

ABSTRACT

Title of Document: SYNTHESIS OF MAGNETIC NANOTUBES
AS MAGNETIC RESONANCE CONTRAST
AGENTS AND DRUG CARRIERS AND THE
STUDY OF THEIR CYTOTOXICITY

Xia Bai, Doctor of Philosophy, 2008

Directed By: Professor Sang Bok Lee
Department of Chemistry and Biochemistry

The increasing interest in the medical application of nanotechnology has heightened the need for synthesizing nanoparticles with well-defined dimensions and multifunctionalities. Studies on template synthesis demonstrate relatively reliable reproducibility of the nanostructures. Moreover, differential modification can be achieved with template synthesis method.

Based on template synthesis method, magnetic nanotubes (MNT), silica nanotubes (SNT) loaded with superparamagnetic iron oxide nanoparticles (SPION), were successfully prepared. The magnetic properties of MNTs including saturation magnetization (M_{sat}) and magnetic resonance (MR) relaxivities were investigated. Results revealed that M_{sat} of MNTs is as high as 95 emu/gFe, which is on the highest side of reported value for magnetite nanoparticles. The MR study showed that MNTs enhanced proton MR relaxation considerably, especially transverse relaxation T_2 (*). The transverse relaxivities (r_2 (*)) of MNTs are higher than that of Feridex, a FDA

approved MR contrast agent, indicating that MNTs could potentially act as efficacious T_2^* -weighted MR contrast agents.

MNTs were also studied as drug carriers to control the loading and release of Doxorubicin (Dox: a cancer drug model). The inner surfaces of MNTs were modified with C18- and pyridine-silane with various ratios. The results showed that Dox molecules held in the MNTs were stable at pH 7.2, and released at pH 4.5. With proper modification, MNTs can be used to control drug release profiles. The magnetic nanoparticles in MNTs helped in loading drug molecules due to barrier effect.

Cytotoxicity and cellular uptake of SNTs with two different sizes and surface charges were investigated for two cell models, primary (non-malignant) and cancer cells. The nanotubes showed limited toxicity which was concentration-, surface charge-, and length- dependent. The internalization was confirmed with both confocal microscopy and TEM studies. Confocal microscopic images demonstrated that endocytosis was one of the main mechanisms for internalization of nanotubes.

A novel method was developed in this thesis to improve multifunctionality of SNT as a drug delivery system by modifying the nanotubes segmentedly between the entrance and the remainder. Ideally, we can make a universal delivery vehicle with SNTs as the constitute structure which can be filled with therapeutic and imaging payloads and have biological surface modifiers for targeting.

SYNTHESIS OF MAGNETIC NANOTUBES AS MAGNETIC RESONANCE
CONTRAST AGENTS AND DRUG CARRIERS AND THE STUDY OF THEIR
CYTOTOXICITY

By

Xia Bai

Dissertation submitted to the Faculty of the Graduate School of the
University of Maryland, College Park, in partial fulfillment
of the requirements for the degree of
Doctor of Philosophy
2008

Advisory Committee:
Professor Sang Bok Lee, Chair
Professor Kyu Yong Choi
Professor Catherine Fenselau
Professor John Fourkas
Professor Cheng Lee

© Copyright by
Xia Bai
2008

My religion consists of a humble admiration of the illimitable superior spirit who reveals himself in the slight details we are able to perceive with our frail and feeble mind.

Albert Einstein

Acknowledgements

I am very grateful to my advisor, Professor Sang Bok Lee. Many thanks to him for the help not only in my research but also in my life. It was pleasant to work with him. He is a person full of enthusiasm and inspiration. Thanks to his considerable patience and encouragement, I survived after these years of research. I also need to pay my respect to my committee members, Professors Kyu Yong Choi, Catherine Fenselau, John Fourkas and Cheng Lee for their great support and precious time. I would also like to thank Dr Joseph Frank from National Institutes of Health for his generosity in sharing instrument and ideas, editing my paper and answering my questions. Thanks to Eric Gold for his assistance with my work in Dr Frank's lab. I also extend my sincere thanks to Dr Wei Liu and Dr Shixiong Zhang for their help with the characterization of magnetic nanoparticles and help me to comprehend the concepts and techniques to carry out my research. Many thanks to Dr Anjan Nan for teaching me the bio-related work, sharing literature and helping me to understand my project. I am also grateful to Dr English for allowing me to work in his lab. He is an excellent teacher. I really enjoyed his group meeting. Thanks to Dr Xiang Wang and Charles Lueckert from Dr English's group for their help with nanotube imaging with confocal microscope. I would like to express my appreciation to Tim Maugel and Jan F. Endlich for their assistance with electron microscopes and endless jokes. Many thanks to Brian Straughn for his help with plasma etching and sharing his books with me. It is always fun to talk with him. I am grateful for the help from Drs Yiu-Fai Lam and Yinde Wang for NMR measurement. I am also thankful for the help from Juhee Park in discussion on my experimental design. Many thanks to my group members

for their valuable support in the lab and for providing a friendly atmosphere. I would also like to thank Dr Chunjuan Zhang, Israel Perez and Parag Banerjee for inspiring discussions. I also wish to express my gratitude to Drs William Ullman, George W. Luther and Stephen Dexter from the University of Delaware for their continuous support and encouragement. Finally, I wish to thank my family. They are the best I have got in my life.

Table of Contents

Acknowledgements.....	iii
Table of Contents.....	v
List of Tables.....	viii
List of Figures.....	ix
List of Schemes.....	xii
Chapter 1: Introduction.....	1
1.1 Nanoparticles as drug carriers.....	1
1.2 Targeted drug delivery systems.....	6
1.2.1 Carbon nanotubes.....	7
1.2.2 Nanocapsule and mesoporous nanospheres.....	8
1.2.3 Nanotubes prepared from template synthesis.....	10
1.3 Nanoparticles for molecular imaging.....	19
1.3.1 Optical imaging probes.....	20
1.3.2 Magnetic resonance contrast agents.....	22
1.4 Cellular uptake of nanoparticles.....	24
1.4.1 Endocytosis.....	24
1.4.2 Size and shape effects on nanoparticle internalization.....	24
Chapter 2: Synthesis of Magnetic Nanotubes.....	27
2.1 Introduction.....	27
2.2 Materials and methods.....	29
2.2.1 Template synthesis of silica nanotubes.....	30
2.2.2 Synthesis of superparamagnetic iron oxide nanoparticles in the silica nanotubes.....	35
2.2.3 Characterization of superparamagnetic iron oxide nanoparticles and magnetic nanotubes.....	35
2.2.4 Iron content measurement.....	36
2.3 Results.....	37
2.3.1 Superparamagnetic iron oxide nanoparticles synthesized in the bulk solutions.....	37
2.3.2 Electron microscopy studies of magnetic nanotubes.....	39
2.3.3 Iron content determination of magnetic nanotubes.....	42
2.3.4 Magnetization of superparamagnetic iron oxide nanoparticles and magnetic nanotubes.....	43
2.4 Discussion.....	48
2.4.1 Polyol method.....	48
2.4.2 Formation of superparamagnetic iron oxide nanoparticles.....	49

2.5 Conclusions.....	50
Chapter 3: Magnetic Nanotubes as Magnetic Resonance Contrast Agents	52
3.1 Introduction.....	52
3.2 Basics of magnetic resonance spectroscopy	52
3.2.1 Physics of magnetic resonance	52
3.2.2 Measurement of relaxation times.....	58
3.3 Magnetic resonance contrast agents.....	62
3.4 Magnetic nanotubes as magnetic resonance contrast agents	65
3.5 Methods.....	66
3.6 Results and discussions.....	67
3.7 Conclusions.....	70
Chapter 4: Loading and Release of Doxorubicin with Magnetic Nanotubes	71
4.1 Introduction.....	71
4.2 Materials and methods	74
4.2.1 Materials	74
4.2.2 Modification of nanotubes	75
4.2.3 Optical images	76
4.2.4 Release profiles.....	76
4.3 Results and discussion	77
4.3.1 Optical images	77
4.3.2 Release profiles.....	79
4.4 Conclusions.....	85
Chapter 5: Cellular Uptake and Cytotoxicity.....	86
5.1 Introduction.....	86
5.2 Experimental.....	88
5.2.1 Surface functionalizations.....	88
5.2.2 Growth inhibition assay of silica nanotubes	89
5.2.3 Confocal microscopy	90
5.2.4 Transmission electron microscopy	91
5.2.5 Cell labeling with MNT-Pro complexes and assessment of toxicity	92
5.3 Results and discussions.....	93
5.4 Conclusions.....	104
Chapter 6: Segmented Modification of Nanotubes.....	105
6.1 Introduction.....	105
6.1.1 Differential modifications.....	105
6.1.2 Segmented functionalizations	108
6.1.3 Dry etching.....	109
6.2 Experimental design.....	111
6.2.1 Materials	111
6.2.2 Modifications of the inner surfaces of silica nanotubes.....	112
6.2.3 Photoresist coating.....	113
6.3.4 O ₂ plasma etching	113

6.3.5 Segmented functionalization of nanotubes	114
6.3 Results and discussions.....	116
6.4 Conclusions.....	120
Chapter 7 Conclusions and Future Work.....	122
7.1 Conclusions.....	122
7.2 Future work.....	123
References:.....	125

List of Tables

Table 2.1 The iron content of MNTs with different inner surface modifications.....	43
Table 3.1 Relaxivities r_1 , r_2 and r_2^* of ferumoxide and magnetic nanotubes (MNTs) for T_1 -, T_2 - and T_2^* - weighted imaging.....	68

List of Figures

Figure 1.1 Principle of drug controlled release.....	2
Figure 1.2 Multifunctional nanoparticles[3].....	3
Figure 1.3 Schematic illustration of the EPR effect principle. (a) normal tissue and (b) tumor tissue. Angiogenesis and enhanced vascular permeability of tumor capillaries and impaired or missing lymphatic clearance of nanoparticles result in accumulation of nanoparticles in tumor tissue (after [12]).	5
Figure 1.4 Scanning electron microscopic images of alumina template	11
(a) top view; (b) side view	11
Figure 1.5 Scheme for differential functionalization of silica nanotubes.....	12
Figure 1.6 Releasing profiles of 5-Fu, 4-NO ₂ -Ph and ibuprofen from MNTs in phosphate buffer solutions (pH 7.4) [44].....	15
Figure 1.7 SEM images of (a) template embedded and (b) liberated corked nanotest tubes. Scale bar: 500 nm [48]	17
Figure 1.8 Scheme for partial modification of silica nanotubes with gold nanoparticles and gold capping [50]	18
Figure 1.8 Cellular uptake of gold nanoparticles with different size [68]	25
Figure 2.2 Preparation of AAO templates with a two-step anodization	32
Figure 2.3 TEM images of silica nanotubes obtained with (a) mechanical polishing and (b) dry etching. Scale bar: 200 nm	34
Figure 2.4 Transmission electron microscopy (TEM) images for the magnetite nanoparticles synthesized with different precursor concentrations: a) 0.05M, b) 0.01M, and c) 0.005M (Scale bar: 50 nm)	38
Figure 2.5 TEM images for superparamagnetic iron oxide nanoparticles (SPIONs) obtained with 2 hrs reflux (a) and 4 hrs reflux (b) in a 0.002 M iron precursor solution (scale bar: 50 nm).....	39
Figure 2.6 Scanning electron microscopy (SEM) images of the top view (a) and side-view (b) of 2 μm-magnetic nanotubes (MNTs, length: 2 μm, diameter: 70 nm) embedded in a AAO template.	40
Figure 2.7 Energy-dispersive X-ray spectrum (EDS) of magnetic nanotubes. Fe, Si, and O peaks represent the composition of magnetic nanotubes. Cu and C peaks come from the specimen grid and the Formvar carbon supporting film.....	40
Figure 2.8 High resolution transmission electron microscopy (TEM) image for MNTs.	41
Figure 2.9 Calibration curve for relaxation rate ($1/T_2, s^{-1}$) as a function of iron concentration (C_{Fe}, mM): $1/T_2 = 8.4287 C_{Fe} + 0.3853$, with correlation coefficient of 0.999	42
Figure 2.10 Magnetic nanoparticles in ethanol with (a) and without (b) external magnetic field.....	44
Figure 2.11 Magnetization (M) - magnetic field (H) relations (T = 300 K) of 2 μm-magnetic nanotubes (MNTs) synthesized by a two-step 2 hrs reflux in 0.002 M iron precursor solutions, and of superparamagnetic iron oxide nanoparticles (SPIONs) synthesized by a 4 hrs reflux in a 0.002 M iron precursor solution.....	45

Figure 2.12 Field cooled (FC) and zero field cooled (ZFC) magnetization as a function of temperature for superparamagnetic iron oxide nanoparticles (SPIONs) obtained with 4 hrs reflux in 0.002 M iron precursor solutions (a), and 2 μm -magnetic nanotubes (MNTs) obtained from two-step reflux with the same iron precursor solutions (b).	47
Figure 3.1 Spin of magnetization vector (M_0) with the applied magnetic field (B_0)	53
Figure 3.2 T_1 relaxation with a RF 90° pulse	55
Figure 3.3 T_1 relaxation with a RF 180° pulse	56
Figure 3.4 T_2 relaxation	57
Figure 3.5 T_2^* decay	62
Figure 3.6 T_1 and T_2 contrast	63
Figure 3.7 Relaxation rates as a function of iron concentration (mM): (a) T_1 relaxation rates ($1/T_1, \text{s}^{-1}$), (b) T_2 relaxation rates ($1/T_2, \text{s}^{-1}$), and (c) T_2^* relaxation rates ($1/T_2^*, \text{s}^{-1}$) (correlation coefficient is higher than 0.99).	69
Figure 3.8 T_2 - and T_2^* - weighted images for phantoms dispersed with (a) 500 nm-magnetic nanotubes (MNTs) with concentration of 0, 2.4, 4.7, 9.5 and 19 μM (Fe concentration of 0, 0.085, 0.170, 0.213 and 0.426 mM), respectively, and with (b) 2 μm -MNTs with concentration of 0, 3.3, 6.5, 13 and 26 μM (Fe concentration of 0, 0.062, 0.124, 0.248, and 0.495 mM), respectively.	70
Figure 4.1 Lysosomotropic delivery (Duncan, Nature Reviews Cancer (2006))	72
Figure 4.2 Effect of pH on the partition of Dox between chloroform and water [131]	73
Figure 4.3 Optical images of SNTs loaded with Dox. (a) SNTs modified with 100% C18-silane, (b) SNTs modified with 75% C18-silane and 25% pyridine-silane, (c) SNTs modified with 50% C18-silane and 50% pyridine-silane.	78
Figure 4.4 Fluorescence spectra for Dox and calibration curve in acetate buffer at pH 4.5	79
Figure 4.5 Fluorescence spectra for Dox and calibration curves in HEPES buffer at pH 7.2	80
Figure 4.6 Effect of pH on the release profile of Dox from nanotubes	81
Figure 4.7 Dox remained in the nanotubes after release in HEPES buffer	83
Figure 4.8 Dox release profiles at pH 4.5	83
Figure 4.9 Releasing rates of Dox from MNTs	84
Figure 4.10 TEM images of magnetic nanotubes (MNTs) loaded with Dox before release (a) and after incubation in acetic buffer solution (pH 4.5) for 55 h.	85
Figure 5.1 Schematic representation of template synthesis of silica nanotubes	89
Figure 5.2 Scanning electron microscope images of porous alumina template for SNT (dia 50 nm, length 200 nm) (a) Top view, (b) Cross section, and Transmission Electron Microscope images of bare silica nanotubes (50 nm dia.) Length: (c) 200 nm, (d) 500 nm, with inset of TEM image for the cross section of the SNTs bundle.	94
Figure 5.3 MTT cytotoxicity assay showing the effect of varying concentrations of nanotubes on growth inhibition of (a) MDA-MB-231	

breast cancer cells and (b) Human Umbilical Vein Endothelial Cells (HUVEC) cultured in vitro.	96
Figure 5.4 Transmission Electron Microscope images showing uptake of 500 nm positively charged SNTs in MDA-MB-231 cells. Blue arrows indicate cross sectional view and red arrows horizontal view of nanotubes.	99
Figure 5.5 Confocal microscope images of uptake of 200 nm positively charged fluorescent SNTs by MDA-MB231 cells at 37°C. (a) without metabolic inhibitors, and in the presence of metabolic inhibitors of endocytosis namely (b) sodium azide and (c) sucrose. Concentration of SNTs is 0.01 µg/ml.	101
Figure 5.7 MTS cytotoxicity assay results for 500 nm-MNT labeled rat glioma cells for 24 hours.	103
Figure 5.8 Representative Prussian blue-stained (a) unlabeled cells and (b) MNT-Pro labeled cells.	104
Figure 6.1 Schematic representation of the CdS nanoparticles-capped mesoporous silica nanoparticles-based drug delivery system [168]....	107
Figure 6.2 Ion striking energy decreases with pressure and the mechanism changes with the pressure [169].....	110
Figure 6.3 Schematic illustration of a plasma etching system.....	114
Figure 6.4 Scanning microscopy images of silica coated AAO, (a) top view and (b) side view	116
Figure 6.5 Transmission electron microscope (TEM) images of silica nanotubes before photoresist loading (a), and after photoresist loading with O ₂ plasma etching time of 1 min (b), 2 min (c), 4 min (d), and 8 min (e). Scale bar: 200 nm.....	117
Figure 6.6 Optical images of differentially modified nanotubes based on method 1 with inner surfaces pre-modified with AMMD-silane (a and b), and nanotubes pre-modified with DETA-silane (c and d): (a, c) dark field images, (b, d) fluorescence images.....	119
Figure 6.7 Fluorescence images of segmentedly modified nanotubes based on method 2 with inner surfaces pre-modified with DETA-silane. (a) with green dye filter, (b) with red dye filter , and (c) overlap of (a) and (b).....	120

List of Schemes

Scheme 2.1 Preparation of magnetic nanotubes (MNTs)	28
Scheme 2.2 Formation of silica layer on template surfaces with surface sol-gel method.....	33
Scheme 2.3 Formation of magnetite in propane diol: (a) complexation, (b) hydrolysis, (c) condensation	49
Scheme 6.1 Segmented modifications	108
Scheme 6.2 Two methods on segmented modification of nanotubes.....	115

Chapter 1: Introduction

This chapter has been reproduced in part with permission from: Son, JS; Bai, X and Lee, SB, Inorganic hollow nanoparticles and nanotubes in nanomedicine. Part 1: Drug/gene delivery applications. Drug Discovery Today 12(15-16): 650-656; Part 2: Imaging, diagnostic, and therapeutic applications. Drug Discovery Today 12(15-16): 657-663

The global drug delivery products and services market is projected to surpass \$67 billion in 2009. The nanotechnology-enabled drug delivery systems will generate over \$1.7 billion (\$US) in 2009 and over \$4.8 billion in 2012 according to a newly released report from NanoMarkets, an industry consulting firm[1].

1.1 Nanoparticles as drug carriers

Why nano? For conventional therapy, the drug concentration in the blood rises when the drug is taken, then reaches a peak and goes down. A controlled drug delivery system is designed to achieve a prolonged therapeutic effect by releasing the drug continuously over an extended period of time[2], as shown in Figure 1.1. For some drugs, the peaks can cause terrible side effects, and in the valleys the drug is not effective[3]. The therapeutic index is used to define this property of a drug. It is expressed as a ratio between the toxic dose and the therapeutic dose[4]. Generally, it is measured by the lethal dose of a drug for 50% of the population (LD_{50}) divided by the minimum effective dose for 50% of the population (ED_{50}), that is, LD_{50}/ED_{50} . It is known that the side effects are mainly due to the non-specificity of the chemotherapy, indicating that side effects can be reduced or eliminated if healthy cells are spared while malignant cells are killed. However,

most current anticancer drugs do not differentiate between cancerous and normal cells. The maximum allowable dose of the drug is thus limited to avoid toxicity. Additionally, rapid elimination and widespread distribution of the drug demand an administration in a large quantity and make the chemotherapy quite costly. Therefore, it is crucial to improve the drug efficacy and reduce the side effects by administering proper doses of chemotherapeutic drugs in a controlled and targeted manner [3].

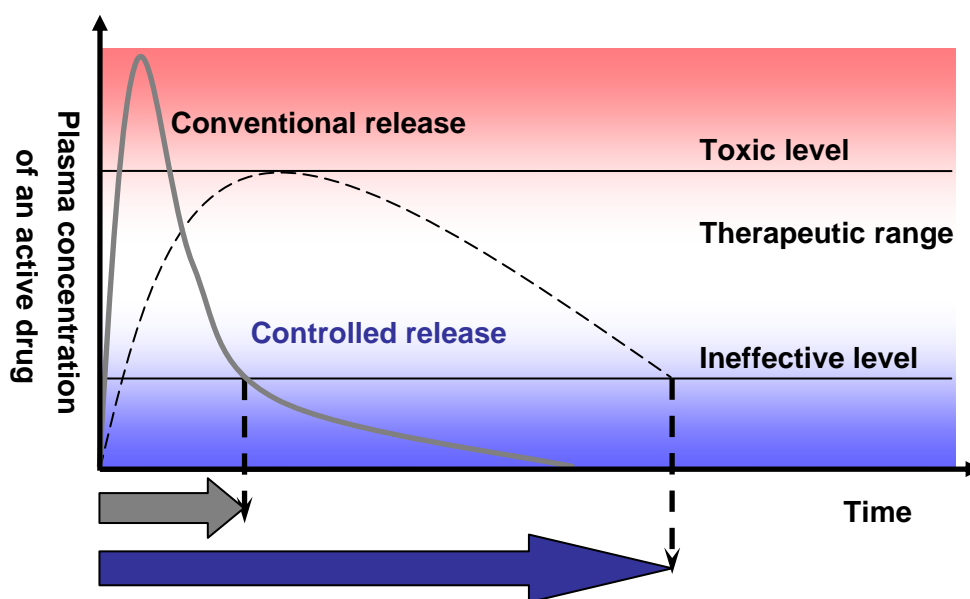


Figure 1.1 Principle of drug controlled release
(www.azom.com/Details.asp?ArticleID=745)

Nanomedicine, a newly emerging discipline, is described as medical applications of nanotechnology to improve healthcare, particularly in cancer[2]. The advantages of nanomedicine over conventional therapy are mainly due to the

physicochemical properties of nanoparticles. Basically, nanoparticles can protect the active agent from premature degradation, accomplish targeted delivery of large and different payloads, and can be multifunctional and versatile (Figure 1.2).

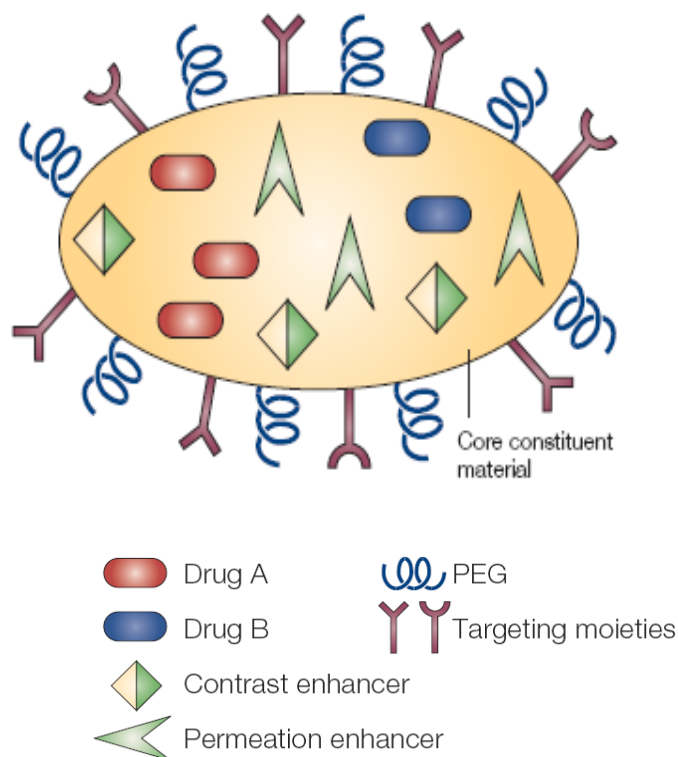


Figure 1.2 Multifunctional nanoparticles[3]

Tumor tissue is different from normal tissue in terms of the structure and behavior of the vasculature and lymphatic systems[5], as illustrated in Figure 1.3. The tumor vasculature, which is leaky, undergoes continuous angiogenesis in order to provide enough nutrients to the growing tumor. Additionally, the lymphatic capillary at the tumor site is very tight or missing, and can not function effectively as a drainage system. This results in the accumulation of nanoparticles in the interstitial space of tumors instead of in the normal tissue. The effect is called the

enhanced permeability and retention (EPR) effect. EPR effect has been considered as a main mechanism for passive targeting of nanoparticles. Targeted drug delivery via the EPR effect is mostly useful for solid, nonmetastatic tumors. Studies on using liposomes with different mean size for passive targeting suggest that the threshold size for extravasation into tumors is ~400 nm, but other studies have shown that particle size less than 200 nm is more effective [6-8]. Moreover, a surface marker, antigen or receptor is generally over-expressed on tumor cells relative to normal cells. For example, growth factor receptors and proteins involved in cell-cell or cell-matrix interactions are usually up-regulated on the surface of tumor associated endothelial cells [9-11]. Nanoparticles with multivalent binding effects will have stronger binding affinity than monovalent binding of free drug molecule. This enhanced affinity can also be used to improve targeting [6].

Goals of nanomedicine include identifying cancer in its earliest stages, visualizing development of the disease, delivering improved therapy to increase the effectiveness and reduce side effects of drugs, and capturing early signals of drug efficacy[13]. Paras Prasad, Ph.D., a professor of chemistry at the University of Buffalo, and Raoul Kopelman, Ph.D., a professor of chemistry, physics, and applied physics at the University of Michigan, have developed nanoparticles that can detect tiny tumors in living animals and at the same time deliver potent, light-activated cell killers specifically to the tumor locations[13]. In fact, nanomedicine can be found in present clinical use, such as Doxil, a liposome-encapsulated dosage

form of doxorubicin made by Ben Venue Laboratories for Johnson & Johnson, used in the treatment of a wide range of cancers, and Ferridex, a dextran coated magnetite nanoparticles as magnetic resonance (MR) contrast agents.

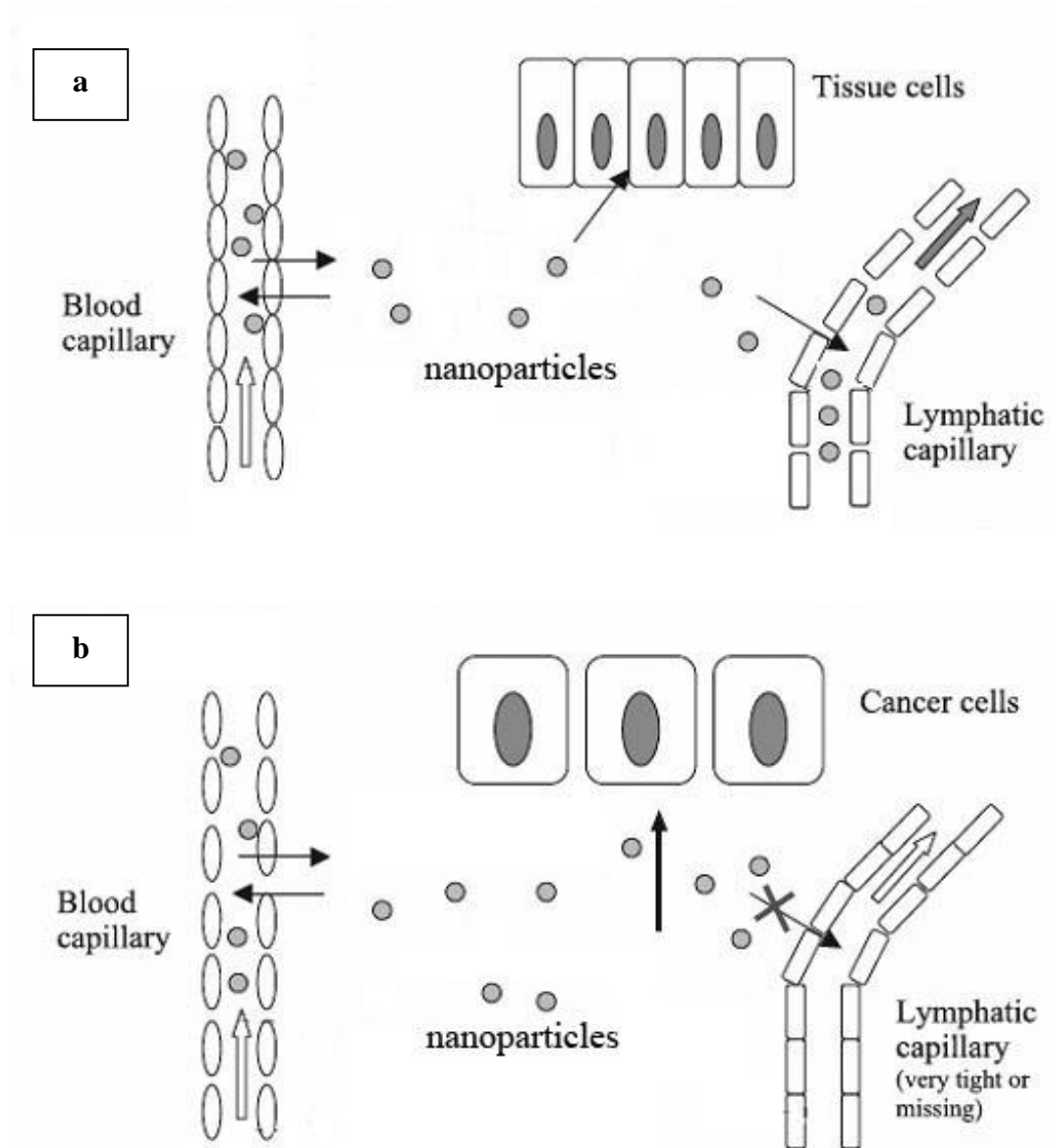


Figure 1.3 Schematic illustration of the EPR effect principle. (a) normal tissue and (b) tumor tissue. Angiogenesis and enhanced vascular permeability of tumor capillaries and impaired or missing lymphatic clearance of nanoparticles result in accumulation of nanoparticles in tumor tissue (after [12]).

In summary, nanomedicine has enormous potential to increase opportunities for prevention, diagnosis and treatment of cancer. Here, I will focus on the application of inorganic hollow nanoparticles for drug delivery and imaging.

1.2 Targeted drug delivery systems

Over a century ago, Paul Ehrlich envisioned the creation of "magic bullets," compounds that would have a specific attraction to disease-causing microorganisms and destroy them, while avoiding other organisms and having no harmful effects on the bodies of patients [14]. The concept of targeted drug delivery was then formed.

Recently, nanotechnology has been rapidly emerging in biomedical and biotechnological applications, including drug/gene delivery carriers, disease diagnosis, and cancer therapy. In most applications, bio-nanomaterials such as liposomes and biodegradable polymers have played key roles in nanomedicine because they are considered to be safe in the human body [15, 16]. In contrast, the use of inorganic nanomaterials such as carbon nanotubes, metals, and metal oxide nanoparticles has been limited by safety issues in biomedical applications.

Since recent cytotoxicity studies on carbon nanotubes (CNTs) have shown that biocompatibility of nanomaterial might be mainly determined by surface functionalization rather than by the size, the shape, and the material itself [17, 18], inorganic nanoparticles are attracting great interest in the field of nanomedicine.

Inorganic nanomaterials have fundamental advantages over bioorganic nanomaterials in terms of their size and shape control and surface

functionalization [3, 19]. In addition, since inorganic nanomaterials permit a wide range of functionality arising from their unique optical, electrical and physical properties, they may provide a solution for many biological barriers that limit biomedical applications.

Nanotubes, nanoshells and mesoporous nanoparticles are attractive vehicles for drug/gene delivery due to their hollow and porous structures and facile surface functionalization. The inner void can take up a large amount of drug and the open ends of pores serve as gates that can control the release of drug/gene. Furthermore, the hollow tubular nanoparticles can be differentially functionalized between the inner and outer surfaces, which can provide a platform of multifunctionalities into the nanoparticle through sequential and sectionalized surface modifications.

1.2.1 Carbon nanotubes

Although carbon nanotubes (CNTs) have attracted increasing attention as new vectors for the delivery of therapeutic molecules due to the ease of translocation across cell membranes and low toxicity [20-23], issues about the ultimate biocompatibility of CNTs have limited their use in biomedical applications [24-26]. However, a recent study reported by Singh *et al.* revealed that water-soluble functionalized CNTs can be rapidly cleared from the systemic blood circulation through the renal excretion route [17]. Less than 1% of injected nanotubes were detected in all organs measured three hours after intravenous administration of nanotubes injected through the tail vein of a mouse. Functionalized CNTs have been used for antigens and gene delivery [20, 27]. In the antigenicity and

immunogenicity studies, peptide-CNT conjugates were recognized by antibodies as well as were free peptide. No immune response to CNTs was detected and gene expression efficiency offered by DNA-CNT was about 10 times higher than that of DNA alone [10].

For the mechanism of cell membrane penetration, a spontaneous process, Bianca *et al.* proposed that CNTs behave like nanoneedles and pass through the cell membrane without causing cell death [28]. The reduced toxicity was thus due to the rapid internalization of CNTs into the cytoplasm of cells and hence reducing the possibility of disruption of the cell membrane structure.

1.2.2 Nanocapsule and mesoporous nanospheres

Mesoporous silica nanosphere

Mesoporous silica nanoparticles are silica nanoparticles with an ordered pore structure. MCM-41, among this family, is the one that has been most extensively studied. MCM-41 type mesoporous silica nanospheres (MSN) have hexagonal arrays of cylindrical mesopores. Generally, the MSNs are synthesized by self-assembly of a silica/surfactant mixture in which inorganic species simultaneously condense forming mesoscopically ordered composites [29, 30]. The average size of MSNs is 200.0 nm with a pore size of 2.3 nm. Based on this structure, drug carrier systems have been developed for gene transfection with high efficiency and low toxicity [31]. Flow cytometry analysis on cells 48 h post-transfection showed an efficiency of 35% with the gene delivery system. This efficiency is higher compared to other commercial transfection reagents, such as PolyFect

(15% efficiency), SuperFect (10%) and Metafectene (16%). Capped with chemically removable cadmium sulfide (CdS) nanoparticles, the nanosystem can be used for stimuli-responsive controlled release of drug molecules [32]. Giri *et al.* developed a superparamagnetic nanoparticle capped MSN system using disulfide bonds for stimuli-triggered release[33]. They proposed that the MSN system could be a promising nanodevice for site-selective, interactive sensory and controlled-release drug delivery.

Hollow carbonaceous capsules

Sun and Li have recently prepared hollow carbonaceous capsules with reactive surface layers *via* hydrothermal methods with the anionic surfactant sodium dodecyl sulfate (SDS) and glucose as starting materials. The void size within the capsule and the shell thickness can be tuned by adjusting the amount of SDS and the hydrothermal parameters, such as time, temperature and glucose concentrations [34].

Calcium phosphate nanoshells

Calcium phosphate, the main component of the skeletons and teeth of vertebrate animals, is biocompatible and biodegradable. Solid calcium phosphate particles have been widely investigated for their applications in biotechnology. Roy *et al.* [35, 36] have synthesized calcium phosphate nanospheres with diameter around 80 nm to encapsulate DNA for targeted gene delivery. The results from studies carried out both *in vitro* and *in vivo* show promising transfection efficiency. The nanoshell form of calcium phosphate has been reported by Schmidt and Ostafin [37]. Nanoshells, unlike nanospheres where the drug is dispersed throughout the

particles, are vesicular systems where the drug can be stored and protected from premature inactivation.

1.2.3 Nanotubes prepared from template synthesis

Although nanoparticles have been successfully used in most nanomaterial-involved biomedical and biotechnological applications, spherical nanoparticles still need to be improved in terms of surface modification and environmental compatibility, especially when multifunctionality is required. Since a sphere has only one surface, every surface functionalization takes place on the same surface, which may lead to interference among various functional groups. In this regard, nanotubes (NTs) can offer attractive alternatives for some applications that require multifunctionalities.

NTs have inner and outer surfaces, which can be functionalized differently depending on their roles (*e.g.* the inside with drugs or imaging agents, and the outside with targeting moieties and antifouling agents). The inner void of the NT, for example, can provide space to load a large amount of drugs and its open end can serve as a gate for drug uptake/release. Due to these unique attributes of NTs, compared with spherical nanoparticles, NTs are considered ideal nanovectors for nanomedicine [19].

Of the various synthetic methods for nanotube production, template synthesis [38] provides the easiest way to control nanotube size and shape. This method offers a general approach for preparing nanomaterials that involves the synthesis or deposition of a desired material within the cylindrical and monodisperse pores of a

nanopore membrane or other solid surface [39]. Figure 1.4 shows an alumina template that has cylindrical nanopores with monodisperse diameters and lengths. Porous alumina templates can be obtained by a well-established electrochemical anodization method on aluminum plates. The dimensions of the pores can typically be adjusted from five to a few hundred nanometers in diameter and from tens of nanometers to hundreds of micrometers in length [40, 41].

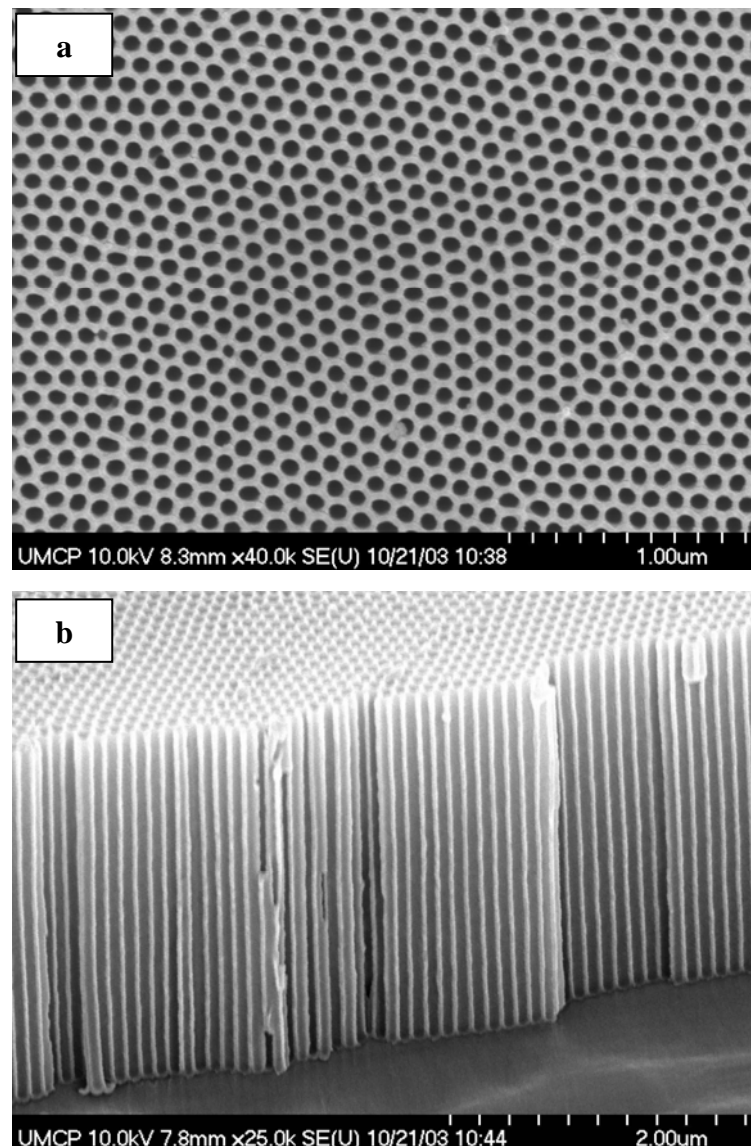
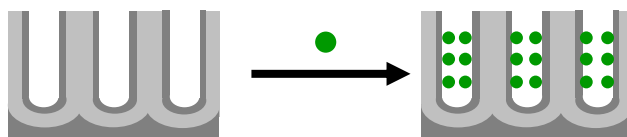


Figure 1.4 Scanning electron microscopic images of alumina template
(a) top view; (b) side view

Another virtue of template synthesis is that differential functionalization between the inner and outer surfaces of nanotubes is possible [42], as shown in Figure 1.5. The modification of the inner surfaces of NTs is performed when they are still embedded in the pores of the template. In this step, the outer surfaces of the NTs remain unmodified because the template protects them. After obtaining free-standing nanotubes by removal of the template, the outer surfaces of the NTs can be exposed for functionalization. Differential functionalization can thus be achieved.

Inner surface modification (when NT embedded in template)



Outer surface modification (after selective dissolution of template)

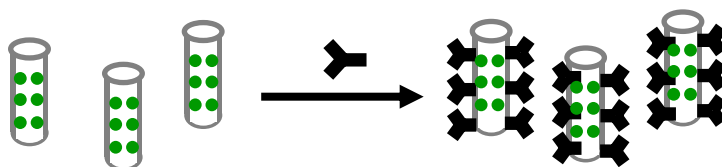


Figure 1.5 Scheme for differential functionalization of silica nanotubes

Silica nanotubes

Chen *et al.* [43] reported fluorescent silica nanotubes (SNTs) for gene delivery.

SNTs were prepared inside pores of 200-nm diameter commercial alumina

membrane *via* a sol-gel process with tetraethyl orthosilicate (TEOS) as the precursor. The inside of the SNT was then modified with 3-aminopropyl silane (APTS) to generate a polycationic surface to hold CdSe/ZnS core-shell quantum dots (QDs) or DNA molecules through the electrostatic forces. Green fluorescent silica nanotubes (gfSNTs) were used for a cell membrane permeability study. Confocal microscopy revealed that the gfSNTs entered about 60-70% of the cells by endocytosis and were mostly localized in the cytoplasm. In cytotoxicity tests, approximately 80% of the cells were still alive after the treatment with gfSNT, indicating that silica nanotubes are not especially toxic under these experimental conditions.

For the gene delivery experiment, the plasmid DNA was inserted into the nanotube to form a DNA/SNT complex. The cytoplasmic green fluorescent protein (GFP) expression complex was observed with DNA/SNT, but not with free DNA. Although the efficiency of SNT-mediated DNA transfection (ca. 10-20%) is less than that of conventional calcium phosphate (ca. 60-70%), the advantage of this strategy is that cargo biomolecules carried by SNTs can be any biomolecules, such as RNA or proteins.

Magnetic nanotubes

Son *et al.* have reported magnetic nanotubes (MNTs), silica nanotubes embedded with magnetite nanoparticles [44]. The main advantage of the drug carrier having a magnetic property is that it allows for the use of a powerful imaging technique, magnetic resonance imaging (MRI), to track drug delivery. In addition, movement

of the drug carrier can be controlled by an external magnetic field, and hence directed to specific anatomical sites *in vivo*. The combination of attractive magnetic properties with a tubular structure makes the MNT an ideal candidate as a multifunctional nanomaterial for biomedical applications. For the synthesis of MNTs, silica nanotubes were first prepared by the surface sol-gel (SSG) method [45]. The resulting template embedded with silica nanotubes was dip-coated with a 4:1 mixture solution of 1 M FeCl₃ and 2 M FeCl₂, dried, and treated with 1 M NH₄OH [46].

The inner void of MNTs can be used to control the release of drug molecules into a solution. To achieve this result, the insides of the MNTs were differentially functionalized with aminopropyltriethoxysilane, APTS. 5-fluorouracil (5-FU), 4-nitrophenol, and ibuprofen (Ibu) were tested as model drugs for the controlled release experiments[44]. As shown in Figure 1.6, depending on pKa values (Ibu, 4.8; 4-nitrophenol, 7.2; 5-FU, 8.1), different release patterns were observed. For example, 10% of the ibuprofen was released in 1 hr and 80% was released after 24 hrs, whereas more than 90% of the 5-FU and the 4-nitrophenol were released in 1h. Son *et al.* proposed that the strength of ionic interactions between drug molecules and amine groups of the nanotube inner surface is a main factor for the drug release from the inside of the NT. This suggests that the drug release rate can be controlled by regulating the modification of the inner surfaces of NTs based on molecular interactions, such as ionic or hydrophobic interactions.

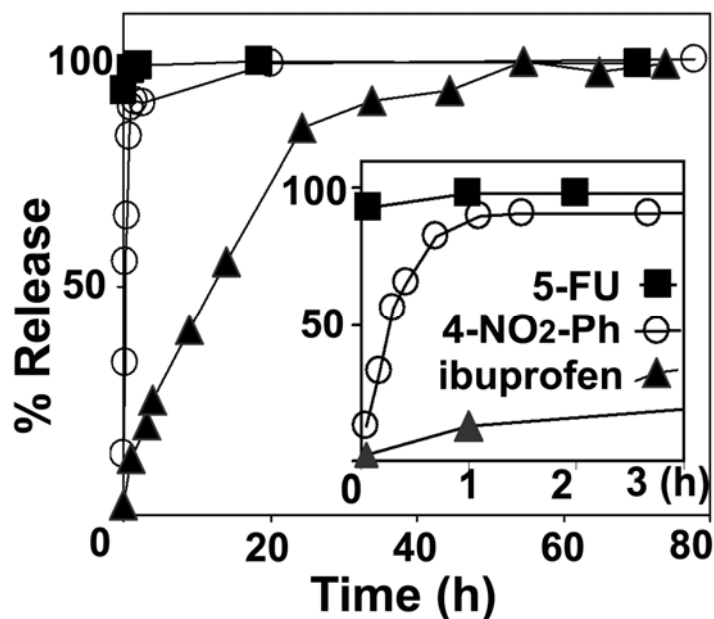


Figure 1.6 Releasing profiles of 5-Fu, 4-NO₂-Ph and ibuprofen from MNTs in phosphate buffer solutions (pH 7.4) [44]

Another type of MNTs, heterostructured MNTs, was produced through layer-by-layer (LbL) deposition of polyelectrolytes and nanoparticles in the pores of a track-etched polycarbonate membrane[47]. These MNTs are composed of alternating multilayers of cationic poly(allylamine hydrochloride) and anionic poly(styrene sulfonate), and then a multilayer of magnetite nanoparticles (NPs). The content of magnetite NPs was calculated to be 20% of the total mass of the MNTs on the basis of the saturation magnetization. Large uptake of anionic molecules was observed when MNTs were treated with acid (pH < 2.5). Lee *et al.* proposed that the increased capacity arises from the protonation of free amine groups within the multilayers and a pH-sensitive swelling of the polyelectrolytes. For use as drug carriers, three anionic molecules (ibuprofen, acid red 8 and rose Bengal) were tested in a release study using acid-treated MNTs. Results revealed

that molecular structure, particularly the size of the anionic molecules, played a key role in sustained drug release. In the case of bulky rose bengal, sustained release was observed, whereas small ibuprofen was immediately released.

Nanotubes corked with nanoparticles

Surface functionalization has been used for NTs to control drug release [19, 48]. However, this approach does not offer a full range of drug release control. An alternative payload-release strategy was explored by Martin and coworkers by corking nanotubes with a chemically labile cap [48]. Open ends of NTs functionalized with amino groups were spontaneously corked with anionic aldehyde-functionalized latex NPs via Schiff base linkage when the NTs were embedded in the alumina template. More than 80% of liberated NTs from the template remain corked, indicating that NP caps are not attached to the ends of NTs by electrostatic interactions but rather by covalent imine linkages (Figure 1.7). Schiff's bases are known to be thermodynamically unstable in the presence of water, but they proposed that the metastable condition of the assembled structure is possible due to the multiple points of contact between the NTs and NPs. They suggested that if NTs could be loaded with a payload, such as drugs or genes, before corking the open ends with a chemically labile cap, these NTs could be used as a universal delivery vehicle.

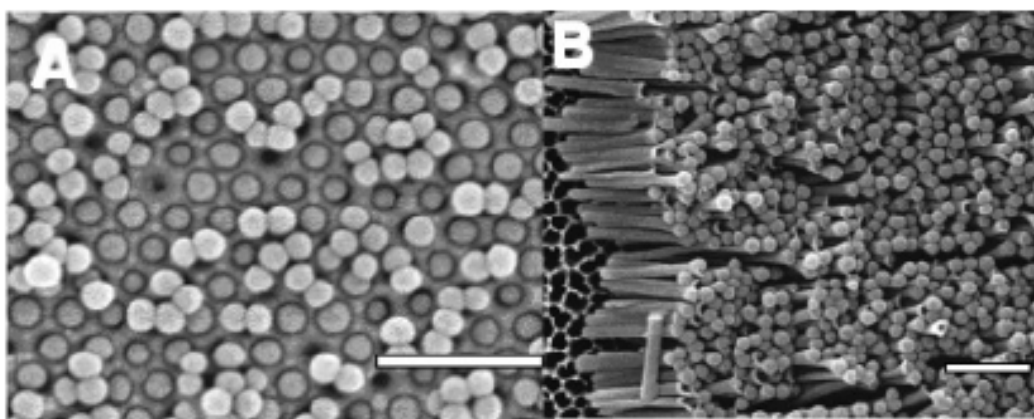


Figure 1.7 SEM images of (a) template embedded and (b) liberated corked nanotubes. Scale bar: 500 nm [48]

Another approach to cap NTs was achieved by our group with gold nanoparticles (NPs)[49], as shown schematically in Figure 1.8. In this method, negatively charged 2-nm Au NPs were selectively immobilized on the positively charged inside of a nanotube through attractive electrostatic interactions. Since the non-functionalized outer surface bears partial negative charges and the repulsive forces produced by Au NPs occupying the open ends blocks further diffusion of Au NPs into the channel of the NTs, the Au NPs were localized at the open end of nanotubes and were found neither on the outer surfaces of NTs nor on the deep inner surface. Pre-trapped Au NPs can serve as a seed for a “seed-mediated gold growth” reaction to make caps at the open end of the NTs [50]. In this reaction, HAuCl_4 was exclusively deposited onto the pre-trapped Au NPs after reduction with ascorbic acid. The capping procedure can be potentially adopted for a general in-situ encapsulation of biomolecules (*e.g.* DNA or enzyme).

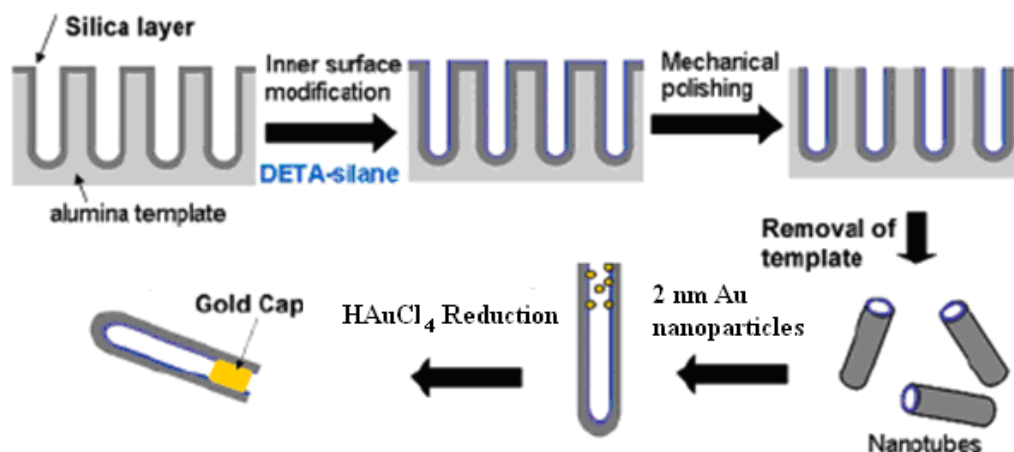


Figure 1.8 Scheme for partial modification of silica nanotubes with gold nanoparticles and gold capping [50]

In summary, the unique properties of a variety of inorganic materials such as mesoporous silica and CNTs make it possible to enhance, or even surpass, the capabilities of conventional delivery. The fundamental advantage of the use of hollow and porous inorganic nanomaterials in biomedicine lies in multifunctionality and well-controlled physicochemical properties. Together with the generic transporting ability of porous materials, useful properties in biomedical applications such as magnetism and NIR absorbance, can be easily integrated in a single unit. However, more research is needed before the hollow and porous inorganic nanomaterials are able to be used outside of laboratory. Although long-term safety studies have to be thoroughly examined, recent studies show that the characteristics being used for assessing inorganic material safety for *in vivo* applications vary with the type, size, and shape of a material [17, 18, 20].

Inorganic nanomaterials can be appropriate for biomedical use with proper surface treatments.

1.3 Nanoparticles for molecular imaging

Molecular imaging is an emerging field that aims to integrate patient-specific and disease-specific molecular information with traditional imaging techniques[51]. It differs from traditional imaging in that probes are used to image particular targets on the cellular level. The ability of nanoparticles to interact with complex biological functions can provide information about the fundamental mechanisms and signaling pathways involved in the progression of disease [52].

Organic fluorophore-based detection techniques have been widely used as imaging and signal transduction tools for the detection of trace levels of analytes. The photostability of the fluorophores, however, limits their application in complex environments, such as living bio-systems where degradation or photobleaching can occur. The potential of nanoparticles with various sizes, shapes and materials as the carriers of fluorophores or imaging agents has been studied as a possible solution to this problem.

Quantum dots (QDs) are one of the most intriguing fluorescent probes, due to their unique optical properties. QDs have high quantum yields, high molar extinction coefficients (~10 – 100 times than that of organic dyes) and broad absorption with narrow, symmetric photoluminescence spectra from UV to near infrared [53, 54]; however, the bioconjugation of QDs is somewhat challenging and is relatively inflexible [53].

Hollow and mesoporous nanoparticles, such as nanotubes, nanoshells and hollow spheres can be loaded with a large amount of imaging molecules, which will considerably enhance signal and sensitivity. The detection of trace amounts of biomolecules, critical for early imaging and diagnosis of cancer, will be facilitated by nanoparticles that are concentrated with imaging molecules. Additionally, the photostability of doped imaging molecules is increased by the protective carriers. Compared with polymer nanoparticles, the advantages of silica nanoparticles lie in well-developed silane chemistry, easy preparation and biocompatibility [55, 56]. In addition to functioning as imaging agents, hollow and mesoporous nanoparticles with distinct inner and outer surfaces have potential as drug carriers. To be able to detect, treat and report the success of therapy with a single injection will eventually be a future and challenging medical application of nanotechnology. Here, I will review recent developments of using hollow and porous inorganic nanomaterials for sensing and imaging.

1.3.1 Optical imaging probes

A fundamental limitation of molecular imaging is the signal to background ratio caused by non-specific adhesion of bio-imaging agents to surfaces [57], making it difficult to identify a low intensity signal. A molecular imaging agent that emits light following a particular molecular event is ideal for *in vivo* tissue pathology. With well-developed silane chemistry, various surface modifications of silica nanoparticles can easily be realized and are widely performed. Silica nanoparticle-

based bio-imaging agents are promising in nanomedicine as bioimaging agents [58].

The two general synthetic approaches to prepare dye-doped silica nanoparticles are the Stober method and a microemulsion process. Ow *et al.* [55] have synthesized multifunctional silica-based fluorescent nanoparticles using the Stober method. The encapsulation process first involves covalent attachment of the dye molecules to an amine-containing silica precursor to form a dye-rich core, followed by co-condensation of silica precursor with sol-gel monomer to form a denser silica network around the core. This approach enables the incorporation of a variety of dye molecules into the silica nanoparticles. These nanoparticles are monodisperse with a diameter of 30 nm. The fluorescent silica nanoparticles are 20 times brighter than the constituent dye. Ow *et al.* [55] proposed that the protection of the fluorophore from the solvent by the silica shell increases the photostability and, hence, contributes to the enhancement of brightness.

For the microemulsion process, dye-doped silica nanoparticles are synthesized by hydrolyzing tetraethyl orthosilicate (TEOS) in a reverse micelle or water-in-oil microemulsion system. The dye molecules are encapsulated physically in the silica matrix. Zhao *et al.* [59] synthesized these nanoparticles for bioanalysis applications as labeling reagents. The dye molecule was linked to a dextran molecule before the reverse microemulsion process. In this way, the organic dye molecules become more water soluble, more easily entrapped inside silica pores and have reduced leakage due to the increased size. Effective entrapment of a

large amount of dye molecules in each silica nanoparticle makes feasible ultra-sensitive detection in bioanalysis.

Nanoshells have a high scattering optical cross-section and thus can also work as contrast agents for photonics-based imaging modalities, such as reflectance confocal microscopy and optical coherence tomography. The scattering of light in the near infrared (NIR) spectral range can provide optical signals for cancer detection whereas biological tissue has low inherent scattering. Loo *et al.* [60] have designed immunotargeted nanoshells to simultaneously provide both scattering and absorption at specific frequencies in the NIR spectral region for dual imaging/therapy applications. They successfully detected and destroyed breast carcinoma cells that overexpress HER2 using the antibody-conjugated nanoshells.

1.3.2 Magnetic resonance contrast agents

Ultra-short single-walled carbon nanotubes (US-tubes) loaded with Gd^{3+} -ion clusters have been shown to have a T_1 relaxivity 40 to 90 times larger than any Gd^{3+} -based contrast agent (CA) in current clinical use. The observed enhancement of the relaxation rate was considered to be mainly related to the proton/water exchange rate, the rotational correlation time, and the relaxation rate of the Gd^{3+} electron spin[35].

Taylor *et al.* have developed Gd^{3+} -containing mesoporous silica nanospheres as MRI CAs [61]. T_1 -weighted MR images with the hybrid materials show signal

enhancement. The dose (2.1 $\mu\text{mol/kg}$) is much lower than what is typically required of currently used contrast agents (0.1-0.3 mmol/kg).

Titirici *et al.* have reported a simple one-pot synthesis of hollow spheres of crystalline metal oxide *via* a hydrothermal approach [62]. Various metal salts were dissolved together with carbohydrates in water and then heated at 180°C in an autoclave. Hollow spheres of various metal oxides, such as Fe_2O_3 , Ni_2O_3 , Co_3O_4 , CeO_2 , MgO , and CuO , can be obtained. Template-free syntheses of water soluble and amine-functionalized magnetic hollow nanospheres have been developed by Wang *et al.* [63]. The hollow nanospheres were prepared by dissolving 1,6-hexadamine and sodium acetate in $\text{FeCl}_3 \cdot 6\text{H}_2\text{O}$ in ethylene glycol. By controlling the amount of the ligand, 1,6-hexadamine, nanospheres of 100 to 200 nm were obtained. *In vivo* magnetic resonance imaging experiments revealed magnetite solid nanoparticles were obtained with a higher concentration of 1,6-hexadamine and a smaller amount of anhydrous sodium acetate. The saturation magnetizations of the hollow spheres with a diameter of 150 nm and the nanoparticles with tunable size from ~15 to ~50 nm were determined to be 71.2 and 41.3-59.8 emu/g at 25°C. *In vivo* magnetic resonance imaging in live mice was performed with 25 nm amine-functionalized magnetic nanoparticles as a contrast agent while no acute fatal toxicity was observed.

1.4 Cellular uptake of nanoparticles

1.4.1 Endocytosis

Large polar molecules or nanoparticles cannot pass through the hydrophobic plasma membrane of cells. Cells use endocytosis to take up nanoparticles [64-66] by envelope of particles with plasma membrane. There are three major types of endocytosis: phagocytosis, pinocytosis, and receptor-mediated endocytosis. Pinocytosis (cell-drinking) is a process related with the uptake of solutes and single molecules such as proteins. Phagocytosis (cell-eating) is a process for cells to ingest large objects, such as bacteria or viruses or dead cells. For receptor-mediated endocytosis- a more specific active event, cells have pits coated with the protein (e.g., clathrin) that initiate endocytosis when the target particles bind to the receptor proteins in the plasma membrane. The cytoplasmic membrane folds inward to form coated pits and buds to form cytoplasmic vesicles[67].

1.4.2 Size and shape effects on nanoparticle internalization

Research has been carried out to study the size and shape effects of nanoparticles on cellular uptake. To be an effective drug carrier, the size of nanoparticles need to be controlled. It must be small enough to avoid rapid filtration by the spleen, which has a filament spacing of about 200 nm, it must be small enough to avoid Kupffer cell-lined sieve plates with 150-200 nm-sized fenestrae [52]. Chithrani *et al.* have studied the size dependence of gold nanoparticle uptake[68]. The results reveal that the cellular uptake is heavily dependent upon the size, and the

maximum uptake occurs for nanoparticles with size of 50 nm, as shown in Figure 1.8. A mechanism has been proposed by the researchers from the same group to explain the uptake process[69]. This “wrapping time” mechanism involves factors like the ratio of adhesion and membrane stretching, the membrane’s bending energy and particle size. NPs with a size about 50 nm would have the fastest wrapping time, as also suggested by Gao *et al.*[66].

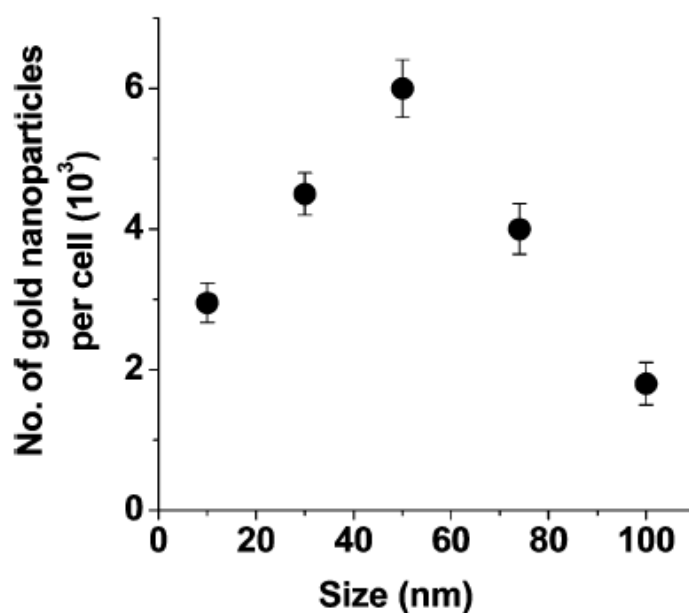


Figure 1.8 Cellular uptake of gold nanoparticles with different size [68]

Carbon nanotubes (CNTs) have been demonstrated as an effective carrier for gene and anti-cancer drug delivery[27, 70]. However, the mechanism of the cellular uptake of CNTs is not clear. One of the key advantages of CNTs over other nanoparticle carriers has been considered to be the possibility of crossing biological barriers effectively [71]. Dennis Dishcer and colleagues have reported that filamentous polymeric micelles known as filomicelles (22 to 60 nm in

diameter, and 2 to 8 μm in length) have a blood circulation time that is ten times greater than their spherical counterparts and have a high efficiency in deliver the anticancer drugs [72]. However, the study on cellular uptake of gold nanoparticles (NPs) of different shapes showed a lower uptake of rod-shaped gold NPs in comparison to spherical shaped NPs and the rates of uptake were lower with an increasing aspect ratio[69].

Chapter 2: Synthesis of Magnetic Nanotubes

This chapter has been reproduced in part with permission from Bai, X; Son, SJ; Zhang, SX; Liu, W; Jordan, EK; Frank, JA; Venkatesan, T; Lee, SB, Synthesis of superparamagnetic nanotubes as magnetic resonance imaging contrast agents and for cell labeling. *Nanomedicine* 3(2): 163-174.

2.1 Introduction

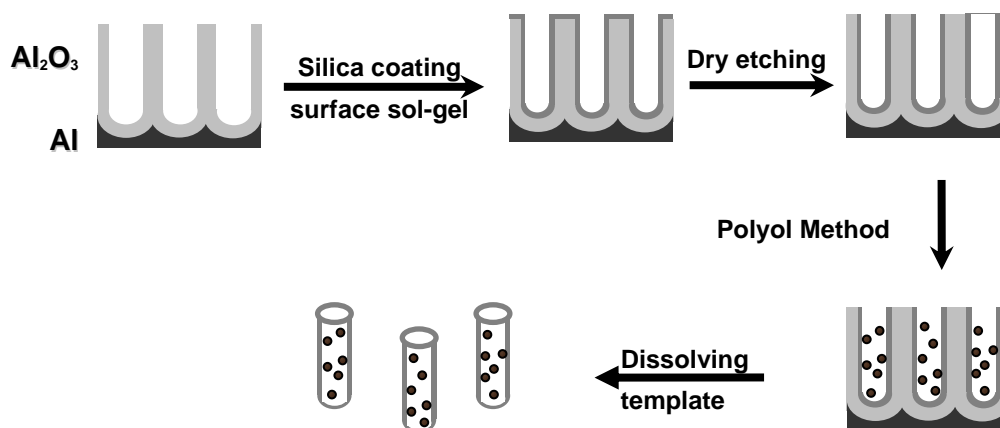
The protocols for synthesis of superparamagnetic iron oxide nanoparticles (SPIONs) can be classified as water-phase and non-hydrolytic high-temperature growth methods[73-75]. The water-phase based methods generally produce SPIONs with poor crystallinity and a polydisperse size distribution. On the contrary, the high-temperature growth methods have better control of the size distribution and magnetic properties, but encounter difficulties in water solubility and surface modification. Magnetic nanoparticles without effective surface coating have very limited practical applications because their suspensions are quite unstable. They tend to aggregate and precipitate out of solution and their magnetic properties vary. Various types of biocompatible SPIONs have been developed, such as liposomes, dendrimers, polymer-coated, and silica-coated iron oxide, *etc.*[73, 76].

Silica nanotubes (SNTs), with well-defined, robust and monodisperse structures, have attracted intensive attention recently for biotechnological studies[39, 77-82]. SNTs have several important merits in terms of multifunctionality due to their structural features [39, 48, 83]: namely, (i) an inner void for accommodating molecules such as drugs and protecting them from environment such as enzyme

reactions and nonspecific adsorptions; (ii) an open end for controlling drug uptake and release; (iii) distinctive inner and outer surfaces that can be differentially functionalized for imaging and targeting moieties. Lee and coworkers have recently used these concepts to prepare MNTs, a silica nanotube (SNT)/SPION composite. Although they demonstrated proof-of-concept experiments on chemical separations, immunobinding, and controlled drug release [44, 84], the saturation magnetization (M_{sat}) was low (2 emu/g), which limited these applications of these materials.

In this chapter, a method is designed to synthesize MNTs in order to obtain high value of saturation magnetization, M_{sat} . The method is based on a polyol method. The polyol method was originally reported for the synthesis of monodisperse metal and polymetal fine particles in the late 1980s with inorganic salts, such as nitrates, alcoholates, as precursors. Polyol was used as both a reducing agent and a solvent. Oxide nanoparticles prepared by the polyol method have been recently reported with high yield, narrow size distribution and good crystallinity [85-88]. Scheme 2.1 illustrates the route for the preparation of MNTs.

Scheme 2.1 Preparation of magnetic nanotubes (MNTs)



2.2 Materials and methods

Silicon tetrachloride (SiCl₄, 99.8%, Acros Organics), oxalic acid (dehydrate, Acros), o-phosphoric acid (85%, Fisher), chromic acid (10%, W/C, LabChem, Inc.), hexane (Fisher), ethanol (Pharmco-AAPER), methanol (Fisher), and perchloric acid (70%, Fisher) were used as supplied without further purification. Aluminum foils (99.99%) and ferric chloride hexahydrate (FeCl₃·6H₂O 97.0-102.0%) was obtained from Alfa Aesar (Ward Hill, MA), while propylene glycol (J.T. Baker, Philipsburg, NJ) and sodium acetate (ACS reagent) were obtained from Fisher Scientific. Deionized (DI) water was obtained by a Milli-Q A10 system and used for all the experiments. All the silane agents were obtained from Gelest, including EDTA-silane (n-(trimethoxysilylpropyl)ethylenediamine, triacetic acid, sodium salt, 45% in water), DETA ((3-Trimethoxysilylpropyl)diethylenetriamine, 95%) and PEG-silane (2-[methoxy(polyethyleneoxy)propyl]trimethoxysilane, 90%).

2.2.1 Template synthesis of silica nanotubes

The home-made alumina templates were prepared with a two-step anodization of aluminum plates (99.99%, Alfa Aesar). The cell setup is illustrated in Figure 2.1. An aluminum plate functions as the anode and two pieces of stainless steel act as the cathode in an electrolyte. The cell temperature is controlled by a water pump thermostat (Isotemp 3016).

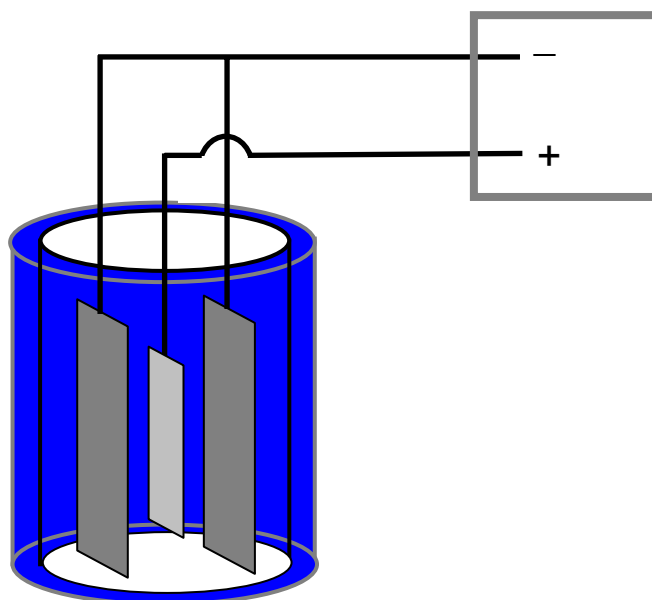


Figure 2.1. Electrochemical cell setup with an aluminum plate as the anode, stainless steel plates as the cathode in an electrolyte.

The aluminum plates were first degreased by sonicating for 10 min in acetone. The plate was then electropolished with perchloric acid solution (perchloric acid: ethanol v/v = 1:5) at 15 V, 5 °C for 5 min. The electropolishing step produces stress-free and relatively uniform metal surfaces compared to the surfaces obtained with mechanical finishing[89]. The two-step anodization was carried out

at 40 V and 10 °C in 0.3 M oxalic acid solutions. The process is demonstrated in Figure 2.2. When aluminum is oxidized to alumina, the volume expands. This leads to compressive stresses in the oxide layer since the oxidation takes place at the entire metal/oxide interface. This stress can promote the formation of well-defined self-ordered pore structure of aluminum anodic oxide (AAO) films[90, 91]. The AAO layer tends to become more and more ordered with anodization time. The oxide film obtained from the first step anodization was etched off by a mixture composed of chromic acid (1.5 wt%) and phosphoric acid (6 wt%). Since the anodic film formation involves generally the conversion of a pre-existing film on the surface[89] , second anodization results in a layer of AAO with a more ordered pattern. The thickness of the final oxide film was controlled by the second anodization time. The final pore diameter was controlled by a pore-widening step in 0.1 M phosphoric acid solution at 38 °C.

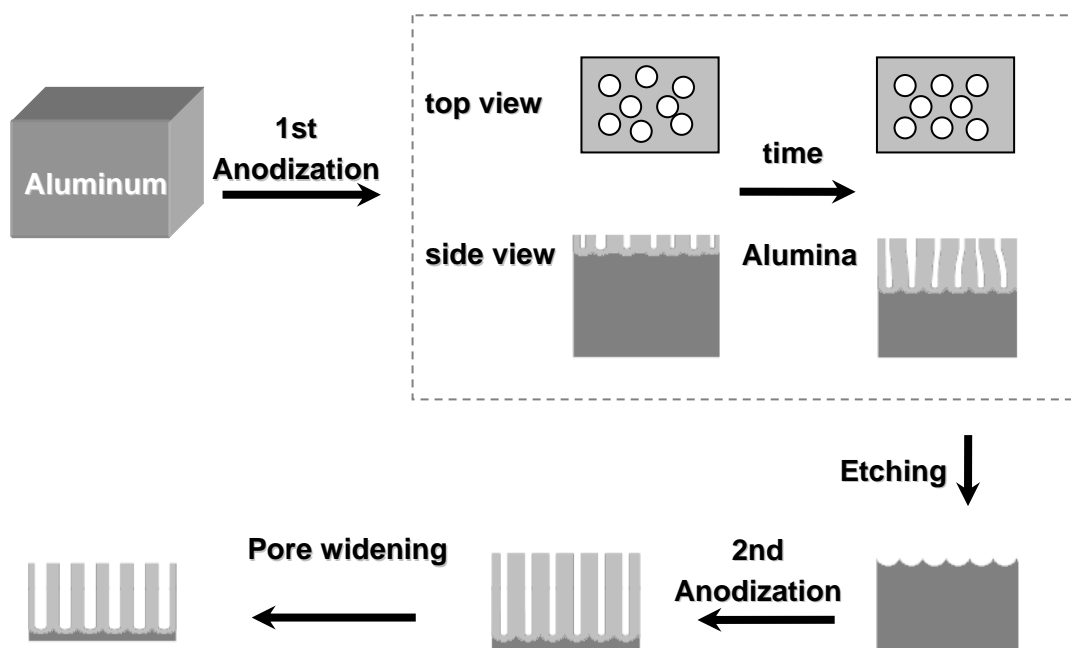
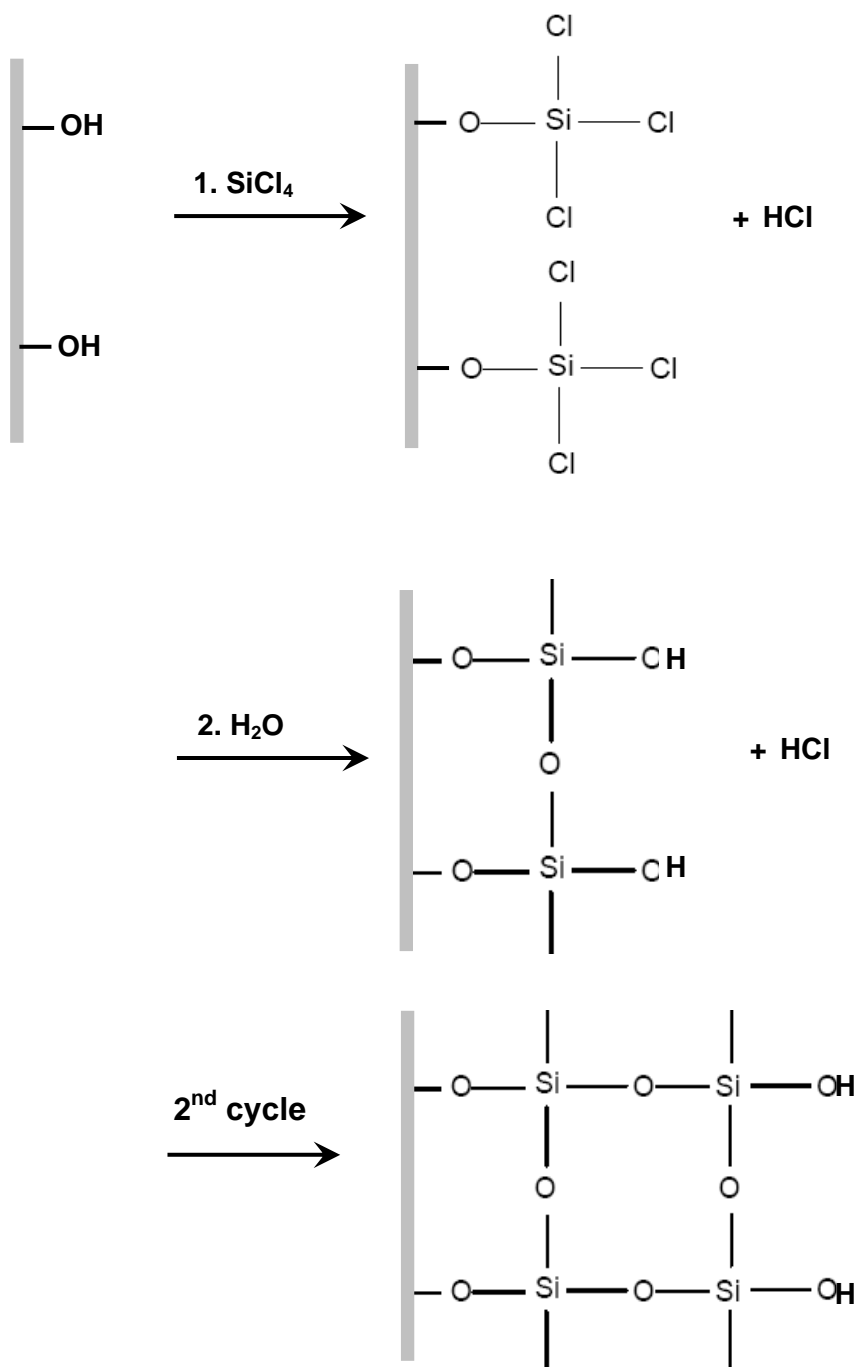


Figure 2.2 Preparation of AAO templates with a two-step anodization

SNTs were synthesized by depositing a silica layer in the pores of the templates via a surface sol-gel method[92], as shown in Scheme 2.2. The basic reaction is hydrolysis of SiCl_4 to form silica (silicon dioxide). Briefly, the template was dipped in SiCl_4 , and then rinsed with hexane, a mixture of hexane and methanol, and ethanol in sequence. The rinsing process with organic solvents from low to high polarity is to remove unbound SiCl_4 molecules to have a layer of SiCl_4 left on the template surfaces. The template was then dried with nitrogen gas, and immersed in water to finish the reaction. The wall thickness of the nanotubes increases on the nanometer scale with the number of sol-gel cycles.

Scheme 2.2 Formation of silica layer on template surfaces with surface sol-gel method



The silica layer on the top surface of the template was removed via either mechanical polishing using alumina powder with a particle size of $0.3\ \mu\text{m}$ (MSI, AP-254), or by dry etching with CHF_3 , to expose the alumina template. For dry

etching, the silica coated AAO was placed in a plasma chamber (Technics Model PE-IIA) and the chamber pressure was pumped down to 90 mTorr. CHF_3 gas was then flushed in until the pressure reached 100 mTorr. The power was set to 150 W and the etching time was 2 min. During the plasma etching, free fluorine was produced by electron impact in plasma, and reacted with SiO_2 to form SiF_4 in the gas phase, which was pumped away. Free-standing nanotubes were then released by dissolving the alumina template selectively in a 25% phosphoric acid solution. TEM images were taken with ZEISS EM10CA TEM microscope (Thornwood, NY) operating at 80 kV.

Figure 2.3 shows the TEM images of SNTs with different polishing method. It can be seen that the nanotubes obtained with dry etching did not have the residue shown at the entrance of the nanotubes obtained with mechanical polishing. The particles at the entrance could be ground silica particles produced during mechanical polishing.

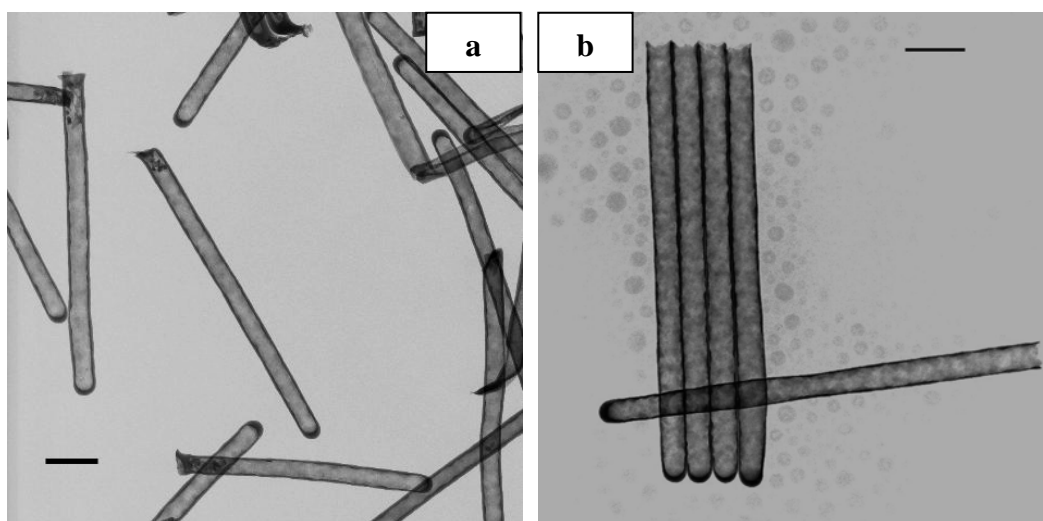


Figure 2.3 TEM images of silica nanotubes obtained with (a) mechanical polishing and (b) dry etching. Scale bar: 200 nm

2.2.2 Synthesis of superparamagnetic iron oxide nanoparticles in the silica nanotubes

Ammar *et al.*[85] have reported the synthesis of CoFe_2O_4 nanoparticles with a high crystallinity via a polyol method. Based on this method, we used $\text{FeCl}_3 \cdot 6\text{H}_2\text{O}$ as the precursor for the synthesis of SPIONs. Specifically, the SPIONs were prepared under reflux in 25 ml of 1,2-propanediol for 2 h in a 100 ml round-bottomed flask fitted with a condenser. Sodium acetate was used as the hydrolyzing agent. $\text{FeCl}_3 \cdot 6\text{H}_2\text{O}$ with concentrations ranging from 0.002 M to 0.01 M was used, while the concentration of sodium acetate was kept at three times the Fe concentration. 500 μl water was added in the 25 ml polyol medium for hydrolysis reactions. For the synthesis of MNTs, silica-coated alumina templates were introduced into the reaction media. After the reflux processes, the silica coated alumina templates were rinsed in ethanol and water. After removal of the silica coating on the top surfaces with mechanical polishing, the templates were selectively dissolved with 0.1 M NaOH solution. The SPION-loaded nanotubes were subsequently rinsed with ethanol and collected via filtration, and dispersed in water. For comparison, the SPIONs formed in the bulk solutions were also collected.

2.2.3 Characterization of superparamagnetic iron oxide nanoparticles and magnetic nanotubes

The template and MNT dimensions were characterized by field emission scanning electron microscopy (SEM, Hitachi S-4700) and ZEISS EM10CA transmission

electron microscopy (TEM). High resolution TEM images were taken with JEM-2100F Field Emission Transmission Electron Microscope operating at 200 kV with STEM (Scanning TEM) capability and Oxford Energy Dispersive X-Ray Spectrometry (EDS). The magnetic properties were characterized by using the Quantum Design (MPMS-XL) superconducting quantum interference (SQUID) magnetometer.

2.2.4 Iron content measurement

The iron content of the MNTs was assessed with NMR relaxometry [93, 94]. The T_2 relaxation time was measured with a custom-designed relaxometer (Southwest Research Institute, San Antonio, TX) at 23 °C and 1 Tesla. The relaxation times were collected using a Carr-Purcell-Meiboom-Gill (CPMG) pulse sequence with 500 echoes and inter-echo times of 1, 3, and 5 ms. A calibration curve was obtained by measuring $1/T_2$ with ferric chloride solutions with known concentrations. The solution was prepared by mixing a 500 μl ferric chloride solution with known concentration with 500 μl concentrated hydrochloric acid (HCl). To measure the Fe concentration of a MNT solution, a 500 μl MNT solution was mixed with 500 μl of concentrated HCl to dissolve iron oxide to free ferric ion and the relaxation time was obtained under the same conditions as for the standard solutions. The number of MNTs in the solution was estimated based on the surface area of the relative template with a pore density of $10^{10}/\text{cm}^2$. The iron content of a single MNT was thus determined as the average iron content of the MNTs dispersed in the solutions.

2.3 Results

2.3.1 Superparamagnetic iron oxide nanoparticles synthesized in the bulk solutions

Different concentrations of $\text{FeCl}_3 \cdot 6\text{H}_2\text{O}$ were used: 0.001, 0.005, 0.01 and 0.05M.

The concentration of sodium acetate was kept at three times of the concentration of $\text{FeCl}_3 \cdot 6\text{H}_2\text{O}$. 0.2 ml water was added in for the complete hydrolysis of the metal salt and compensated for the loss of water during the reflux processes. The TEM images of SPIONs formed with different precursor concentrations are shown in Figure 2.4. The SPIONs synthesized in bulk solution with 0.002 M iron precursor for 2 h reflux have a diameter of 5-10 nm, and 7-15 nm with 4 h reflux. Figure 2.5 shows the TEM images of SPIONs formed in bulk solutions with different reflux time.

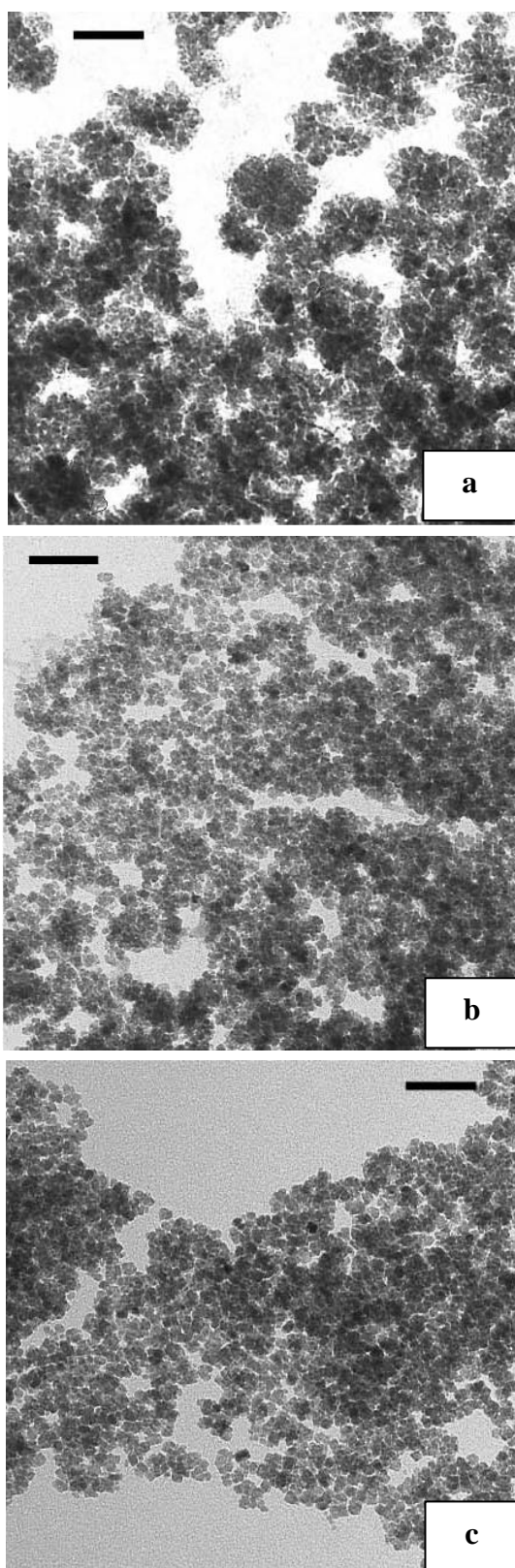


Figure 2.4 Transmission electron microscopy (TEM) images for the magnetite nanoparticles synthesized with different precursor concentrations: a) 0.05M, b) 0.01M, and c) 0.005M (Scale bar: 50 nm)

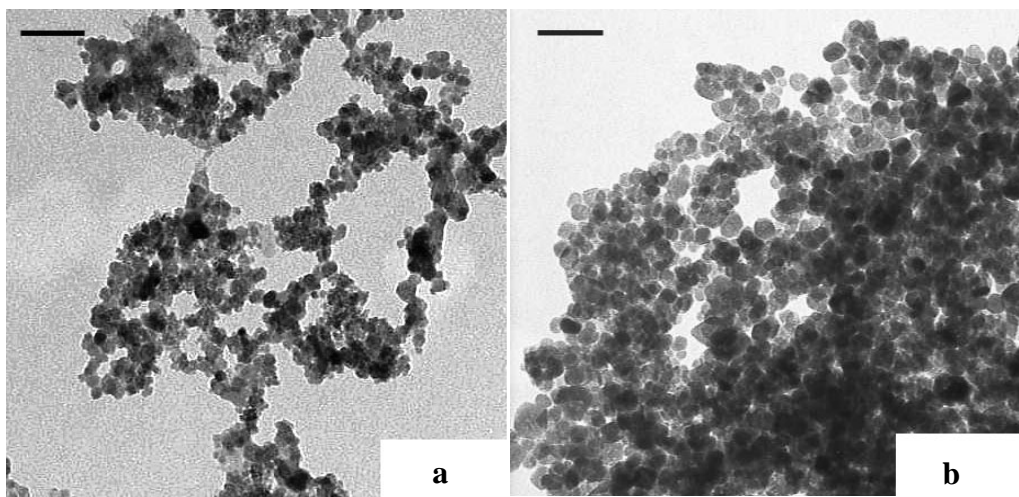


Figure 2.5 TEM images for superparamagnetic iron oxide nanoparticles (SPIONs) obtained with 2 hrs reflux (a) and 4 hrs reflux (b) in a 0.002 M iron precursor solution (scale bar: 50 nm)

2.3.2 Electron microscopy studies of magnetic nanotubes

The size of the SPIONs formed in the 2 μm -MNTs with the two-step reflux in 0.002M iron precursor solutions was about 3-7 nm based on TEM images. The difference in nanoparticle size between SPIONs formed in bulk and the SPIONs formed within MNTs indicates that the nucleation and growth processes of nanoparticles in the nanotubes might be different from the process in the bulk. The SEM images of the MNTs with 2-step reflux in iron precursor solutions with a concentration of 0.002 M are shown in Figure 2.6. The main element components of the MNTs were detected with Energy-dispersive X-ray spectrum (EDS). As shown in Figure 2.7, there are Fe, Si, O, Cu and C peaks. Fe, Si, and O peaks represent the composition of magnetic nanotubes. Cu and C peaks come from the specimen grid and the Formvar carbon supporting film.

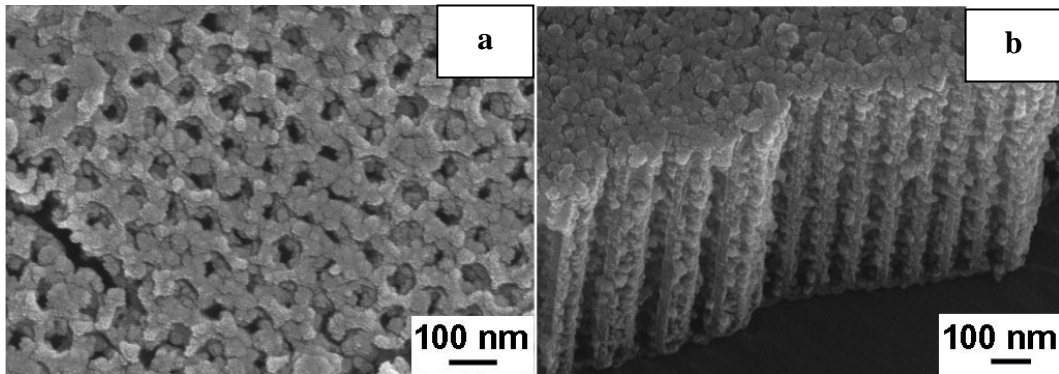


Figure 2.6 Scanning electron microscopy (SEM) images of the top view (a) and side-view (b) of 2 μm -magnetic nanotubes (MNTs, length: 2 μm , diameter: 70 nm) embedded in a AAO template.

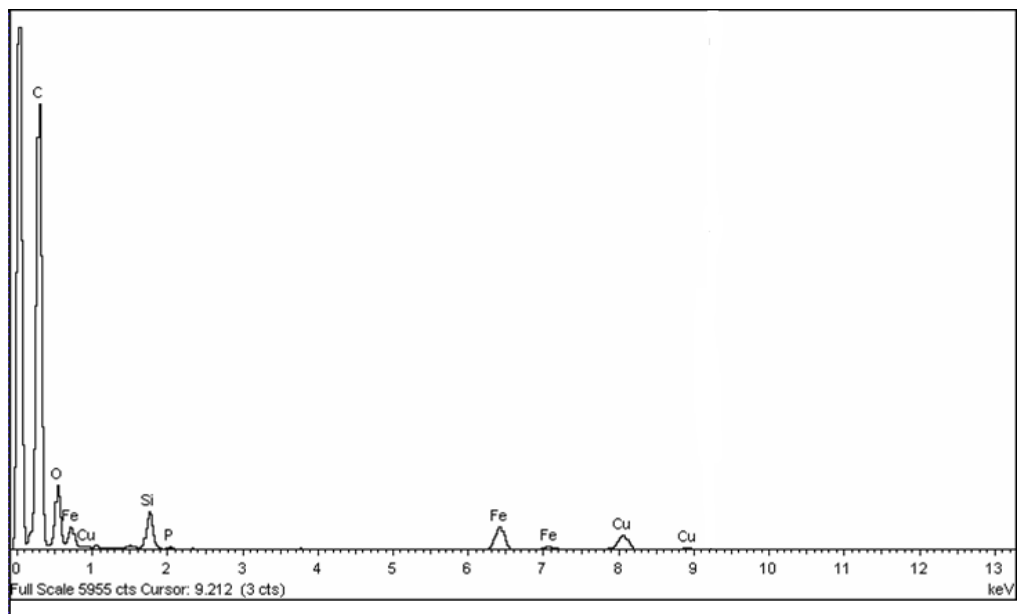


Figure 2.7 Energy-dispersive X-ray spectrum (EDS) of magnetic nanotubes. Fe, Si, and O peaks represent the composition of magnetic nanotubes. Cu and C peaks come from the specimen grid and the Formvar carbon supporting film.

The high resolution transmission electron microscopic (HR-TEM) image for MNTs was shown in Figure 2.8. The highlighted lattices have a d-spacing of 0.25 nm, which agrees well with the literature value of the interlayer distance between

the (3 1 1) lattice planes of magnetite [95]. However, the d-spacing values obtained from the diffraction pattern for maghemite ($\gamma\text{-Fe}_2\text{O}_3$) [96] are quite close to the values for magnetite (Fe_3O_4). It is hard to distinguish magnetite from maghemite just based on diffraction patterns. It is well known that the saturation magnetization (M_{sat}) of magnetite is much higher than the M_{sat} of maghemite [96]. The M_{sat} of our magnetic nanoparticles is on the highest side of reported values for magnetite nanoparticles by other groups [97]. This further provides evidence for the presence of magnetite as the main part of the SPIONs synthesized in this study.

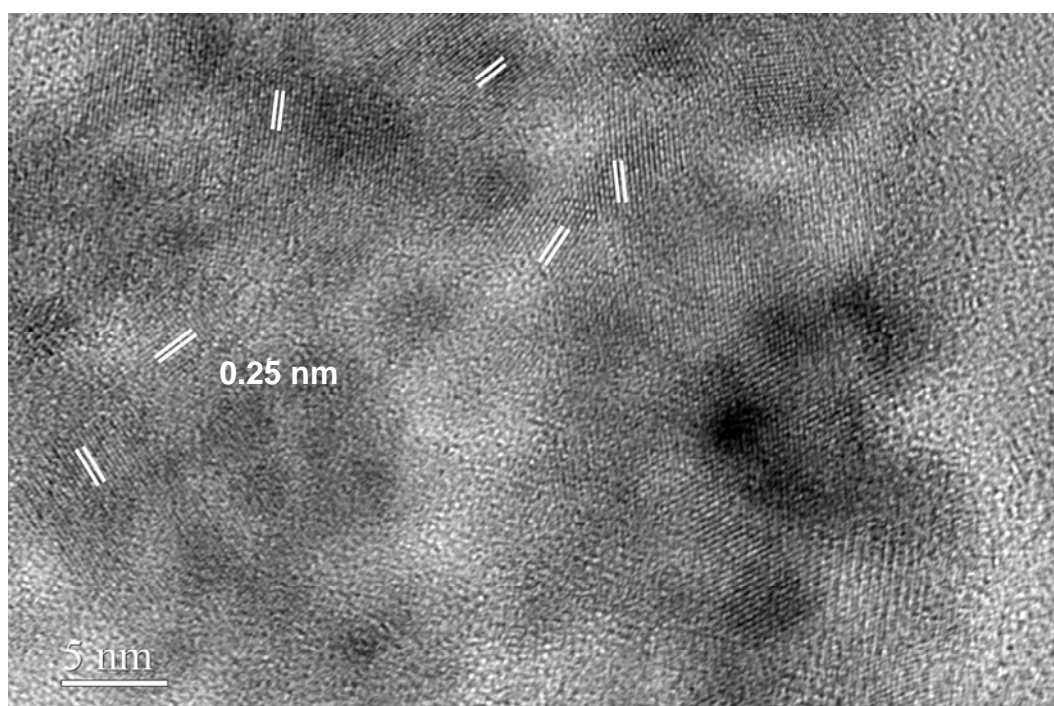


Figure 2.8 High resolution transmission electron microscopy (TEM) image for MNTs.

2.3.3 Iron content determination of magnetic nanotubes

The iron content of MNTs was determined with NMR relaxometry. The calibration curve is shown in Figure 2.9. The iron content of 2 μm -MNTs was measured to be 0.714 ± 0.187 fg/MNT after the first reflux in 0.002 M iron precursor solution, and increased to 1.367 ± 0.473 fg/MNT after the second reflux. The Fe content of 500 nm-MNTs was 2.013 ± 0.651 fg/MNT with a 3-step reflux. A multi-step reflux process was necessary to increase the loading of SPIONs.

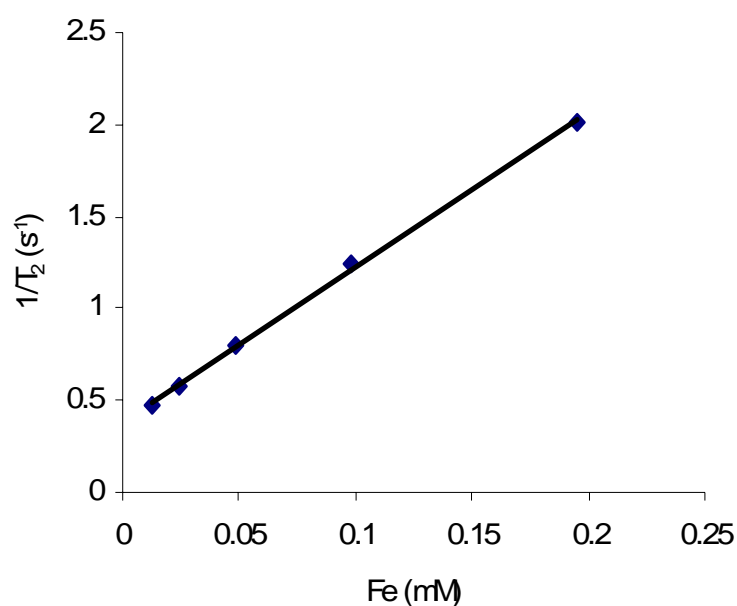


Figure 2.9 Calibration curve for relaxation rate ($1/T_2, \text{s}^{-1}$) as a function of iron concentration (C_{Fe}, mM): $1/T_2 = 8.4287 C_{\text{Fe}} + 0.3853$, with correlation coefficient of 0.999

The effect of surface modification was also studied. The iron content of the MNTs with different surface modifications was listed in Table 2.1. No significant difference was detected according to an F-test.

Table 2.1 The iron content of MNTs with different inner surface modifications

Modification of NT	Iron content (fg/NT)	
	One-step reflux	Two-step reflux
bare	0.714±0.187	1.367±0.473
PEG-	0.713±0.360	1.410±0.644
DETA-	0.534±0.276	1.294±0.757
EDTA-	0.610±0.158	1.497±0.371

2.3.4 Magnetization of superparamagnetic iron oxide nanoparticles and magnetic nanotubes

Figure 2.10 shows the distribution of SPIONs in ethanol with and without an external magnetic field. The magnetic-field (H) dependence of magnetization (M) taken at 300 K was shown in Figure 2.11. Neither the SPIONs nor the MNTs exhibited hysteresis, which is consistent with the superparamagnetic properties of iron oxide crystals. According to the SQUID results, the saturation magnetization (M_{sat}) of the synthesized SPIONs was as high as 98 emu/gFe. This value is greater than the reported M_{sat} values for dextran coated SPION ferumoxides (Feridex IVTM, 68 emu/gFe [98]) that is used clinically as a MR contrast agent. The M_{sat} of MNTs is 95 emu/gFe based on the iron content, and 30 emu/gMNT based on the

mass of MNTs, which is fifteen times greater than the M_{sat} of the previously reported magnetic nanotubes formed at room temperature (i.e., 2 emu/gMNT) [44]. This increase in M_{sat} results from the increased crystallinity of nanoparticles formed at the high temperature employed with the solvothermal method [99, 100]. The HR-TEM images shows that the SPIONs formed in the nanotubes and in bulk solutions are crystalline (Figure 2.8). The slight decrease of the M_{sat} of MNTs from that of SPIONs formed in the bulk demonstrated that the MNTs retained the magnetization of the SPIONs formed in bulk solutions.

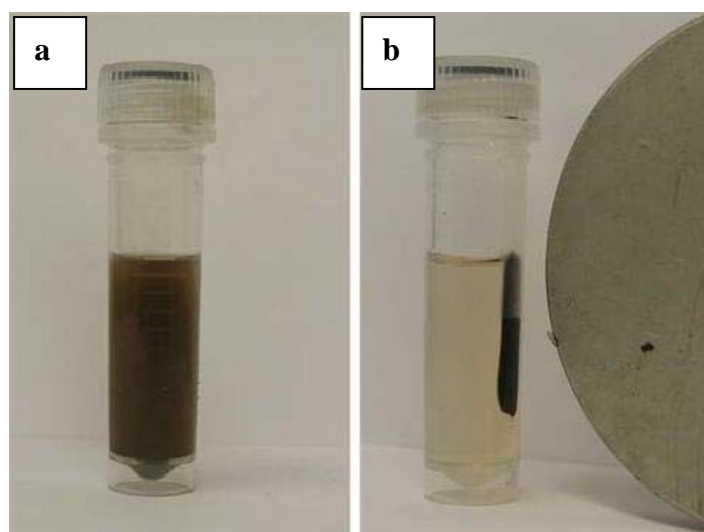


Figure 2.10 Magnetic nanoparticles in ethanol with (a) and without (b) external magnetic field

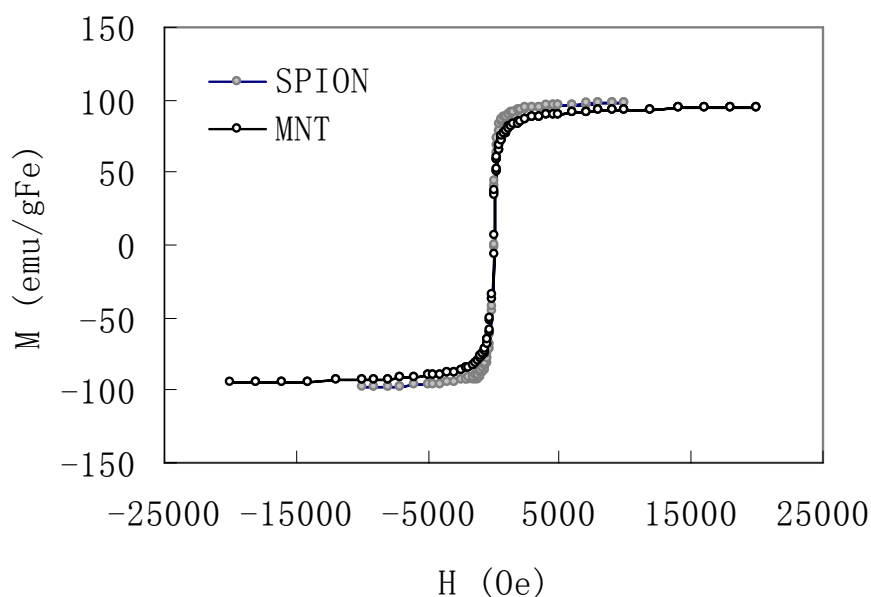


Figure 2.11 Magnetization (M) - magnetic field (H) relations ($T = 300$ K) of 2 μm -magnetic nanotubes (MNTs) synthesized by a two-step 2 hrs reflux in 0.002 M iron precursor solutions, and of superparamagnetic iron oxide nanoparticles (SPIOs) synthesized by a 4 hrs reflux in a 0.002 M iron precursor solution

The temperature dependence of zero field cooled magnetization (ZFCM) and field cooled magnetization (FCM) was measured at $H = 50$ Oe (Figure 2.12). At high temperatures, both the ZFCM and FCM increase during cooling and these two magnetization-temperature (M-T) curves overlap with each other. Below certain temperature, the ZFCM decreases during cooling and gives rise to a cusp in the ZFCM-T curve, while the FCM continues to increase. This thermomagnetic behavior is a typical characteristic of the superparamagnetic nanoparticle system. The temperature at which the ZFCM cusp is located is the so-called blocking temperature (T_B), which is related to the anisotropy energy (E_α) of the magnetic particles. According to the relation of $E_\alpha = K_{eff}V = k_B T_B$ [101], the higher the T_B ,

the larger the size of the particles can be, where K_{eff} is the effective magnetic anisotropy energy per unit volume and V is the average volume of the magnetic nanocrystal; k_B is the Boltzmann constant. Based on the blocking temperatures obtained, the average size of iron oxide crystals formed in 0.002 M precursor solutions with 4 hrs reflux ($T_B = 250\text{ K}$) is larger than that of the particles formed in nanotubes with 0.002 M precursor solutions with 4 hrs reflux in total ($T_B = 91\text{ K}$), which is consistent with the TEM studies. In addition to the intrinsic contributions, such as shape, magnetocrystalline, or stress anisotropies, particle interactions can modify the energy barrier [102]. The difference in the magnetic dipolar interaction can also contribute to the difference in T_B [101]. Generally, a flatter low-temperature FCM-T curve reflects stronger dipole-dipole interactions, so the nanoparticles formed in the bulk should have stronger dipole-dipole interactions than the MNTs. The SPIONs are present as clusters inside discrete SNTs. This separation by the nonmagnetic silica layer results in weak dipole-dipole interactions for the MNTs.

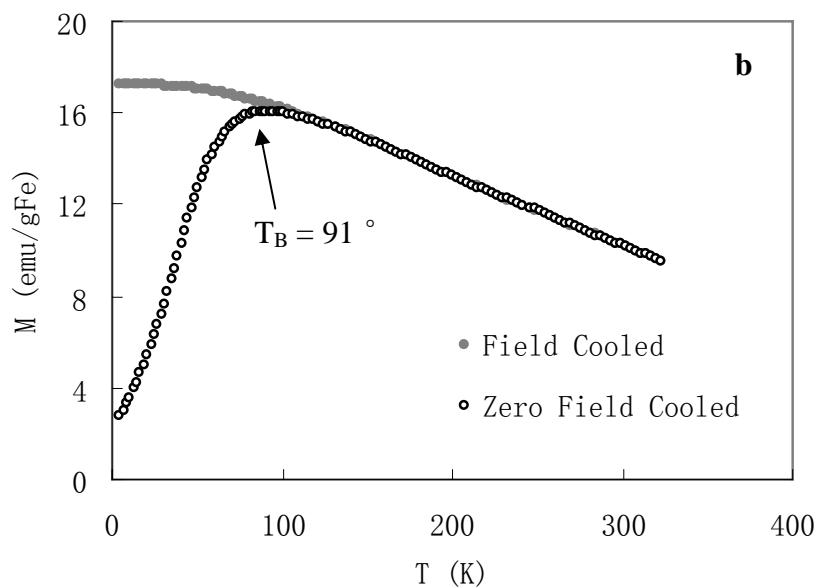
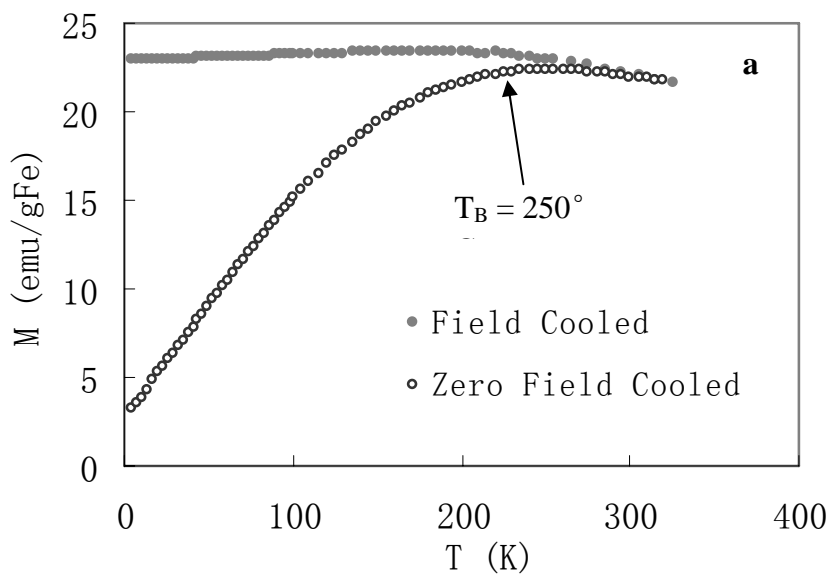


Figure 2.12 Field cooled (FC) and zero field cooled (ZFC) magnetization as a function of temperature for superparamagnetic iron oxide nanoparticles (SPIONs) obtained with 4 hrs reflux in 0.002 M iron precursor solutions (a), and 2 μm -magnetic nanotubes (MNTs) obtained from two-step reflux with the same iron precursor solutions (b).

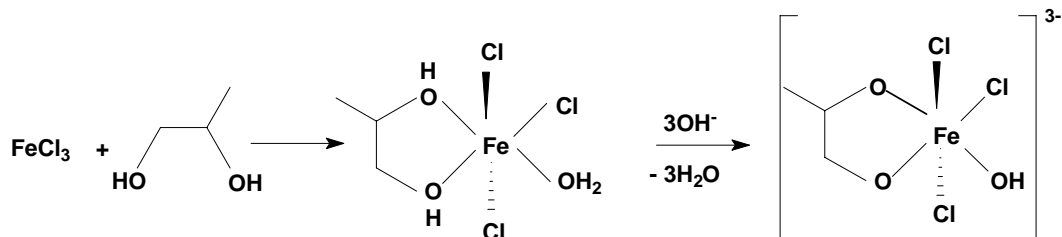
2.4 Discussion

2.4.1 Polyol method

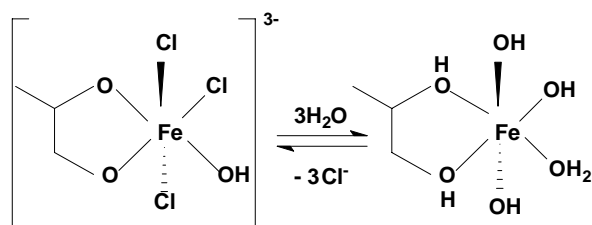
Fe_3O_4 was produced in the solvothermal system by modified reduction reactions between FeCl_3 and propane diol. Polyol has been used for preparing metal oxide nanoparticles functioning as a solvent, a reducing agent and a surfactant. The structure of this molecule is ideal for forming chelated complexes with metals when the molecules are deprotonated. Caruntu *et al.* have proposed the scheme for the complex formation and hydrolysis in diethylene glycol [86, 103]. Similarly, the scheme for the formation of magnetite in propane diol is proposed here.

Scheme 2.3 Formation of magnetite in propane diol: (a) complexation, (b) hydrolysis, (c) condensation

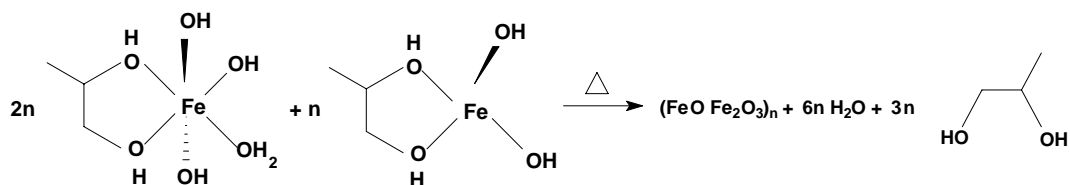
(a)



(b)



(c)



2.4.2 Formation of superparamagnetic iron oxide nanoparticles

At high temperatures with constant bubbling during the reflux process, the nucleation and growth processes are more controlled by thermodynamics, that is, reversible and collective phenomena, than by irreversible atomic scale

kinetics[104]. Nucleation starts with a supersaturated solution. The degree of supersaturation can be expressed by

$$S = C / C_{eq} \quad \text{Equation 2.1}$$

where C and C_{eq} are the solute concentrations at saturation and at equilibrium, respectively.

Nucleation starts with a supersaturated solution. The degree of supersaturation increases with the precursor concentration, resulting in a lower activation energy for cluster formation, and thus a higher nucleation rates [105].

According to the results of the TEM studies, the magnetic nanoparticles formed in bulk solution with a reflux of 2 hrs have a diameter of 5-7 nm; with 4 hrs reflux the diameter is 7-15 nm. The size difference between the SPIONs formed in the bulk and those formed in the nanotubes indicates that the nucleation and growth processes in the nanotubes might be different from the processes in the bulk. A higher viscosity and a lower dielectric constant have been observed in confined nanospaces [106-108]. This difference between nanopores and bulk may result in the retardation of nanoparticle growth in the pores compared to the bulk. Magnetic particles formed during the first reflux process may catalyze the growth of SPIONs in the nanopores during the subsequent refluxes. This can explain successful loading of magnetic nanoparticles with two-step reflux.

2.5 Conclusions

In this chapter, MNTs were prepared with considerably high saturation magnetization (95 emu/gFe). The high value of saturation magnetization is very

important for actual applications like MRI contrast agent, magnetic separation of drug molecules or cells, imaging-monitored drug delivery. The feasibility and efficiency of these applications are highly reliant on this parameter. The synthesis method introduced in this work is quite simple and does not require laborious washing and purification steps.

The structure of MNTs integrates the characteristics of SNTs, such as facile chemistry, mechanical robustness, biocompatibility, and well-controlled dimensions, with the high saturation magnetization of SPIONs, making the MNTs an ideal candidate for imaging-monitored drug delivery.

Chapter 3: Magnetic Nanotubes as Magnetic Resonance

Contrast Agents

This chapter has been reproduced in part with permission from Bai, X; Son, SJ; Zhang, SX; Liu, W; Jordan, EK; Frank, JA; Venkatesan, T; Lee, SB, Synthesis of superparamagnetic nanotubes as magnetic resonance imaging contrast agents and for cell labeling. *Nanomedicine* 3(2): 163-174.

3.1 Introduction

Magnetic resonance imaging (MRI) has been used to produce high-resolution three-dimensional images of the inside of the human body primarily for medical purposes[109]. MRI is based on the principles of nuclear magnetic resonance (NMR). Differential contrast depends on endogenous differences in water content and relaxation times of the tissue of interest. Contrast agents such as gadolinium chelates, are used to increase the specificity of MRI. Such agents have been successfully used for the imaging of blood perfusion and vascular permeability [110]. However, the sensitivity of MRI is low and high local concentrations of the contrast agent are required to generate detectable MR contrast. The contrast agents should, therefore, be characterized by high relaxivity[111].

3.2 Basics of magnetic resonance spectroscopy

3.2.1 Physics of magnetic resonance

Protons are charged particles and possess a characteristic dipolar magnetic moment around their axis. In the absence of an applied magnetic field, the magnetic moment of each proton is randomly oriented in space. When a magnetic

field B_0 is applied in a direction, the z component of the individual magnetic moments of each proton will align either parallel or anti-parallel to the applied field. The parallel orientation is the lower energy state and the anti-parallel one is at the high energy state. The ratio of the populations of protons at these two energy states can be estimated with Boltzmann's equation (Equation 3.1).

$$N_l / N_h = \exp(\Delta E / kT) \quad \text{Equation 3.1}$$

where N_l is the number of protons in the lower energy state and N_h is the number of protons in the higher energy state. T is the absolute temperature (K) and k_B is Boltzmann's constant ($1.3181 \times 10^{-23} \text{ JK}^{-1}$). ΔE is the energy difference between the two energy states, which is proportional to the applied field strength. At equilibrium, the net magnetization vector lies along the direction of the applied magnetic field B_0 and is called the equilibrium magnetization M_0 . The magnetization vector M_0 precesses about B_0 , as shown in Figure 3.1.

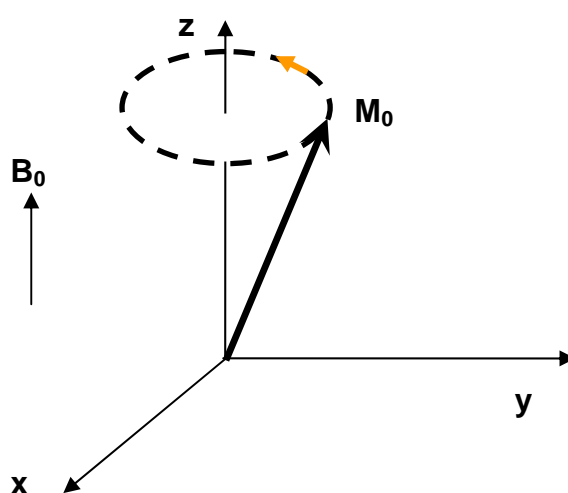


Figure 3.1 Spin of magnetization vector (M_0) with the applied magnetic field (B_0)

There is a simple linear relationship between the magnetic field experienced by the protons and the resulting angular frequency of precession, ω_0 , of the magnetization, as described by the Bloch equation (Equation 3.2).

$$\omega_0 = \gamma B_0, \quad \text{Equation 3.2}$$

where γ is the gyromagnetic ratio which is unique for each nucleus possessing a spin, and ω_0 is the Larmor frequency associated with the spin energy transitions (ΔE) induced by the magnetic field.

The net magnetization vector M_z , the magnitude of M_0 in the z -direction, is small compared to the applied field. M_z can absorb energy from radio frequency (RF) radiation, such as a RF 90° pulse. When the RF source is removed, the protons relax or return to a state of equilibrium and emit energy to the surrounding nuclei, as shown in Figure 3.2. This is T_1 relaxation or “spin-lattice” relaxation. T_1 is the time for the magnetization to return to $1/e$ of its original magnitude (M_0). The behavior of the M_z is described by Equation 3.3.

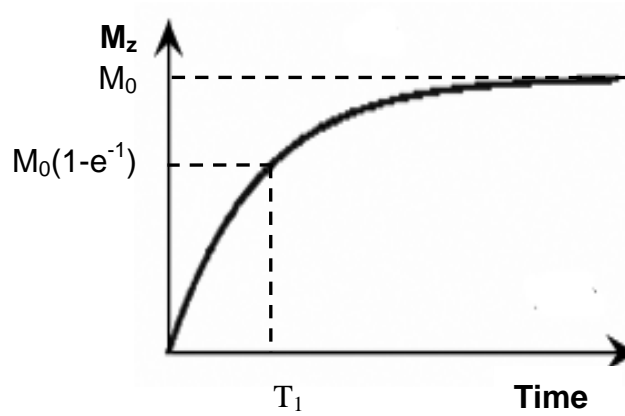
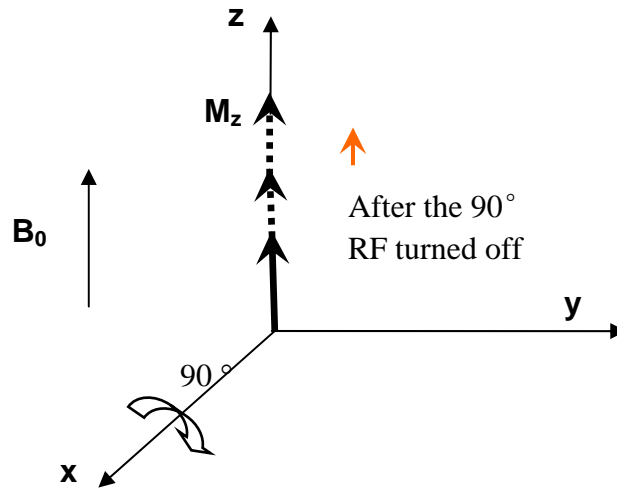


Figure 3.2 T_1 relaxation with a RF 90° pulse

$$M_z(t) = M_0(1 - e^{-t/T_1})$$

Equation 3.3

The net magnetization is placed along the $-z$ direction when a RF 180° pulse is applied, as shown in Figure 3.3. The behavior of the M_z is then described by Equation 3.4.

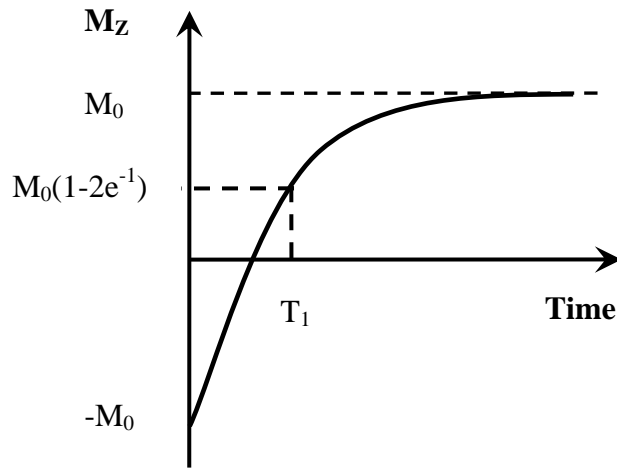
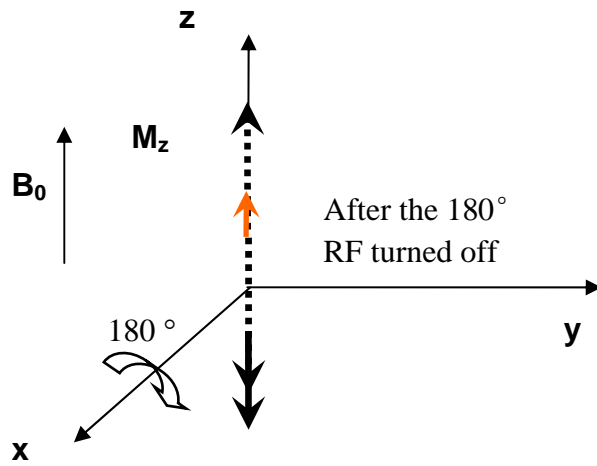


Figure 3.3 T_1 relaxation with a RF 180° pulse

$$M_z(t) = M_0(1 - 2e^{-t/T_1})$$

Equation 3.4

T_2 relaxation or “spin-spin” relaxation occurs when spins at the high and low energy states exchange energy but do not lose energy to the surrounding lattice. However, the magnitude of the transverse magnetization (M_{xy}) decreases. This is

due to a loss of phase coherence, called dephasing, as shown in Figure 3.4. The behavior of the M_z is then described by Equation 3.5. Two factors contribute to the dephasing. One is molecular interactions, which leads to a pure T_2 relaxation. The other is variation in B_0 , which leads to an inhomogeneous T_2 effect ($T_{2inhomo}$). The time constant for the decay caused by the combination of these two factors is given as T_2^* . The relationship between the T_2 and T_2^* can be described as Equation 3.6.

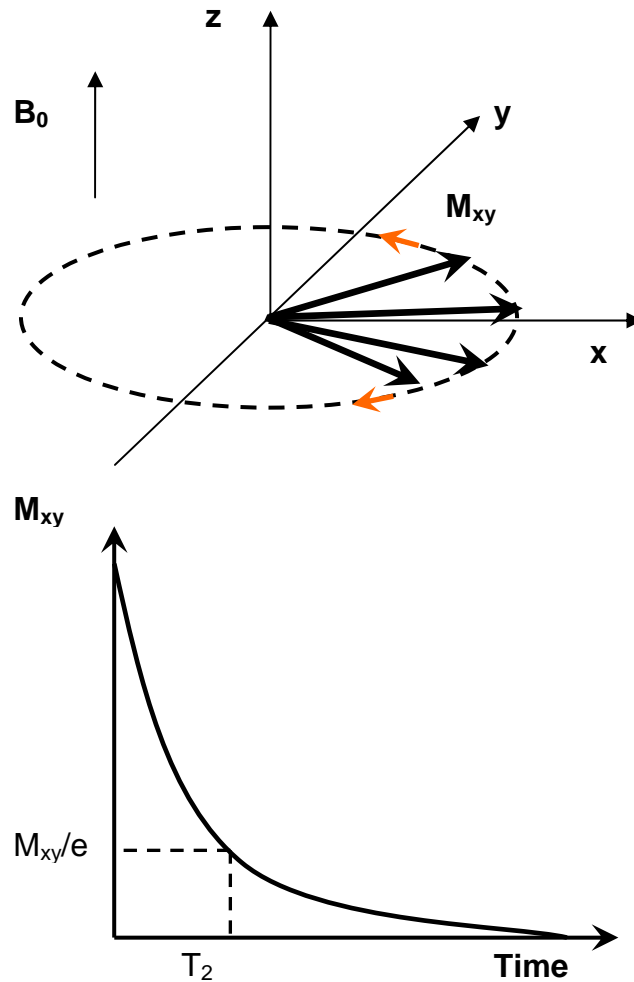


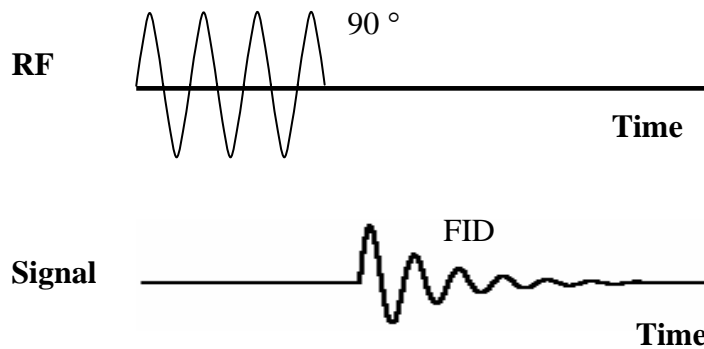
Figure 3.4 T_2 relaxation

$$M_{xy}(t) = M_{xy_0} e^{-t/T_2} \quad \text{Equation 3.5}$$

$$1/T_2^* = 1/T_2 + 1/T_{2in\ homo} \quad \text{Equation 3.6}$$

3.2.2 Measurement of relaxation times

Free induction decay (FID) is a form of magnetic resonance signal from the decay of transverse magnetization. It is measured by a coil placed along the x axis.



Longitudinal relaxation, T_1

The T_1 values can be measured using the sequence defined as

$$[90_x^0 - TR - 90_x^0(FID) - T_D]_n$$

Where 90_x^0 is the 90° RF pulse along x-axis. TR is the repetition time, the time between the 90° pulses. $90_x^0(FID)$ is the measurement of MR signal of the recovered M_z during the TR time. T_D is a delay time and n is the repetition times of the sequence. In this sequence, a 90° RF pulse is applied to rotate M_z to the xy-plane. A second 90° RF pulse is applied to rotate the recovered M_z , the relaxed spins, during the TR time back to the xy-plane for measurement. The T_D value is

generally 3 to 5 times of T_1 . M_z will be completely recovered or close to M_0 after T_D . In each measurement the TR values are changed to generate a plot of signal intensity versus time (Equation 3.7).

$$M_z(TR) = M_z(0)(1 - e^{-TR/T_1}), \quad \text{Equation 3.7}$$

where $M_z(TR)$ is the amplitude of the magnetization at TR, $M_z(0)$ is the amplitude of the magnetization at time zero. T_1 can also be determined with inversion recovery sequence, such as Philips Look-Locker sequence. The sequence is defined as

$$[180_x^0 - \tau - 90_x^0 (FID) - T_D]_n,$$

where τ is the time between the 180° and 90° pulses. In this sequence, a 180° RF pulse is used instead of a 90° RF pulse. The signal is measured as a function of τ (Equation 3.8).

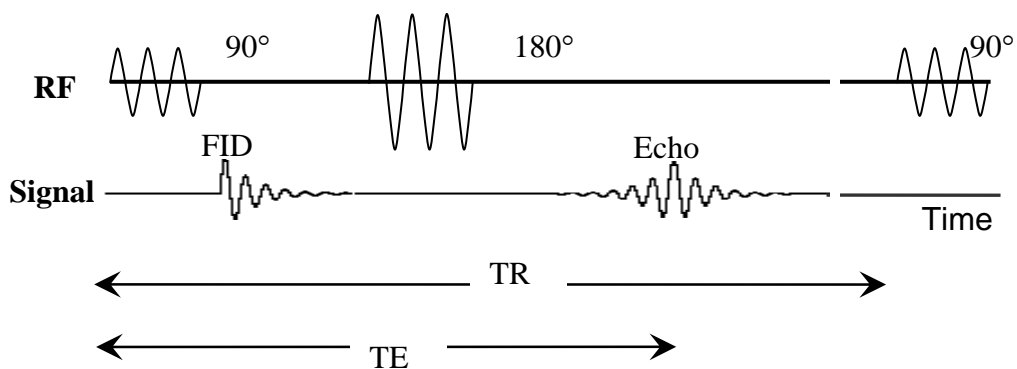
$$M_z(\tau) = M_z(0)(1 - 2e^{-\tau/T_1}) \quad \text{Equation 3.8}$$

Transverse relaxation, T_2

Spin-echo sequences are used to measure T_2 values or for T_2 -weighted imaging by minimizing T_2^* effects. The sequence is defined as

$$90_x^0 - [\frac{1}{2}TE - 180_y^0 - \frac{1}{2}TE - (Echo)]_n$$

A RF 90° pulse is applied to rotate the magnetization to the xy -plane, M_{xy} . A RF 180° pulse along the y -axis is then applied after one half of an echo time (TE) to refocus the spins that have dephased due to the inhomogeneities of the magnetic field. If the field inhomogeneity is present for the first $1/2$ TE delay, the same inhomogeneity is present for the second $1/2$ TE after the 180° pulse and will influence the precession in the same manner. The effect of inhomogeneities of the magnetic field on the dephasing of M_{xy} can thus be cancelled out at the center of the echo where the spins are back in phase and the value of the echo reflects the T_2 effects on the dephasing of the spins. The 180° pulse is often referred to as the refocusing pulse. The dephasing that occurs after the RF 90° pulse and on either side of the echo center is due to T_2^* effects. The echo time (TE) is the time between the RF 90° pulse and the formation of the echo. The repetition time (TR) is the time between the successive RF 90° pulses. The process is repeated n times to produce an echo train. The sequence is called a Carr-Purcell-Meiboom-Gill (CPMG) spin echo sequence.



The T_2 value can be calculated as a function of echo time, according to Equation 3.9.

$$M_{xy}(TE) = M_{xy}(0)e^{-TE/T_2} \quad \text{Equation 3.9}$$

T_2^* relaxation

As mentioned before, T_2^* relaxation is caused by both the T_2 relaxation and the dephasing by magnetic field inhomogeneities (Equation 3.6). T_2^* weighted MRI is commonly used in the presence of superparamagnetic nanoparticles as contrast agents in tissues. The gradient recalled echo (GRE) sequence is used for T_2^* weighted MRI. A RF pulse is used to rotate the magnetization by an angle typically of between 10° and 90° . Then, a gradient is used to rephase the spins in the GRE sequence. The GRE sequence is intrinsically more sensitive to magnetic field inhomogeneities because of the use of the refocusing gradient. Comparing to the spin echo sequence, GRE uses a small flip angle to rotate the magnetization and a gradient instead of a 180° RF pulse to refocus magnetization vectors. This gives the sequence a time advantage over the T_1 and T_2 weighted imaging. It is widely used for fast scan images. T_2^* can be calculated from the exponential decay rate of FID (Equation 3.10), as shown in Figure 3.5.

$$T_2^* = \Delta TE / \ln\left(\frac{SI(TE1)}{SI(TE2)}\right), \quad \text{Equation 3.10}$$

where $SI(TE1)$ and $SI(TE2)$ are the measured signal intensities at the first echo time ($TE1$) and the second echo time ($TE2$), respectively. $\Delta TE = TE2 - TE1$. The signal intensity (SI) is measured from a region of interest (ROI), determined from the MR image. It can also be determined directly from the line width of the proton peak obtained in the Fourier Transform NMR frequency spectroscopy.

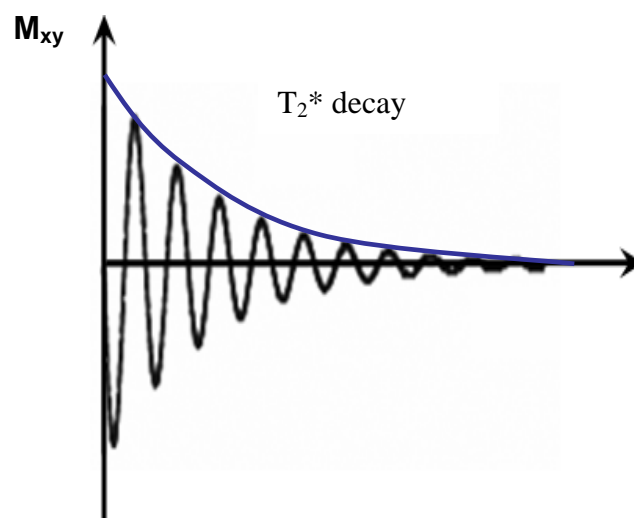


Figure 3.5 T_2^* decay

3.3 Magnetic resonance contrast agents

The MRI contrast is due to the response of protons to an external magnetic field. The relaxation of the protons is dependent upon the local environment, such as temperature and viscosity. Different tissue will relax at different rates. MRI contrast is determined by the difference in proton relaxation rates and proton densities within various tissues (Figure 3.6). Despite the inherent contrast, contrast

agents are required to enhance the contrast by increasing proton relaxation rates. Generally, there is a linear relationship between the relaxation rate and the contrast agent concentration (Equation 3.11).

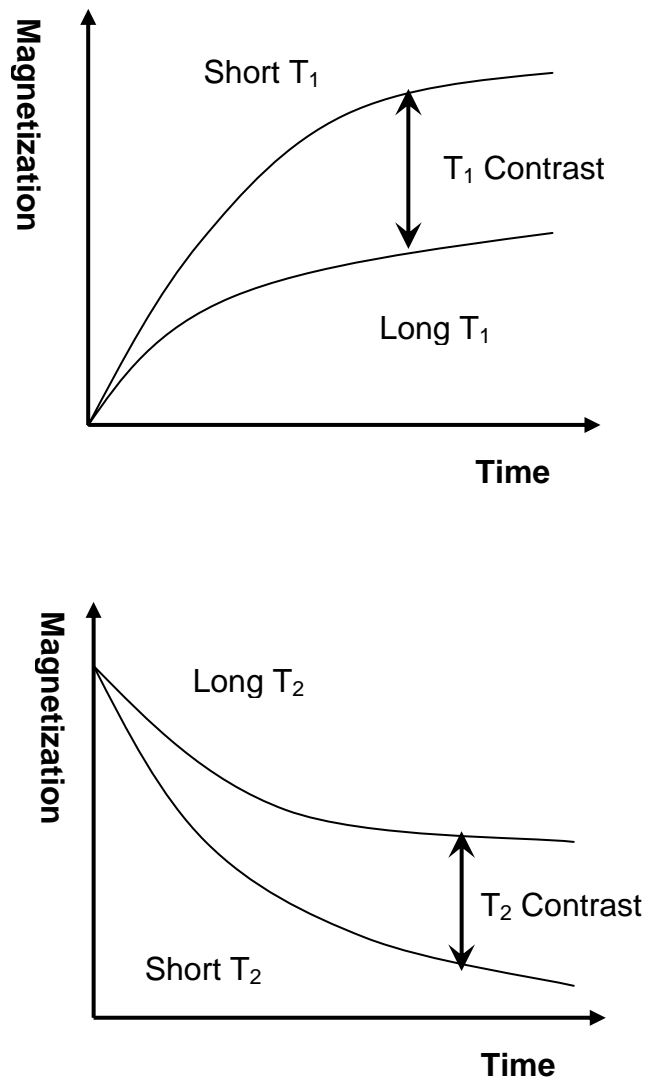


Figure 3.6 T₁ and T₂ contrast

$$R_{1or2} = r_{1or2}C + R_{0,1or2},$$

Equation 3.11

where $R_{1 \text{ or } 2}$ is the relaxation rate in the presence of contrast agent, $r_{1 \text{ or } 2}$ is the relaxivity of the contrast agent with a unit of $s^{-1}mM^{-1}$, C is the concentration of contrast agent, $R_{0,1 \text{ or } 2}$ is the relaxation rate of the sample without contrast agent.

MRI contrast agents can be classified as positive contrast agents and negative contrast agents according to the increase or decrease of signal intensity in the presence of the agent. All contrast agents will enhance both T_1 relaxation and T_2 relaxation. Whether the signal intensity is increased or decreased is dependent upon which effect predominates. The positive contrast agents can increase signal intensity on T_1 weighted images by decreasing T_1 more significantly than T_2 . They are typically paramagnetic agents that produce only weak local magnetic fields and therefore weak enhancement on T_2^* . These agents are generally small molecular weight compounds containing elements that have unpaired electron spins in their outer shells, such as gadolinium, manganese and dysprosium. They are chemically linked to carrier molecules since gadolinium and dysprosium free ions are quite toxic. These agents can be eliminated without any significant biotransformation in the body. Negative contrast agents are mostly particulate aggregates composed of a magnetic core, usually magnetite (Fe_3O_4) or maghemite ($\gamma-Fe_2O_3$), and a shell of polymer, dextran, polyethyleneglycol. Superparamagnetic iron oxide (SPIO) and ultrasmall iron oxide particles (USIO) are the two main types of negative contrast agents. These agents produce predominantly spin-spin relaxation effects. SPIO refers to particles with aggregated iron oxide cores and has a mean hydrated particle diameter greater than

50 nm. USIO particles are made up of single crystalline iron oxide cores with a mean hydrated particle diameter less than 50 nm.

3.4 Magnetic nanotubes as magnetic resonance contrast agents

Superparamagnetic iron oxide nanoparticles (SPIONs) have been recognized as promising and powerful candidates for applications in medical and biotechnological fields, such as magnetic resonance imaging (MRI), cellular therapy, tissue repair, targeted drug delivery, *etc.*[73, 76, 112-116]. There is an increasing interest in MRI to monitor *in vivo* temporal and spatial migration behavior of the transplanted cells labeled with SPIONs [47, 117-120]. MRI is a noninvasive *in vivo* molecular imaging technique that provides a way to assess anatomy and function of tissues. However, one drawback of MRI is the low sensitivity and need for micromolar concentration of contrast agents in tissues [121]. The addition of MRI contrast agents increases the sensitivity to detect tumors at a very early stage, that would be otherwise undetectable with conventional imaging protocols [76].

An ideal MR contrast agent should have a high magnetic moment, high colloidal stability, biocompatibility, long circulation time, and efficient surface functionality [73]. The high-performance magnetic nanoparticles depend highly on their physico-chemical properties, such as size, surface modification, and crystallinity, which are closely related with their synthetic methods. Dextran-coated SPIONs have been used as MRI contrast agents to label cells *ex vivo* [119]. These SPION contrast agents are generally trapped and accumulated by the

reticuloendothelial cells in the liver with a short half-life time in blood. The rapid biodegradation and clearance make it hard for long-term monitoring of the migration of these labeled cells in a biological system. Interestingly, it has been reported that the cylindrical shape of nanoparticles is able to sustain a drug delivery with a longer half-life time compared to nanospheres [72]. Sparring effect of nanotubes resulting in high efficiency in drug-delivery has been demonstrated [28].

Considering the unique characteristics of MNTs, as described in Chapter 2, the relaxivities of the MNTs prepared with polyol method were studied in this chapter. The results suggest that the MNT with a unique physical structure and high MR relaxivities make it suitable for use as a MRI contrast agent.

3.5 Methods

MNTs were embedded homogenously in phantoms (a 2% agarose gel). T_1 and T_2 relaxivities were measured on a clinical 3T MR scanner (Acheiva, Philips Medical System, Best, The Netherlands) using a dedicated 7 cm rat solenoid receive only RF-coil (Philips Research Laboratories, Hamburg, Germany). A T_1 relaxation map was acquired with a Look-locker sequence with 40 phases, echo time $TE = 7$ ms, repetition time $TR = 5000$ ms, flip angle = 10° . A T_2 map was acquired with a multi spin echo sequence with 11 echoes, $TE = 7.2$ ms, $TR = 1000$ ms. A T_2^* map was acquired with a multiple gradient echo sequence with 15 echoes: $TR = 1000$ ms, flip angle = 30° , TE of the first echo = 4.8 ms and inter echo step = 3.4 ms. All images were acquired with field of view = $100 \text{ mm} \times 100 \text{ mm}$, scan matrix =

192 × 192, reconstructed matrix = 256 × 256, slice thickness = 1 mm, number of excitations = 1. T₁, T₂ and T₂^{*} were calculated by mono-exponential fitting with custom-designed IDL software. The reported relaxation time was measured as the average over a regional of interest. The iron content of each sample was determined with a custom-designed relaxometer (Southwest Research Institute, San Antonio, TX) at 23 °C and 1 Tesla, as described in Chapter 2.

3.6 Results and discussions

Superparamagnetic nanoparticles generate contrast by shortening the NMR relaxation times. The efficacy of a MR contrast agent is commonly evaluated in terms of its relaxivities (r₁ or r₂), a measure of how much the proton relaxation rate is increased with the concentration of contrast agent. r₁ and r₂ are defined as the T₁ (spin-lattice) relaxivity and T₂ (spin-spin) relaxivity, respectively. They are determined from the linear relationship between the relaxation rates (R_{1 or 2} = 1/T_{1 or 2}) and the concentration of the contrast agent (C), that is, $R_{1\text{ or }2} = R_{1\text{ or }2}^0 + r_{1\text{ or }2}C$ (where, R_{1 or 2}⁰ is the relaxation rates in the absence of contrast agent). The relationships between the relaxation rates and the concentration of the MNTs are shown in Figure 3.7. Table 1 summarizes the T₁ and T₂ (*) relaxivities of the 500 nm- and 2 μm-MNTs along with the FDA approved MRI contrast agent ferumoxides (Feridex IV; Berlex Laboratories, Wayne, NJ). The r₂ to r₁ ratios for the 500 nm-MNTs (r₂/r₁ = 175) and 2 μm-MNTs (r₂/r₁ = 134) are greater than the ratio of the ferumoxides (r₂/r₁ = 35) measured under the same conditions. This may due to the increased loading of SPIONs in the MNTs. A similar trend has

been reported by Martina *et al.* [122] and Berret *et al.* [123]. T_2^* weighted MRI is commonly used to detect the presence of SPION in tissues. The variation of the magnetic field in the presence of MNTs results in local magnetic susceptibility inhomogeneities and causes an increased loss of phase coherence of proton spins. This effect leads to an increase of T_2^* relaxation compared to surrounding environment and hypointense regions on T_2^* weighted MRI. MNTs have an r_2^* ($628 \text{ mM}^{-1}\text{s}^{-1}$ for 500 nm MNTs, and $946 \text{ mM}^{-1}\text{s}^{-1}$ for 2 μm MNTs) greater than that for ferumoxides ($r_2^* = 344$). The results indicate that the clustering of magnetic nanoparticles in discrete nanotubes enhanced the r_2 , the ratio r_2/r_1 and the ratio of r_2^*/r_1 , which increases the MNTs utility as a T_2 and T_2^* contrast agent [122, 123]. Figure 3.8 shows the T_2 - and T_2^* -weighted images of the phantom with a series of MNT concentrations obtained at 3 Tesla.

Table 3.1 Relaxivities r_1 , r_2 and r_2^* of ferumoxide and magnetic nanotubes (MNTs) for T_1 -, T_2 - and T_2^* - weighted imaging.

System	Fe content	r_1 ($\text{mM}^{-1}\text{s}^{-1}$)	r_2 ($\text{mM}^{-1}\text{s}^{-1}$)	r_2^* ($\text{mM}^{-1}\text{s}^{-1}$)	r_2/r_1
	fgFe/MNT				
ferumoxide	-	6.5 ± 0.6	226 ± 27	344 ± 13	35
500 nm-MNT	2.013 ± 0.651	1.6 ± 0.3	264 ± 56	628 ± 90	175
2 μm -MNT	1.367 ± 0.473	3.0 ± 1.3	358 ± 65	942 ± 216	134

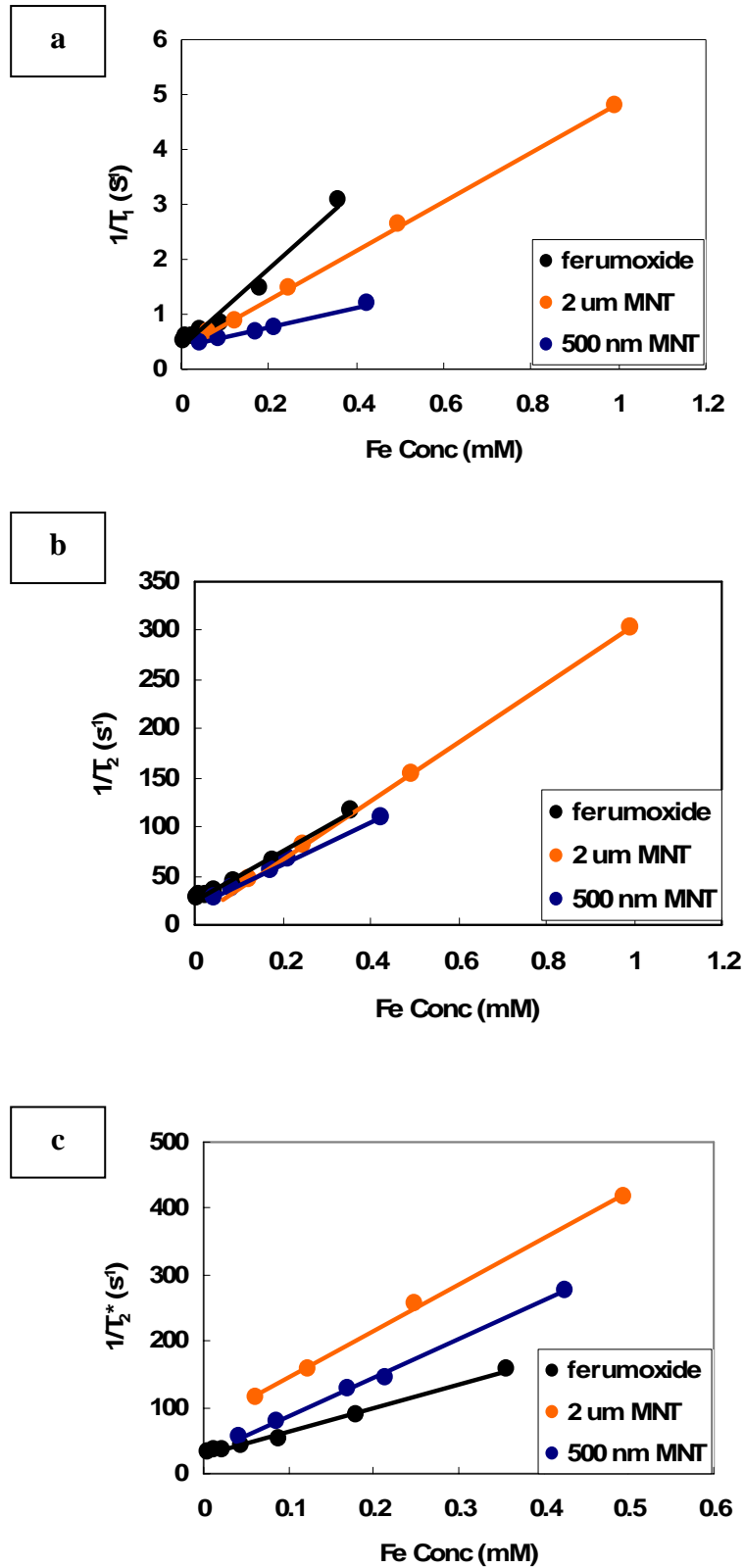


Figure 3.7 Relaxation rates as a function of iron concentration (mM): (a) T_1 relaxation rates ($1/T_1, s^{-1}$), (b) T_2 relaxation rates ($1/T_2, s^{-1}$), and (c) T_2^* relaxation rates ($1/T_2^*, s^{-1}$) (correlation coefficient is higher than 0.99).

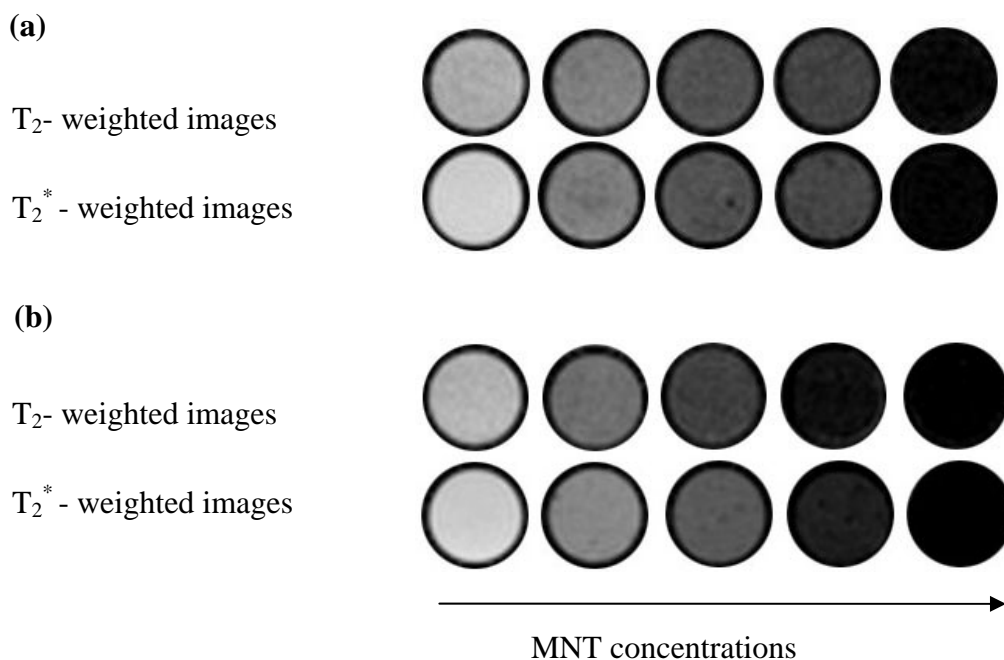


Figure 3.8 T_2 - and T_2^* - weighted images for phantoms dispersed with (a) 500 nm-magnetic nanotubes (MNTs) with concentration of 0, 2.4, 4.7, 9.5 and 19 pM (Fe concentration of 0, 0.085, 0.170, 0.213 and 0.426 mM), respectively, and with (b) 2 μ m-MNTs with concentration of 0, 3.3, 6.5, 13 and 26 pM (Fe concentration of 0, 0.062, 0.124, 0.248, and 0.495 mM), respectively.

3.7 Conclusions

In this work, I demonstrated that MNTs enhanced proton magnetic resonance relaxation rates, especially r_2^* , that are comparable with those of commercially available MR contrast agents. The r_2/r_1 ratio of MNTs is greater than ferumoxides and would indicate that the presence of MNTs could potentially lead to increased changes in contrast enhancement as compared to clinically approved T_2^* -weighted MRI contrast agents.

Chapter 4: Loading and Release of Doxorubicin with Magnetic Nanotubes

4.1 Introduction

It is well documented that endocytosis is the main pathway for the uptake of macromolecules and particles from the surrounding medium[52]. The process involves endosome and lysosome internalization, where the pH can be as low as 5.5-6.0 in the endosome and 4.5-5.0 in lysosomes[12, 125]. Therefore, drug carriers responsive to pH can be designed to selectively release their payload in tumor tissue cells for lysosomotropic delivery (Figure 4.1). Several different approaches have been reported, such as covalently conjugating drug molecules to drug carriers through a proteolytically cleavable bond or a hydrolytically unstable bond [126-129]. Another approach is to incorporate amines or carboxylic acids into block copolymers to form pH-sensitive micelles whose formation is altered by the protonation of these groups [130-132].

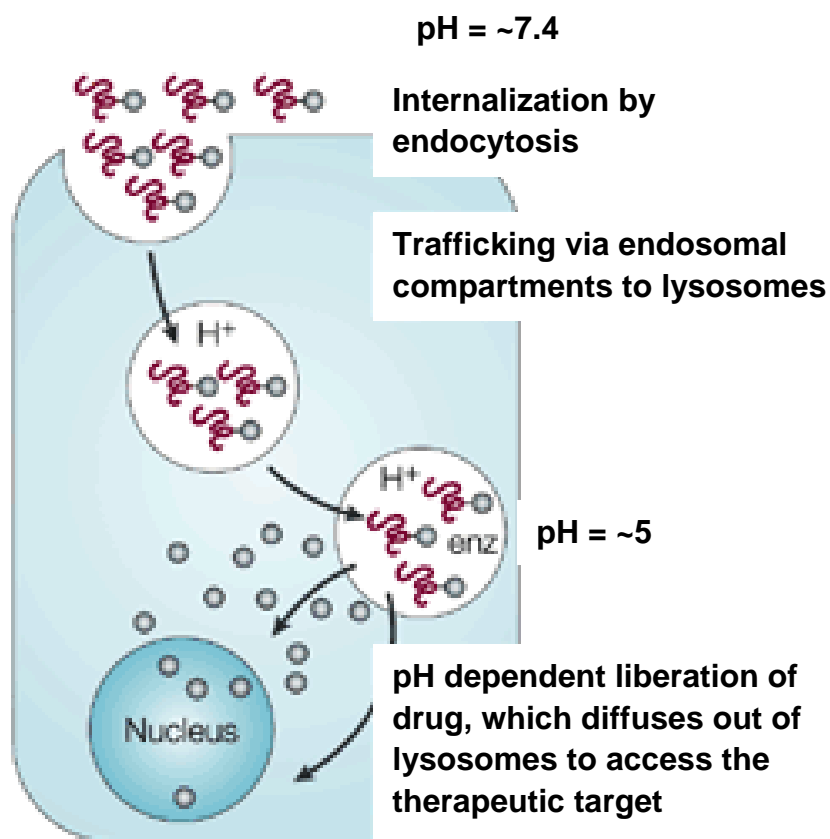


Figure 4.1 Lysosomotropic delivery (Duncan, Nature Reviews Cancer (2006))

In this study, Doxorubicin (Dox) was used as the model anticancer drug. Dox can be used to treat breast, ovarian and bronchial cancers by inhibiting the synthesis of nucleic acids in cancer cells. However, Dox has a very narrow therapeutic index and its use is thus limited [124]. Encapsulation of Dox provides a way to reduce toxicity through selective targeting and controlled release. In this chapter, loading and release of Dox is studied by controlling the bonding strength of the drug molecules to the magnetic nanotubes.

Kataoka *et al.* studied the pH effect on the partition of Dox in aqueous/chloroform phases[131]. This result shows that the Dox partition coefficient varies with pH.

At $\text{pH} > 7$, Dox partitioning into the chloroform phase is higher than 90%. When $\text{pH} < 5.5$, the partition into chloroform phase is about 10% (Figure 4.2). According to these data, the release of Dox can be adjusted by pH. Ideally, nanotubes loaded with Dox will not release the drug during circulation in the blood, where $\text{pH} > 7$. Once the nanotubes are taken up by the cancer cells, the drug will be released in an acidic environment. The pK_a value of pyridine in water is 5.3 [133]. It will be protonated when pH is less than 5.3 and will be in neutral form when the pH is around 7. When the pH is less than 5.3, Dox will also be protonated. For pyridine modified nanotubes, there will be charge-charge interaction and Dox will tend to leave the nanotubes at acidic pH . When the $\text{pH} > 7$, there will be a hydrophobic interactions between Dox and pyridine that assists in holding the drug in the nanotubes.

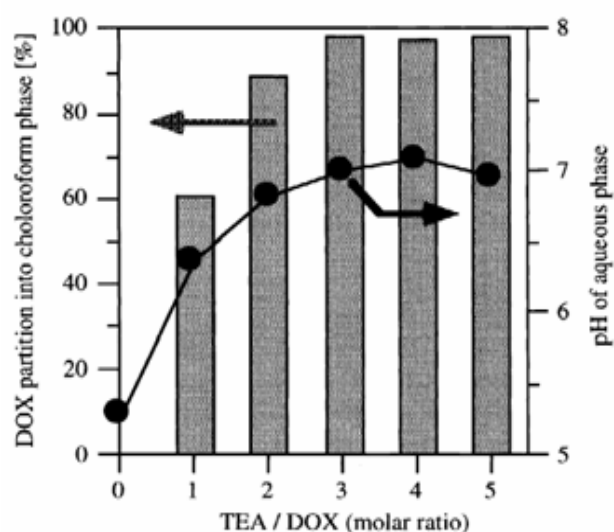
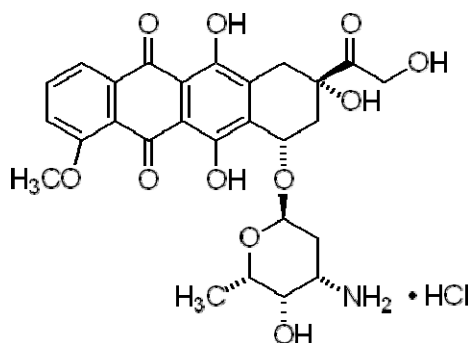


Figure 4.2 Effect of pH on the partition of Dox between chloroform and water [131]

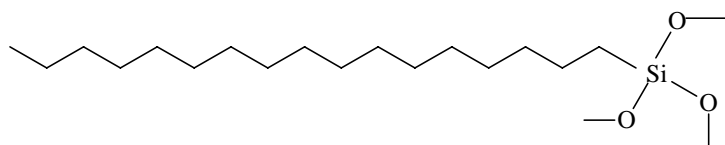
4.2 Materials and methods

4.2.1 Materials

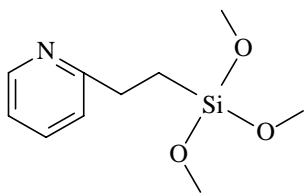
Doxorubicin (Dox) in the form of the hydrochloride salt was purchased from Sigma-Aldrich. Dox base was prepared by mixing Dox with three equivalent of triethylamine (TEA, Fisher Scientific) in dimethylsulfoxide (DMSO, Fisher Scientific). Chloroform was purchased from Fisher Scientific. Silane agents were obtained from Gelest, including n-octadecyltrimethoxysilane (95%, C18-silane), 2-(trimethoxysilylethyl)pyridine (95%, pyridine-silane) and tetraethoxysilane (99+%, TEOS).



Doxorubicin hydrochloride



n-octadecyltrimethoxysilane (C18-silane)



2-(trimethoxysilylethyl)pyridine (pyridine-silane)

Acetic acid (J.T. Baker, Philipsburg, NJ) and sodium acetate (ACS reagent) were obtained from Fisher Scientific. HEPES buffer solution (1M) was obtained from Invitrogen. Piranha solution was prepared by mixing concentrated sulfuric acid (H_2SO_4 , Fisher Scientific) and hydrogen peroxide (H_2O_2 , 30%, Fisher Scientific) with a volume ratio of 3:1. Deionized (DI) water was obtained by a Milli-Q A10 system and used for all the experiments. Magnetic nanotubes (silica nanotubes loaded with magnetic nanoparticles) with length of 2 μm were used for the study on Dox release at different pHs.

4.2.2 Modification of nanotubes

The inside surfaces of the nanotubes were modified with pyridine-silane to adjust the bonding strength of Dox molecules to the nanotubes by varying pH. The hydrophobic silane C18-silane was used together with pyridine-silane in order to increase the loading capacity and further adjust the release profile. The nanotubes were modified with pyridine-silane and C18-silane with three different ratios: 1) 100% C18-silane (100C18), 2) 75% C18-silane and 25% pyridine-silane (75C18), and 3) 50% C18-silane and 50% pyridine-silane (50C18). The final concentration of silanes was 5% prepared in 95% ethanol-water solutions. The silica coated

AAO templates were immersed in the pyridine-silane and C18-silane mixture for 20 min, washed with ethanol and water, and then baked in an oven at 120 °C.

4.2.3 Optical images

Cover slips were cleaned with Piranha solution and then modified with tetraethoxysilane (TEOS) to immobilize nanotubes. Specifically, the cover slips were immersed in 1:1:4 mixture of 1M HCl, TEOS and ethanol, sonicated for 5 min, and then rinsed with ethanol. 20 μ l of a nanotube solution is dropped on the TEOS coated cover slips and dry overnight at 25°C. To obtain the fluorescence images, the sample was located with a microscope in wide field mode, and then imaged with a color Charge-Coupled Device (CCD) camera.

4.2.4 Release profiles

The amount of the nanotubes was calculated based on the pore density of the template (10^{10} per cm^2) and the template area. The Dox base solution was prepared in 100 μ l DMSO solution with 3 equivalent of TEA at first, and then diluted with chloroform with the Dox concentration of 5 mg/ml. The solution was kept in the dark at 4 °C overnight to allow the neutralization of Dox. Nanotubes were then incubated in the solution overnight at 4°C to attain equilibrium. The nanotubes are then collected and dried at 60°C. To remove weakly bound drug molecules, the nanotubes were rinsed with 20 mM HEPES buffer (pH 7.2) solution, and then re-dispersed in 20 mM HEPES (pH 7.2) buffer solutions to study the release profiles at room temperature. The release profiles at acidic pH

were obtained in acetate buffer (pH 4.5). The concentration of Dox was measured by spectrofluorophotometer (RF-1501, Shimadzu) with an excitation wavelength of 490 nm and an emission wavelength of 560 nm.

4.3 Results and discussion

4.3.1 Optical images

Optical images of nanotubes loaded with Dox are shown in Figure 4.3. The loading was successful.

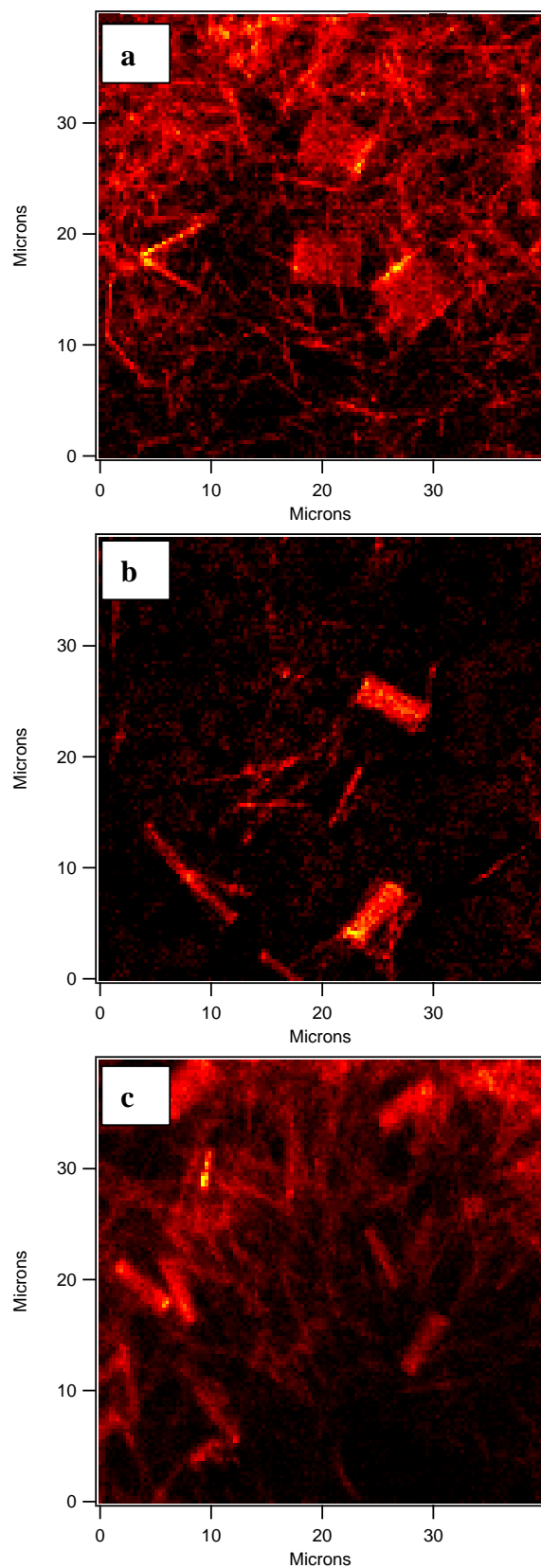


Figure 4.3 Optical images of SNTs loaded with Dox. (a) SNTs modified with 100% C18-silane, (b) SNTs modified with 75% C18-silane and 25% pyridine-silane, (c) SNTs modified with 50% C18-silane and 50% pyridine-silane.

4.3.2 Release profiles

To measure the concentration of Dox, calibration curves at pH 4.5 and 7.2 were obtained, as shown in Figures 4.4 and 4.5.

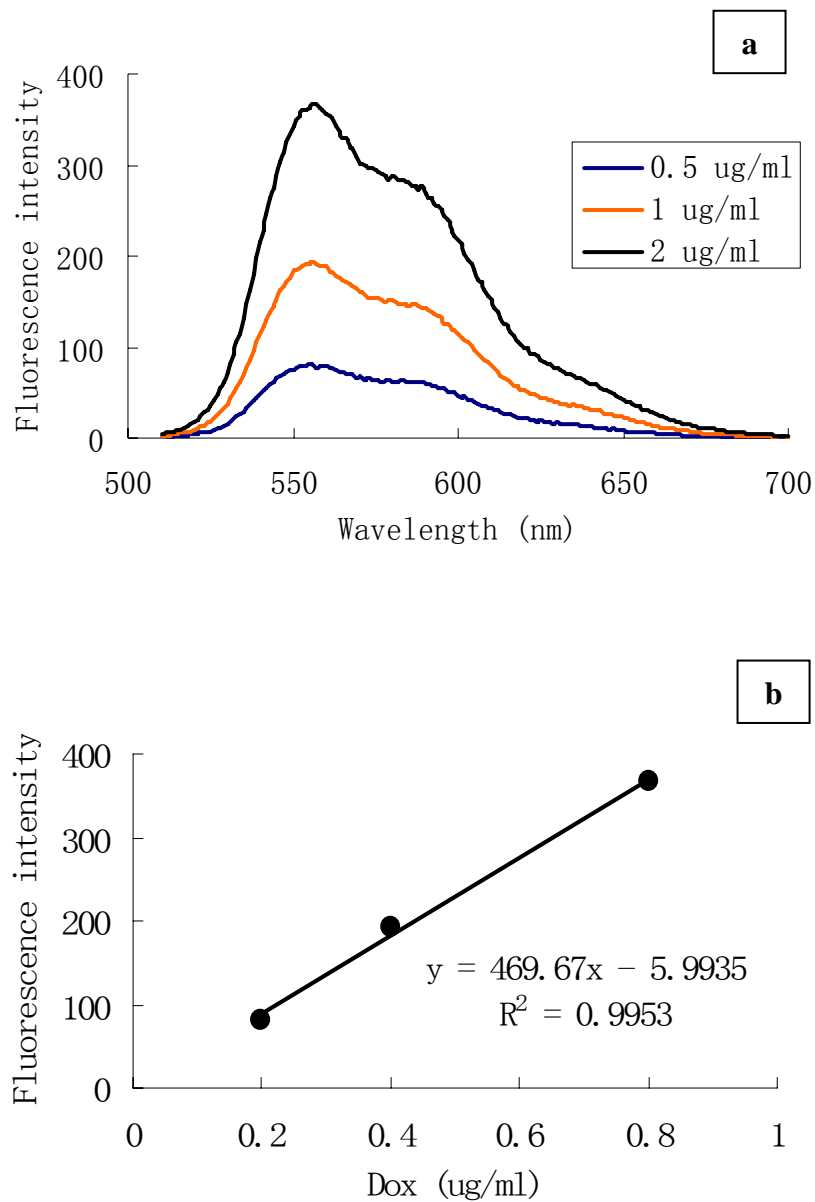


Figure 4.4 Fluorescence spectra for Dox and calibration curve in acetate buffer at pH 4.5

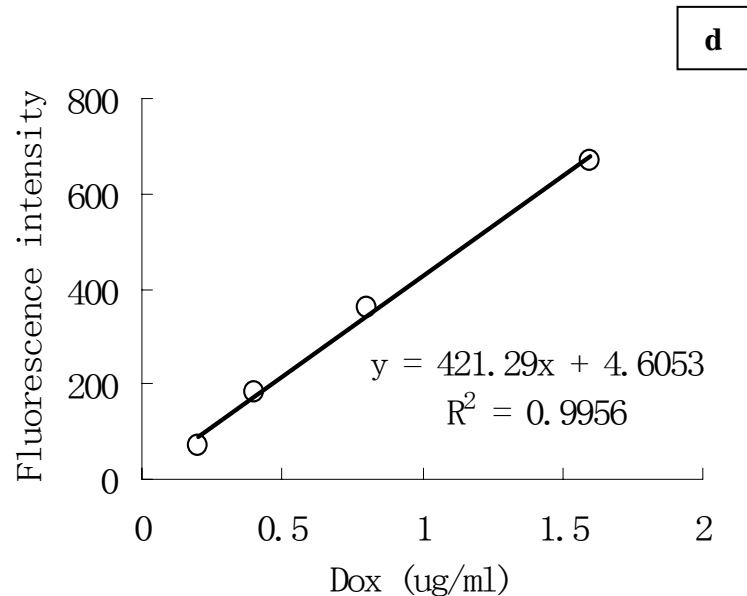
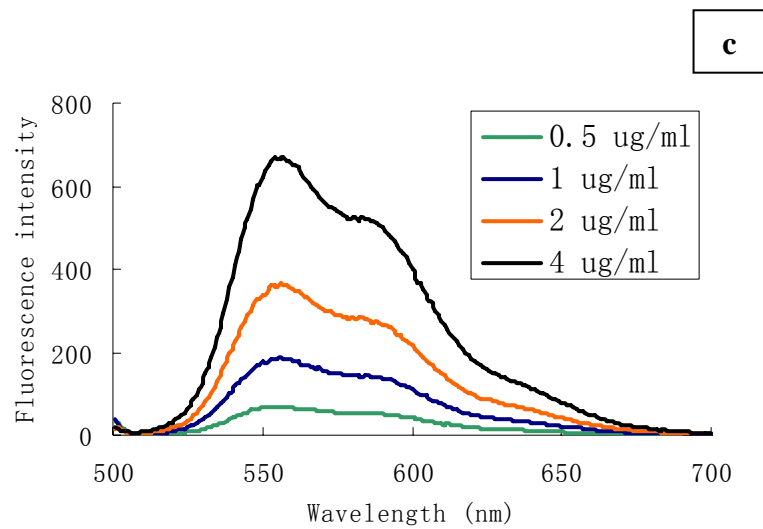


Figure 4.5 Fluorescence spectra for Dox and calibration curves in HEPES buffer at pH 7.2

The effect of pH on the release profile of Dox from the drug loaded nanotubes was studied, as illustrated in Figure 4.6. The fluorescence intensity was corrected to be the intensity per 10^{10} nanotubes by dividing the measured fluorescence intensity with the number of nanotubes. At pH 7.2, the fluorescence intensity of

Dox decreased with time. It can be explained by the intensity decay of the Dox molecular itself in the buffer solutions, as shown by the control sample. The control sample was prepared by diluting Dox base solution with HEPES (20 mM) buffer solutions.

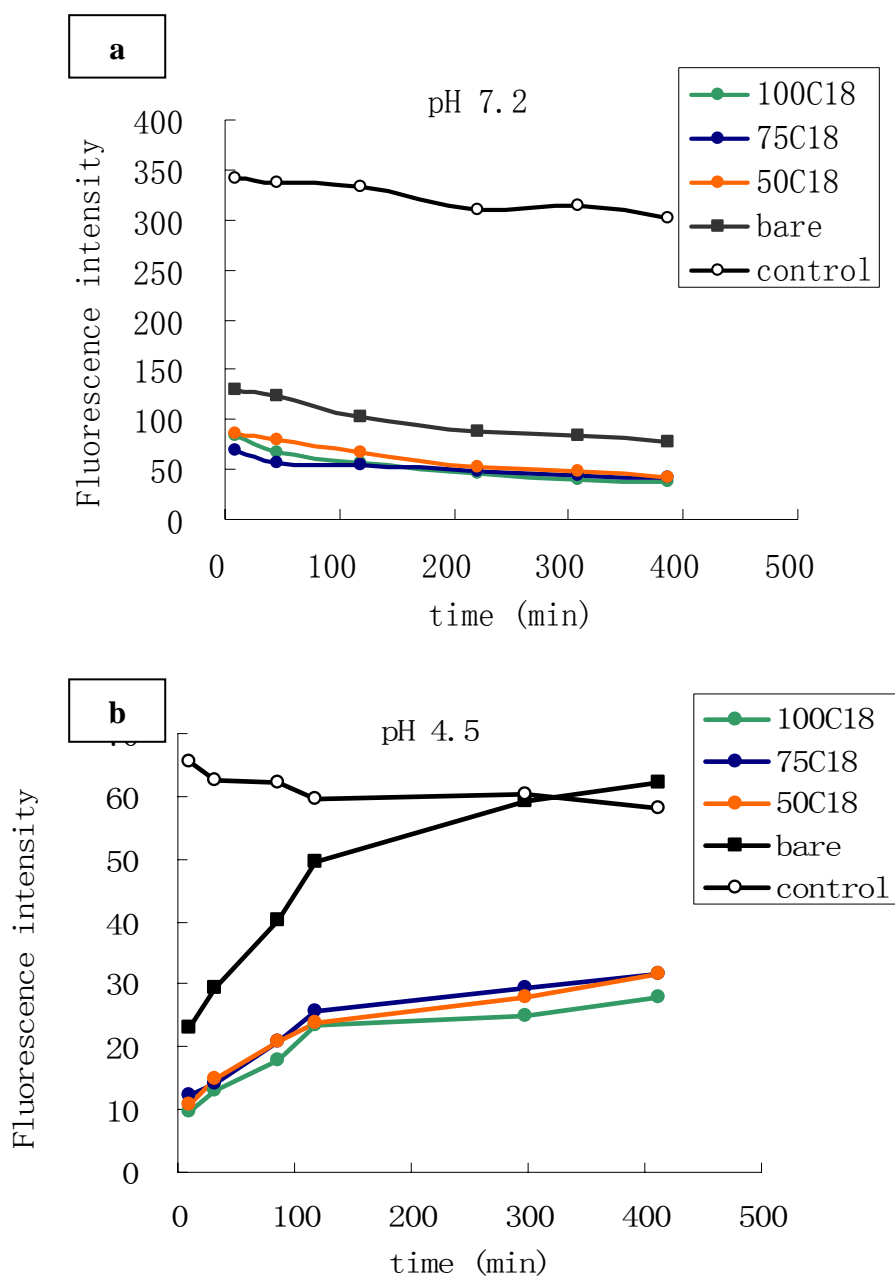


Figure 4.6 Effect of pH on the release profile of Dox from nanotubes

(a): pH 7.2, (b): pH 4.5

The amount of Dox loaded in the nanotubes (m_L) was calculated by multiplication of the concentration of the stock solution (5 mg/ml) and the total volume of the nanotubes. The payload mass of Dox was calculated to be 0.38 μg per 10^{10} nanotubes. The amount of Dox remained in the nanotubes after release in HEPES buffer ($m_{\text{remain}} = m_L - m_{\text{pH}7.2}$) were shown in Figure 4.7. There is no significant difference among the modified nanotubes and bare nanotubes based on the F-test. It indicates that physical trapping played the main role in loading Dox molecules in the nanotubes.

The release profiles of Dox in acetic buffer solutions were shown in Figure 4.8. The release percentage (%Release) is defined to be the released amount over the amount of Dox remained in the nanotubes after release in HEPES buffer solutions (m_{remain}). It is expressed as Equation 4.1.

$$\% \text{ Release} = \frac{m_{\text{pH}4.5}}{m_L - m_{\text{pH}7.2}} \cdot 100\% , \quad \text{Equation 4.1}$$

where $m_{\text{pH}4.5}$ is the amount of Dox released in acetate buffer solutions. This value is determined by the fluorescence intensity compared to the standard curve obtained in pH 4.5 buffer solutions. $M_{\text{pH}7.2}$ is the amount of Dox released in HEPES buffer solutions which is also determined by the fluorescence intensity. The amount of Dox is calculated to be the mass of Dox based on a number of 10^{10} nanotubes.

The release profiles at pH 4.5 showed that the modified nanotubes had a lower release rate than the bare nanotubes (Figure 4.9). This indicates that the modifications can control the release rate of Dox.

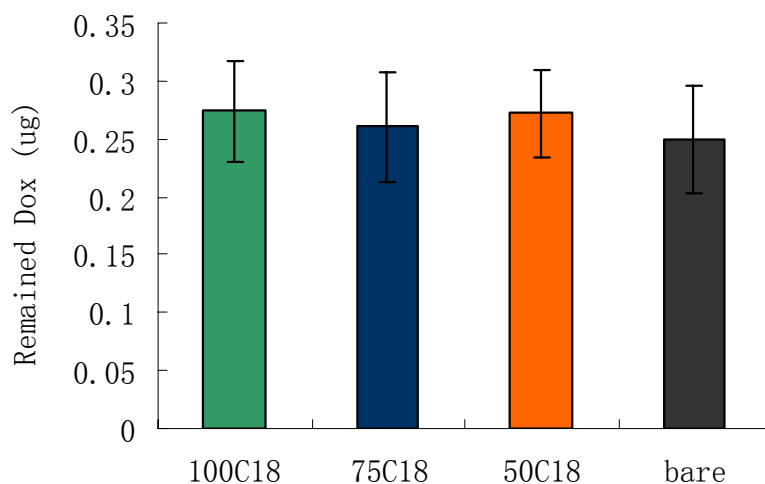


Figure 4.7 Dox remained in the nanotubes after release in HEPES buffer

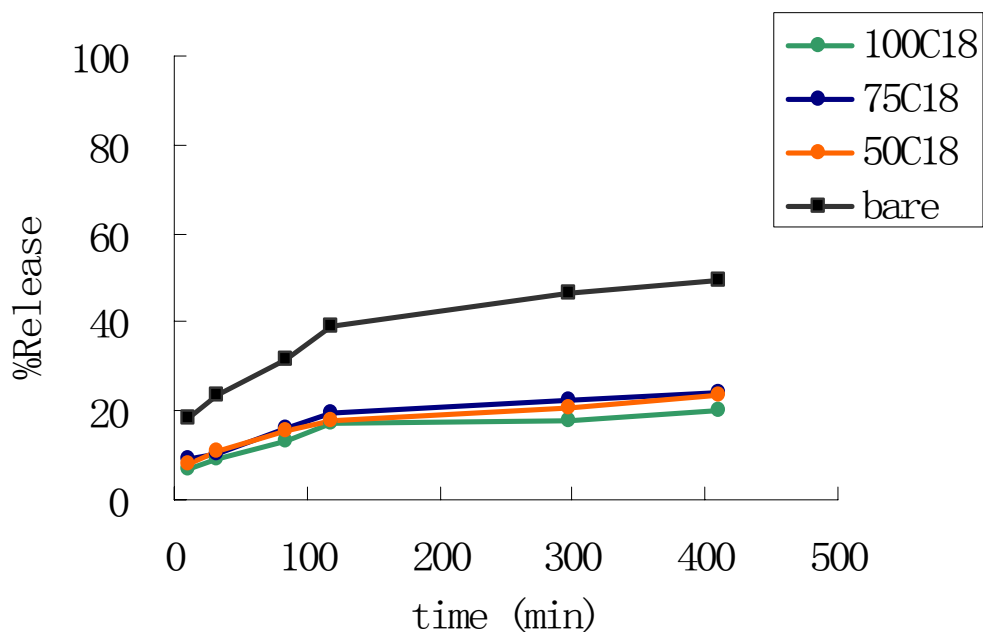
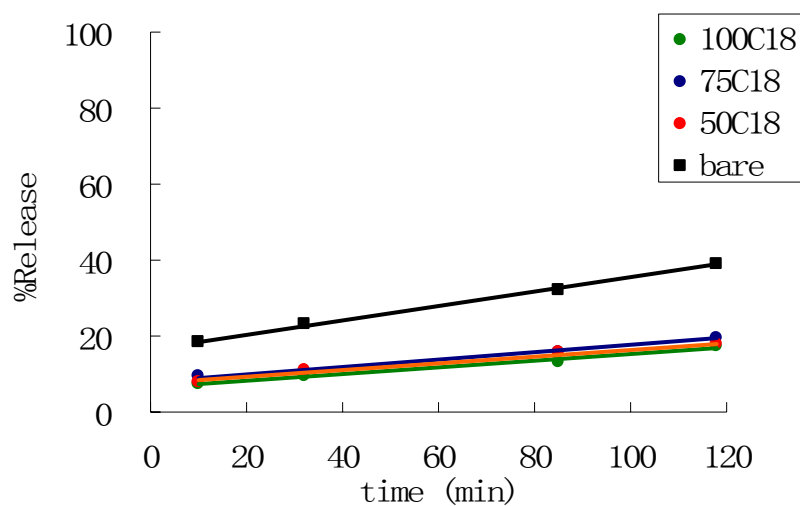


Figure 4.8 Dox release profiles at pH 4.5



Modification	100 C18	75 C18	50 C18	bare
Slope (min^{-1})	0.0880	0.0965	0.0874	0.1871

Figure 4.9 Releasing rates of Dox from MNTs

Considering the potential acidic pH effect on the stability of magnetic nanoparticles, TEM images of MNTs were taken before and after incubation in acetic buffer solution with pH of 4.5 for 55 h. As illustrated in Figure 4.10, MNTs were quite stable under these conditions.

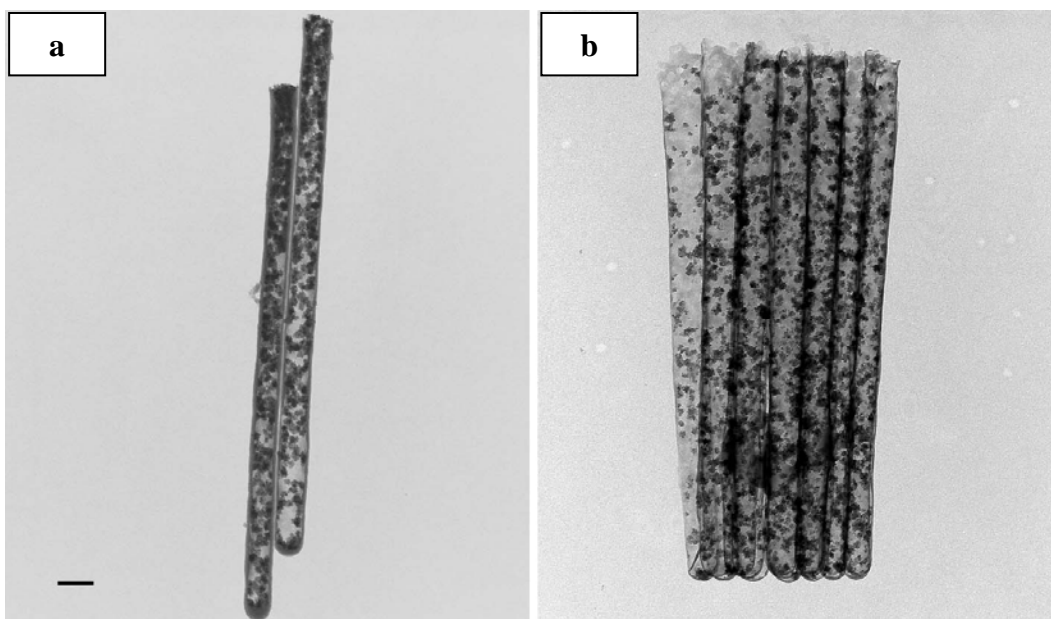


Figure 4.10 TEM images of magnetic nanotubes (MNTs) loaded with Dox before release (a) and after incubation in acetic buffer solution (pH 4.5) for 55 h

4.4 Conclusions

In summary, magnetic nanotubes can be used as drug reservoirs. The barrier effect of magnetic nanoparticles in nanotubes plays the main role in drug loading. Dox molecules were stable in the nanotubes at pH 7.2. They can be released at acidic pH. The modification of the inner surfaces of the nanotubes is effective in controlling the release rate.

Chapter 5: Cellular Uptake and Cytotoxicity

This chapter has been reproduced in part with permission from Nan, A; Bai, X; Son, SJ; Lee, SB; Ghandehari, H, Cellular uptake and cytotoxicity of silica nanotubes, *Nano Lett.*, 2008, 8 (8): 2150-2154.

5.1 Introduction

Multifunctional nanocarriers used to date such as liposomes, linear polymers, nanoparticles, and dendrimers suffer from inherent limitations such as instability or polydispersity, and often result in nonspecific accumulation and toxicity in normal organs [134]. Several studies have suggested that physicochemical properties of nanocarriers such as size, shape and surface functionalization influence their biodistribution (i.e. passing through endothelial and epithelial barriers), targetability (either passively by size control or actively by attaching targeting moieties to the surface of the carrier), and bioactive agent release (by control of pore size within the carrier)[52]. Development of advanced delivery systems in which size, functionalization and loading capacity is precisely tuned may allow a higher degree of control over their biological fate. Such control could potentially enhance therapeutic efficacy and reduce non-specific toxicity associated with conventional carriers.

Silica nanotubes (SNTs) prepared with the template synthesis method provide unique features such as monodispersity, distinctive inner and outer surfaces that can be differentially functionalized for loading biomolecules and targeting and biocompatibility, respectively. Magnetic nanotubes (MNTs), that is, silica nanotubes loaded with iron oxide nanoparticles, can be potentially used for

magnetically controlled bioseparation and biointeraction [44] and as MRI contrast agents [135]. Combining the attractive tubular structure with superparamagnetic properties, SNTs can be an ideal multifunctional platform for magnetic resonance imaging (MRI) monitored delivery. SNTs are mechanically robust with no swelling or porosity changes under physiological conditions [136].

Despite the unique advantages of SNTs in biomedical applications, exploration of their interactions with biological systems remains at a very early stage. Endocytosis has been demonstrated to be the main mechanism for cellular uptake of nanoparticles complexed with biological macromolecules, such as liposome-oligodeoxynucleotides and polymer-DNA. However, the mechanism of the cellular uptake of carbon nanotubes (CNT) is not conclusive. CNTs have been demonstrated as an effective carrier for gene and anti-cancer drug delivery [27, 70]. One of the key advantages of CNTs over other nanoparticles carriers has been considered to be the possibility of effectively crossing biological barriers [71]. Dennis Dishcer and colleagues have reported that filamentous polymeric micelles known as filomicelles (22 to 60 nm in diameter, and 2 to 8 μ m in length) have ten times longer blood circulation time than their spherical counterparts and have a high efficiency in delivering anticancer drugs [72]. However, the study of cellular uptake of gold nanoparticles (NPs) of different shapes showed a lower uptake of rod-shaped gold NPs in comparison to spherical shaped NPs and the rates of uptake were lower with an increasing aspect ratio [69].

To effectively develop these systems for applications, it is necessary to study the structural and functional properties that influence biocompatibility and mechanisms of cellular uptake and interactions. In this chapter, the cytotoxicity and cellular uptake of SNTs with two different sizes and surface charges in primary (non-malignant) and cancer cell models were described.

5.2 Experimental

The template and SNT dimensions were characterized by field emission scanning electron microscopy (SEM, Hitachi S-4700) and ZEISS EM10CA transmission electron microscopy (TEM).

5.2.1 Surface functionalizations

The inner or outer surface of silica nanotubes was modified using commercially available silane reagents (Gelest, Morrisville, PA). For uptake studies nanotubes were modified in the inner surface to permit attachment of a fluorescent probe Alexa Fluor488 (Invitrogen, Eugene, Oregon). For this purpose nanotubes embedded in the alumina template were first modified with 3-trimethoxysilylpropyl diethylenetriamine (95%, DETA). DETA was used as a linker to covalently bind Alexa Fluor to the inner surface of nanotubes. After dissolution of the template, liberated nanotubes were immersed in 1% Alexa Fluor 488 TFP with 0.1 M sodium carbonate buffer solution for labeling. Stopping reagent hydroxylamine (1.5 M NH_2OH in 0.1M sodium carbonate buffer, Fisher

Scientific) was used to remove non-bound or weakly bound dye molecules. Nanotubes were washed and collected by filtration.

Without any outer surface modification nanotubes are negatively charged under physiological conditions. To prepare positively charged outer surfaces, the nanotubes were treated with 5% aminopropyltrimethoxysilane (95%, APTS) in 95% ethanol/water solution for 10 min and then cured at 120°C for 20 min.

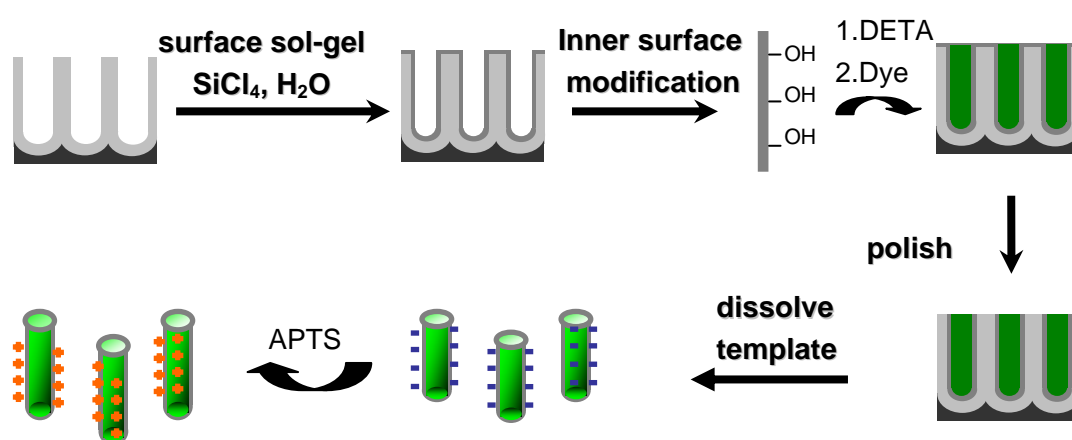


Figure 5.1 Schematic representation of template synthesis of silica nanotubes

5.2.2 Growth inhibition assay of silica nanotubes

Cytotoxicity of the SNTs was assessed on an epithelial breast cancer cell line, MDA-MB-231, and a Human Umbilical Vein Endothelial Cell (HUVEC) line by the standard MTT (3-(4,5-Dimethylthiazol-2-yl)-2,5-diphenyltetrazolium bromide, a tetrazole) assay. Briefly, cells were plated in 96 well plates (Corning, Inc., Corning, NY) at a density of 1000 cells/well. After 24h plates were incubated with SNTs of varying concentration at 37 °C for 3 days followed by addition of 100 μl

of MTT solution for 1 h. Upon removal of the MTT solution, the purple formazan crystals produced were solubilized with 100 μ l of DMSO and measured at 560 nm on a microplate reader (SPECTRAmax plus, Molecular Devices, Sunnyvale, CA). Toxicity was expressed as % of viable cells. Statistical significance of differences in toxicity between different samples was analyzed using a two-tailed unpaired student t-test.

5.2.3 Confocal microscopy

The localization of fluorescently labeled SNTs (labeled with Alexa Fluor 488) in the cellular and intracellular spaces was visualized via confocal laser scanning microscopy (CLSM). Images were obtained using a Nikon Eclipse TE2000 inverted confocal microscope (Nikon Instruments, Inc., Melville, NY). Cells were seeded at a density of 30,000 cells/cm² onto collagen-coated 4-chamber culture slides (BD Biosciences, Bedford, MA) and maintained under normal incubation conditions for 24h. The growth medium was replaced with PBS, and cells were equilibrated for 30 min before uptake experiments. Cells were treated with 300 μ l of 0.01 μ g/ml SNTs for 30 min. The nanotubes were removed by washing the cells 3 times with PBS. For colocalization studies, cells were subsequently chased with 300 μ l pre-warmed (37°C) solution of various markers (Clathrin, LysoTracker Red) at 37°C for additional 30 min to allow internalization. The cells were then fixed with 300 μ l of 4% paraformaldehyde for 20 min at room temperature. Nuclei of cells were stained with 300 μ l of DAPI and incubated at room temperature for 10 min. The cells were washed with PBS, and the chambers were

removed. Gel/Mount was added to each region and slides were covered with a glass coverslip, sealed, and dried overnight at 4°C. Images were obtained using a Nikon Eclipse TE2000 inverted confocal laser scanning microscope (Nikon Instruments, Inc., Melville, NY), equipped with an argon ion laser. DAPI was visualized with excitation and emission wavelengths of 405 nm and 450 nm, respectively; Alexa Fluor 488 was visualized with excitation and emission wavelengths of 488 nm and 515 nm, respectively. The 3-D confocal images were acquired using the following parameters of the Nikon EZ-C1 acquisition software (version 2.3, Image systems, Inc., Columbia, MD): 60x oil objective with numerical aperture = 1.4; 100 µm pinhole size; 9.64 µs scan dwell; 512 x 512 pixel size; 0.5 µm z-step size. All images were recorded using an Image Quant Z-stack which produced a three dimensional image of the samples.

To investigate endocytic uptake, nanotubes were incubated at 37 °C in the presence of 0.1% sodium azide [137] and hyperosmotic 0.45M sucrose [138] for 10 min followed by treatment with SNTs.

5.2.4 Transmission electron microscopy

Following 30 min incubation with SNTs, the cells were fixed with 2.0% glutaraldehyde buffered in 0.1 M PBS for 1 hour at room temperature. After washing with 0.1 M PBS, the cells were collected in centrifuge tubes, and then post-fixed in 1% osmium tetroxide and 2% uranyl acetate. The samples were dehydrated through a series of alcohol concentrations (35%, 50%, 75%, 95% and 100% ethanol). The cells were then treated with propylene oxide and embedded in

Spurr's resin by infiltration with a series of mixtures of resin and propylene oxide at ratios of propylene oxide to resin: 1:1, 1:2, 1:3 respectively. The sample was subsequently incubated at 70°C overnight. Ultra-thin sections with thickness about 60 nm were obtained with ultrathin microtome (Reichert Ultracut, Vienna, Austria) and stained with 2.5% uranyl acetate and 2.5% lead citrate for transmission electron microscopy contrast enhancement. Cell and nanoparticle images were taken with ZEISS EM10CA TEM microscope (Thornwood, NY) operating at 80 kV. All the chemicals for the preparation of TEM cell samples were obtained from Electron Microscope Science.

5.2.5 Cell labeling with MNT-Pro complexes and assessment of toxicity

Protamine sulfate (Pro) was used as a transfection agent [139]. Considering the potential interaction between Pro and serum, MNT-Pro was prepared in serum-free RPMI 1640 media (Biosource, Camarillo, CA) with MNTs of 10 µg/ml and Pro of 40 µg/ml. The zeta potentials of 500 nm-MNTs and MNT-Pro complexes in PBS were measured with a Zeta Potential analyzer (Brookhaven Instrument, New York). A total of 10 runs were collected, and results are reported as mean and standard deviation. Rat glioma C-6 cells (ATCC Manassas, VA) were incubated in a 96-well plate. The media in the wells were then replaced with 500 µl of serum-free media with MNT-Pro complexes. 500 µl of complete media was added in the well after 2 hrs. The cells were then incubated at 37 °C with 5% CO₂, 95% air for 24 hrs. The Prussian blue method was used to evaluate the labeling efficiency. This method involves the reaction of the ferric ion present in the cells

with the ferrocyanide and results in the formation of a bright blue pigment called Prussian blue, or ferric ferrocyanide [140]. The cells were washed three times with phosphoric buffer saline to remove unlabeled MNT-Pro complexes, trypsinized and transferred to cytospin slides. After drying overnight, the slides were incubated for 20 minutes in a mixture of 50 ml of 20% potassium ferrocyanide and 50 ml of 20% hydrochloric acid, washed, and then counterstained with nuclear fast red. This protocol has been published previously [93].

For the assessment of the MNT-Pro complexes toxicity, rat glioma C-6 cells grown in RPMI 1640 media were used. The glioma C-6 cells labeled with MNT-Pro were evaluated with MTS (3-(4,5-dimethylthiazol-2-yl) -5-(3-carboxymethoxyphenyl) -2- (4-sulfophenyl)-2H-tetrazolium) assay after one day incubation at 37°C with 5% CO₂, 95% air. The absorbance of the formazan product was then measured at a wavelength of 570 nm, with 750 nm as the subtracted reference wavelength. The results of the MTS assays were expressed as the percentage of the corresponding control cells.

5.3 Results and discussions

Using the “template synthesis” strategy (Figure 5.1) combined with surface sol-gel chemistry, a series of 50 nm diameter SNTs was fabricated namely: 1) 200 and 500 nm long, bare (non-functionalized) SNTs and 2) 200 and 500 nm long, SNTs functionalized with positively charged aminosilane group on the outer surface. The TEM images demonstrate discrete monodisperse dimensions (diameter and length) of the template (Figure 5.2a, b) and the fabricated nanotubes (Figure 5.2c,

d). The dimensions of the nanotubes can be controlled by the pore diameter and thickness of the template [38, 81].

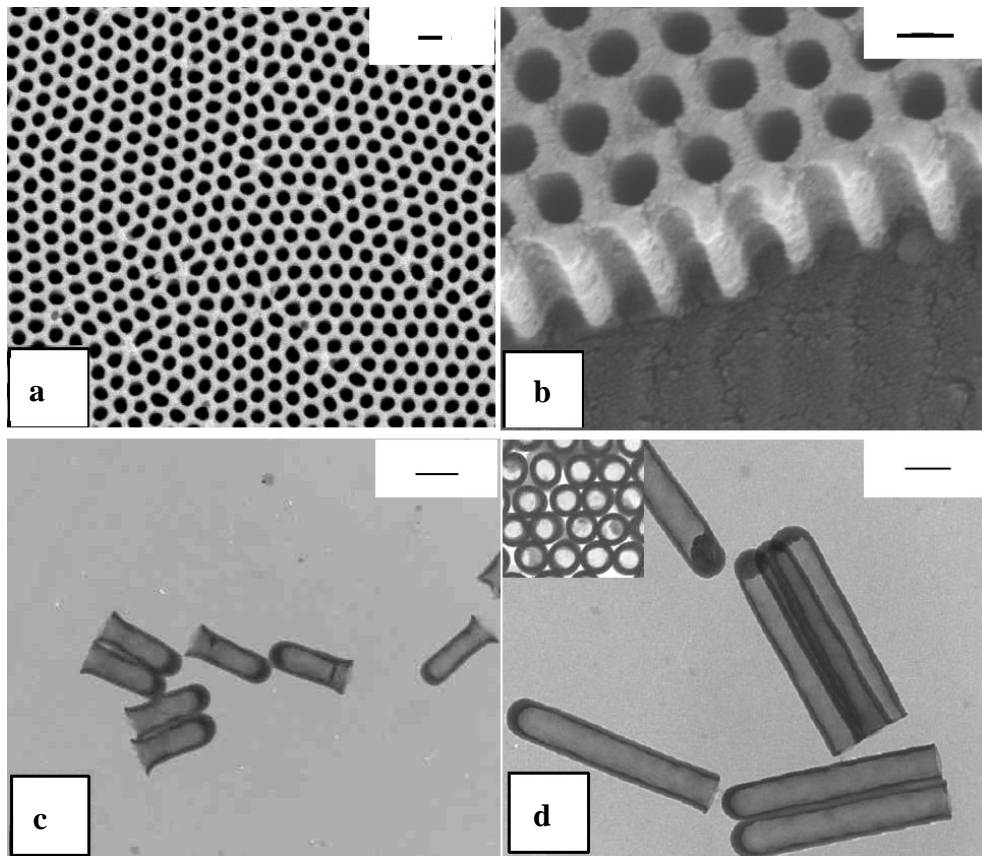
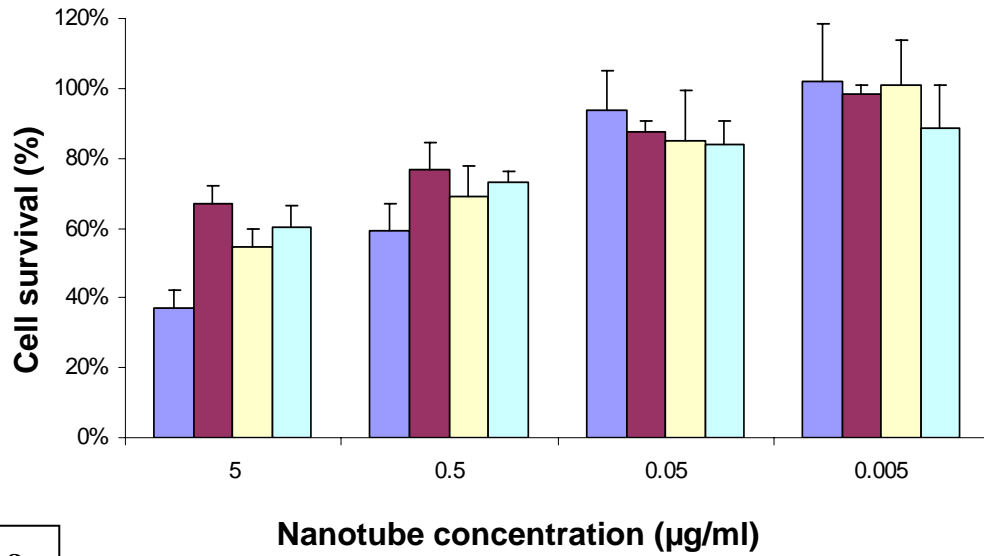


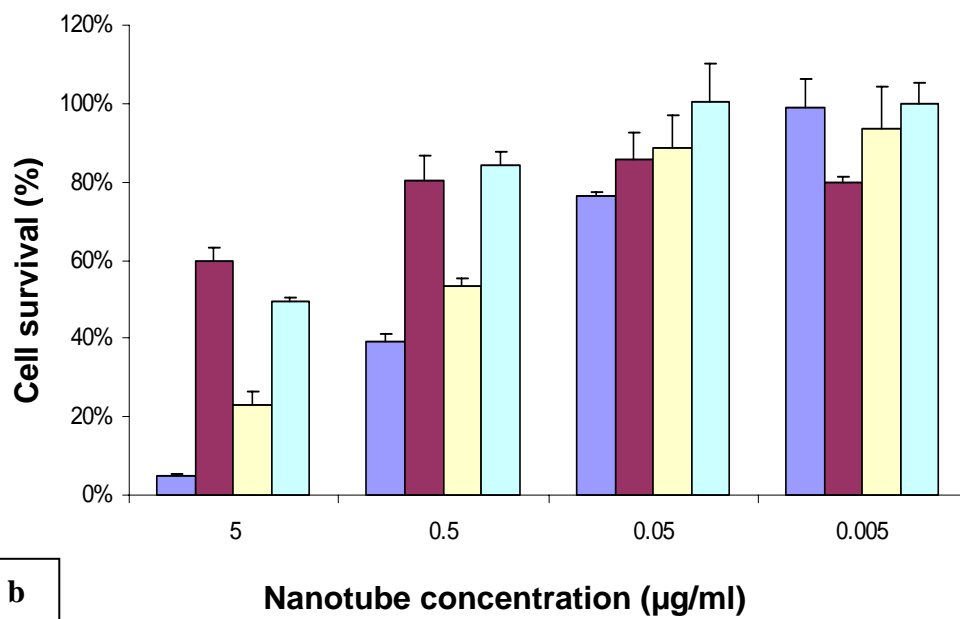
Figure 5.2 Scanning electron microscope images of porous alumina template for SNT (diameter: 50 nm, length: 200 nm) (a) Top view, (b) Cross section, and Transmission Electron Microscope images of bare silica nanotubes (50 nm dia.) Length: (c) 200 nm, (d) 500 nm, with inset of TEM image for the cross section of the SNTs bundle.

The effect of varying size and surface functionalization of SNTs on cytotoxicity was evaluated against two different human cell models: an epithelial breast cancer cell line (MDA-MB-231) and a primary umbilical vein endothelial cell line (HUVEC). The two cell lines were chosen as representative models of the various

cellular environments that SNTs are likely to interact with *in vivo*. Results are reported as mean \pm SEM (n=3). Statistically significant differences are indicated relative to 200 nm positively charged SNTs (*: $p < 0.002$; **: $p < 0.02$). In both the cell lines the SNTs exhibited growth inhibition in a concentration dependent manner. At lower concentrations (0.05 and 0.005 $\mu\text{g/ml}$) the nanotubes did not inhibit the growth of either of the above cell lines. At higher concentrations (5.0 and 0.5 $\mu\text{g/ml}$) both the 200 nm and 500 nm SNTs caused up to 63% growth inhibition of breast cancer cells. At 5 $\mu\text{g/ml}$ concentration, 200 nm positively charged SNTs were significantly more toxic ($p < 0.002$) than the corresponding bare nanotubes (Figure 5.3a). This higher toxicity suggests the possibility of increased cellular association and/or uptake of the nanotubes due to non-specific interactions with the negatively charged cell surface. These observations are also in agreement with reports in the literature on other nanosized carrier molecules such as cationic polymers, amino or polylysine functionalized silica nanoparticles [141, 142], cationic dendrimers or several other positively charged nanostructures whose inherent cytotoxicity, and cellular uptake, is shown to be primarily associated with cationic charge present on the surface.



a



b

Figure 5.3 MTT cytotoxicity assay showing the effect of varying concentrations of nanotubes on growth inhibition of (a) MDA-MB-231 breast cancer cells and (b) Human Umbilical Vein Endothelial Cells (HUVEC) cultured in vitro.

Legends: ■ 200 nm with positively charged APTS outer surface group; ■ 200 nm with no outer surface functionalization; ■ 500 nm with positively charged APTS outer surface group ■ 500 nm with no outer surface functionalization.

The nanotubes showed a similar trend for concentration dependent cytotoxic effects against the primary HUVEC cells (Figure 5.3b). However compared to breast cancer cells at high concentrations (5.0 and 0.5 $\mu\text{g/ml}$) the effect of size and charge seemed to be more significant. Positively charged nanotubes were significantly more toxic than bare nanotubes even at ten fold lower concentration (0.5 $\mu\text{g/ml}$) in HUVECs than in breast cancer cells. These results indicate that in addition to concentration and surface charge, cytotoxicity of SNTs is cell-type dependent. Reports in the literature on similar studies with silica nanoparticles suggest[143] that cancer cells are more resistant to nanoparticle mediated toxicity than normal non-malignant primary cells of the body. Some research groups attribute such resistance to the fact that normal primary cells of the body are more susceptible to nanoparticle mediated cellular membrane injury leading to more rapid onset of apoptotic or necrotic cell death[143-146]. Others more informatively relate cytotoxicity data of different cell lines to their metabolic activity or their rate of proliferation[143, 147]. The cell population doubling times of normal human endothelial cells were about 30 h compared to 20 h doubling time of the MDA-MB-231 breast cancer cells. However further mechanistic toxicity studies are needed to confirm these observations in the context of the SNTs.

At higher concentrations (5.0 and 0.5 $\mu\text{g/ml}$) positively charged SNTs of smaller length (200 nm) were significantly more toxic to the HUVECs than their longer (500 nm) counterparts. This was also observed at 5 $\mu\text{g/ml}$ concentration for breast

cancer cells. The results indicate that in addition to charge, size of nanotubes may also determine the extent of interaction with cells and toxicity. Reports in the literature[148-150] generally suggest that smaller sized particles allow increased cellular interactions and therefore may possess enhanced intrinsic toxicity. The cellular uptake can be considered as a result of competition between thermodynamic driving force for wrapping and the receptor diffusion kinetics[69]. Further, when comparing equivalent concentrations, the number of 200 nm SNTs is about 2.5 times of that of 500 nm given that they have the same mass. Therefore, smaller particle size along with increased number of particles may be responsible for the increased toxicity observed with the 200 nm length SNTs. Given the control over nanotube dimensions and functionalization using the template synthetic strategy one can conceive the ability to predict the influence of discrete size and charge on cytotoxicity and uptake.

Although growth inhibitory effects were observed for both bare and positively charged SNTs these effects were primarily seen at very high concentrations. At 0.05 $\mu\text{g/ml}$ concentration ($\sim 10^8$ SNTs/ml) and lower all SNTs irrespective of their surface characteristics were non-toxic. This indicates the suitability of these nanotubes for drug delivery applications. Additionally appropriate surface modification of SNTs such as with biocompatible polymers could potentially enhance their safety profile but such studies need to be performed.

The internalization of SNTs was further evaluated by Transmission Electron Microscopy (TEM). As shown in Figure 5.4, intact nanotubes are primarily seen

vertically embedded (in the cross sectional view, marked by blue arrows) as confirmed by measurement of their diameters. Few intact nanotubes are seen in a horizontal alignment (lengthwise view Figure 5.4a marked with a red arrow). These results provide visual evidence for the first time of cellular uptake of SNTs.

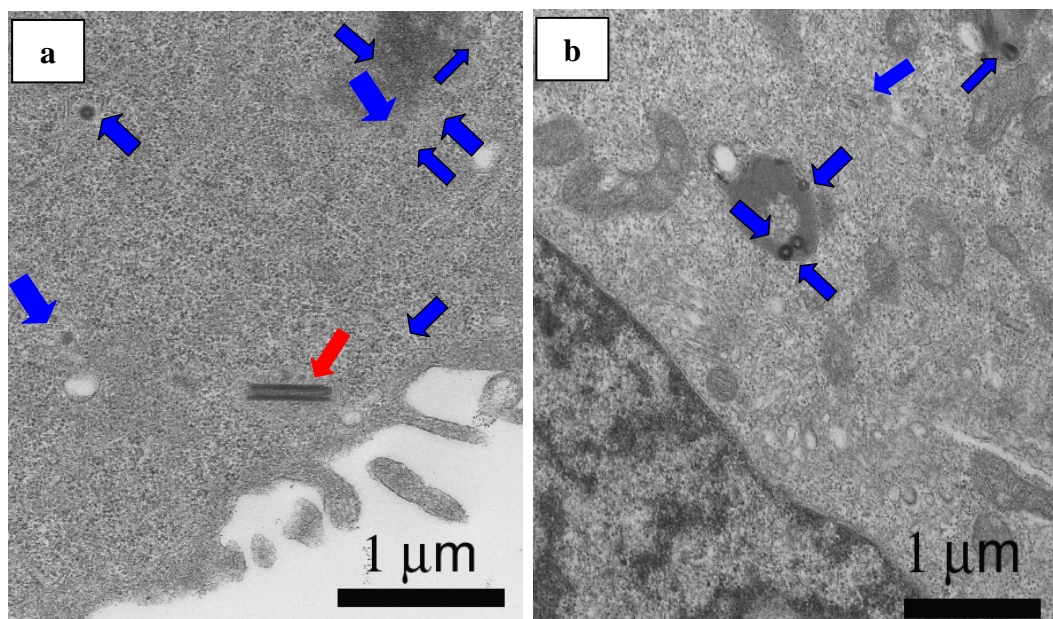


Figure 5.4 Transmission Electron Microscope images showing uptake of 500 nm positively charged SNTs in MDA-MB-231 cells. Blue arrows indicate cross sectional view and red arrows horizontal view of nanotubes.

Finally, the possible mechanisms of cellular uptake of SNTs were evaluated. Reports in the literature suggest that the uptake of nanoparticulate systems into cells typically can occur through several different processes such as non-specific diffusion, phagocytosis and receptor mediated or fluid phase endocytosis [151]. As an initial attempt toward systematically delineating the mechanisms of uptake we investigated the involvement of fluid phase endocytosis. Confocal microscopy techniques were used in the absence and presence of known metabolic (ATP)

inhibitors. Results demonstrated cellular uptake of fluorescently labeled SNTs (200nm) (Figure 5.5a). Internalization of SNTs was significantly inhibited in presence of sodium azide (Figure 5.5b) and sucrose (Figure 5.5c) suggesting the involvement of fluid phase endocytosis.

Endocytic uptake of the SNTs was further evaluated by colocalization with Clathrin (a marker of clathrin mediated early endosomal pathway) and LysoTracker (a marker for lysosomal uptake). Positively charged SNTs (labeled green) demonstrated a higher degree of association with the cell membrane as observed for both Clathrin (labeled red) and LysoTracker (labeled red) coincubation studies (Figure 5.6 b and d) than the respective studies with bare SNTs (Figure 5.6 a and c). This could be attributed to non-specific charge interaction of cationic SNTs with the negatively charged cell surface. SNTs colocalized (labeled orange) to a larger extent with the LysoTracker than with Clathrin suggesting that by 30 min most of the internalized nanotubes accumulate in the lysosomal compartment. Together these results qualitatively indicate that positively charged SNTs interact with cells and accumulate intracellularly to a greater extent than unmodified bare SNTs. Such increased interaction and uptake of positively charged SNTs could therefore be attributed to the increased toxicity observed in growth inhibition studies at higher concentrations.

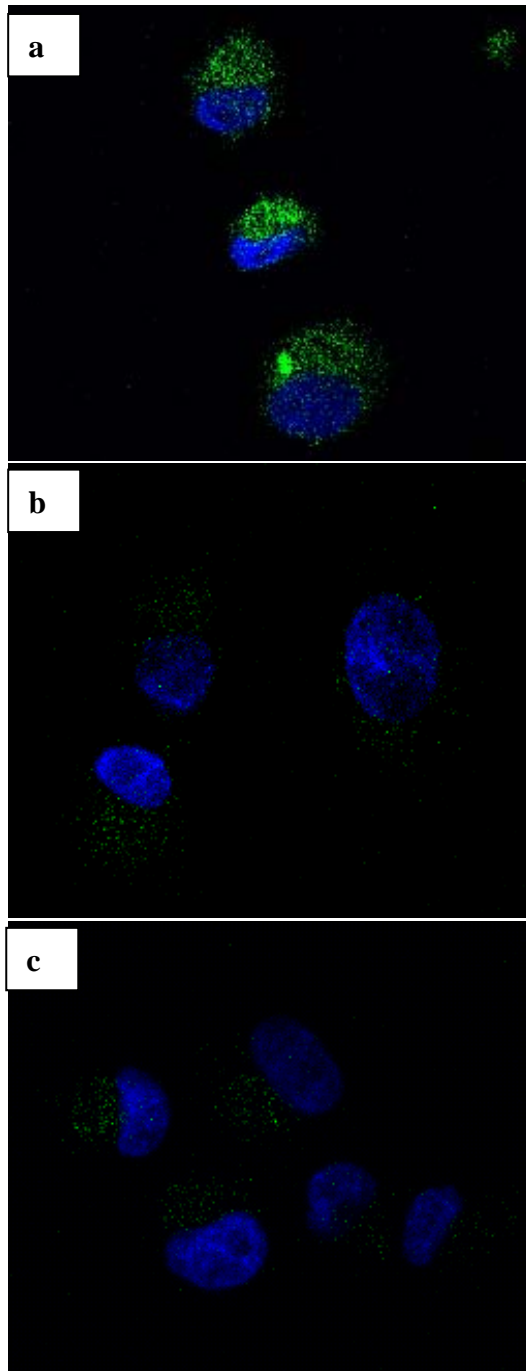


Figure 5.5 Confocal microscope images of uptake of 200 nm positively charged fluorescent SNTs by MDA-MB231 cells at 37°C. (a) without metabolic inhibitors, and in the presence of metabolic inhibitors of endocytosis namely (b) sodium azide and (c) sucrose. Concentration of SNTs is 0.01 $\mu\text{g/ml}$.

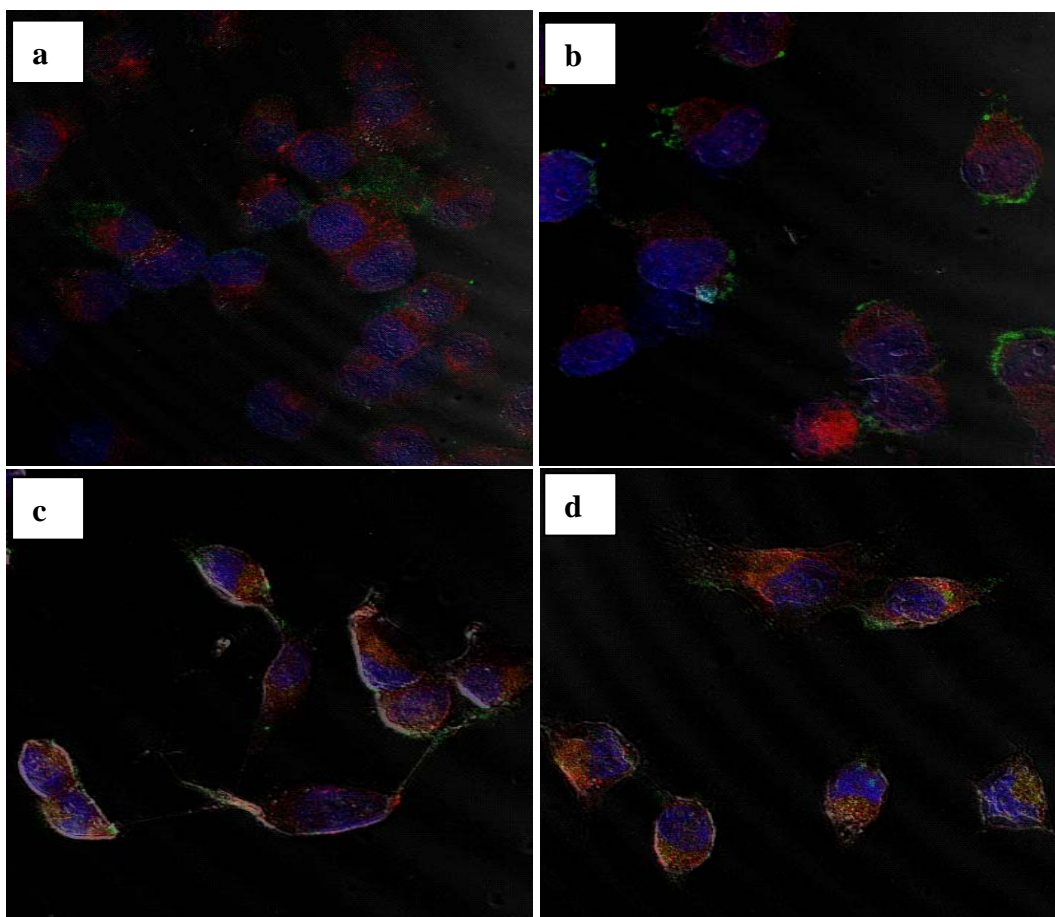


Figure 5.6 Confocal microscope images of uptake of fluorescent SNTs by MDA-MB231 cells. Colocalization studies with 200 nm SNTs with negatively (a and c) and positively charged (b and d) outer surfaces.

(a) and (b) show colocalization of SNTs (green) with an early endosomal marker (Clathrin, red). (c) and (d) show colocalization with a lysosomal marker (Lysotracker, red). Nuclei of cell stained with DAPI (blue). Concentration of SNTs is 0.01 $\mu\text{g/ml}$.

No significant toxicity was shown for the 500 nm-MNT labeled rat glioma cells with the MNT concentration up to 20 $\mu\text{g/ml}$ for 24 hrs after labeling (Figure 5.7). The zeta potential for the MNT-Pro complexes for cell labeling is 12.39 ± 0.02 mV while the zeta potential for bare MNTs is -25.68 ± 0.02 mV. The change in zeta potential of MNT following the addition of protamine sulfate would indicate that complexes form through van der Waals or electrostatic interactions. Cells were considered Prussian blue positive when intracytoplasmic blue granules were detected. The histology images show that more than 80% of the cells were labeled with 500 nm-MNTs successfully (Figure 5.8). However, the cells were not labeled heavily. Further studies are needed to optimize the labeling conditions to increase cellular uptake, such as tailoring the dimension of MNTs and preparing MNT-Pro with different zeta potential.

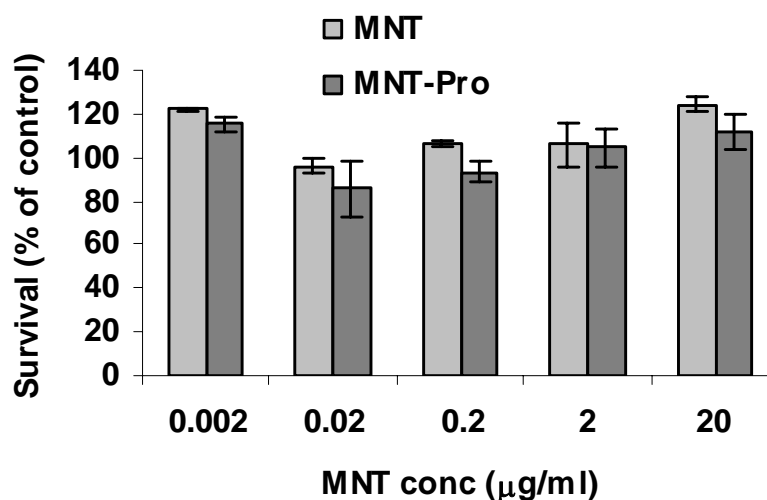


Figure 5.7 MTS cytotoxicity assay results for 500 nm-MNT labeled rat glioma cells for 24 hours

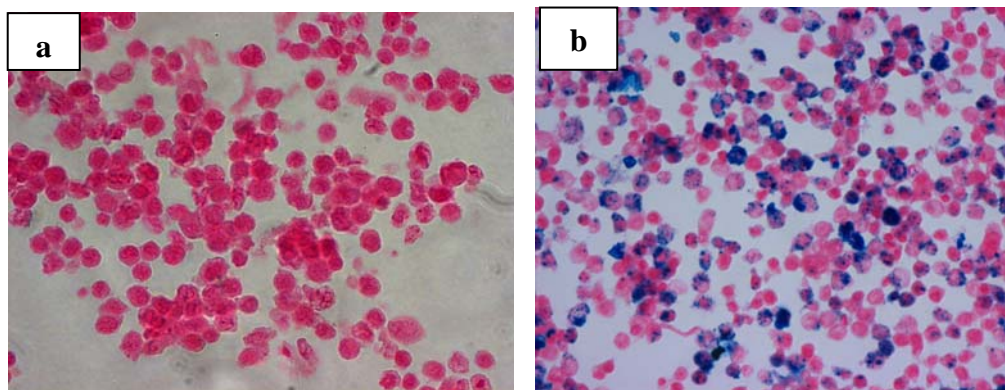


Figure 5.8 Representative Prussian blue-stained (a) unlabeled cells and (b) MNT-Pro labeled cells.

5.4 Conclusions

In summary, SNTs of discrete length, diameter and surface charge were fabricated. The nanotubes showed limited toxicity which was concentration- surface charge- and length- dependent and were internalized in cells at least in part by endocytosis. These initial studies pave the way for understanding the structural features of silica nanotubes influencing their behavior in cellular and tissue environments. In the long term these understandings can aid in designing silica nanotubes with specific biomedical applications including drug delivery. The preliminary studies on the *in vitro* cell labeling with MNTs reveal that the MNTs are not toxic, and the labeling is effective. These results indicate that this unique nanostructure might have potential in monitoring transplantation for cell-based therapy.

Chapter 6: Segmented Modification of Nanotubes

6.1 Introduction

The increasing interest in medical applications of nanotechnology has heightened the need for synthesizing nanoparticles with well-defined dimensions and multifunctionalities. Template synthesis has become an important approach applied to nanomaterials synthesis [152-156]. It allows for the reproduction of the nano-structure with the best possible reproducibility. Anodic aluminum oxide films are popular due to their easy fabrication and control of pore dimensions by applying appropriate electrochemical parameters and chemical pore widening conditions[90, 157-160].

6.1.1 Differential modifications

With the template synthesis method, nanotubes with one open end are of particular interest for drug/gene delivery applications[48, 83, 161, 162]. Hollow tubular structures obtained can be differentially functionalized between the inner and outer surfaces, which provides a platform for multifunctionality through sequential surface modifications. Furthermore, the open ends of pores can serve as gates to control the release of drugs/genes while the inner voids can be loaded with a large amount of drugs [44, 49, 84]. Researchers have been exploring strategies for controlled payload-release. The idea is to design a universal delivery vehicle, capable of carrying a large payload, and has a cap which can be released in the environment where the drug molecules are to be delivered.

It has been reported that controlled release of drugs from the tubular structure can be realized by capping the open ends of the tubular nanostructures with nanoparticles via chemically labile bonds[163-167]. Figure 6.1 shows schematically a controlled release mechanism. The system is based on the chemical reduction of a disulfide linkage between a CdS nanosphere cap and a mesoporous silica nanoparticle host. The drug release profile demonstrates that this strategy works under the experimental conditions[168]. However, there is a drawback for this system. The modification of the inner voids for pore caps can limit the types of drugs and/or the loading capacity. It is challenging to realize a drug-friendly inner void and chemically labile bonds for capping on the same nanotubular structure.

Segmented modifications, that is, modifications of the entrance and the remainder of the tubular structure differently, can provide a way to solve this problem. The surfaces at the entrance of the nanotube can be used to link and release the cap while the chemistry for the rest inner surfaces of the nanotube can be drug-friendly and used as a drug reservoir.

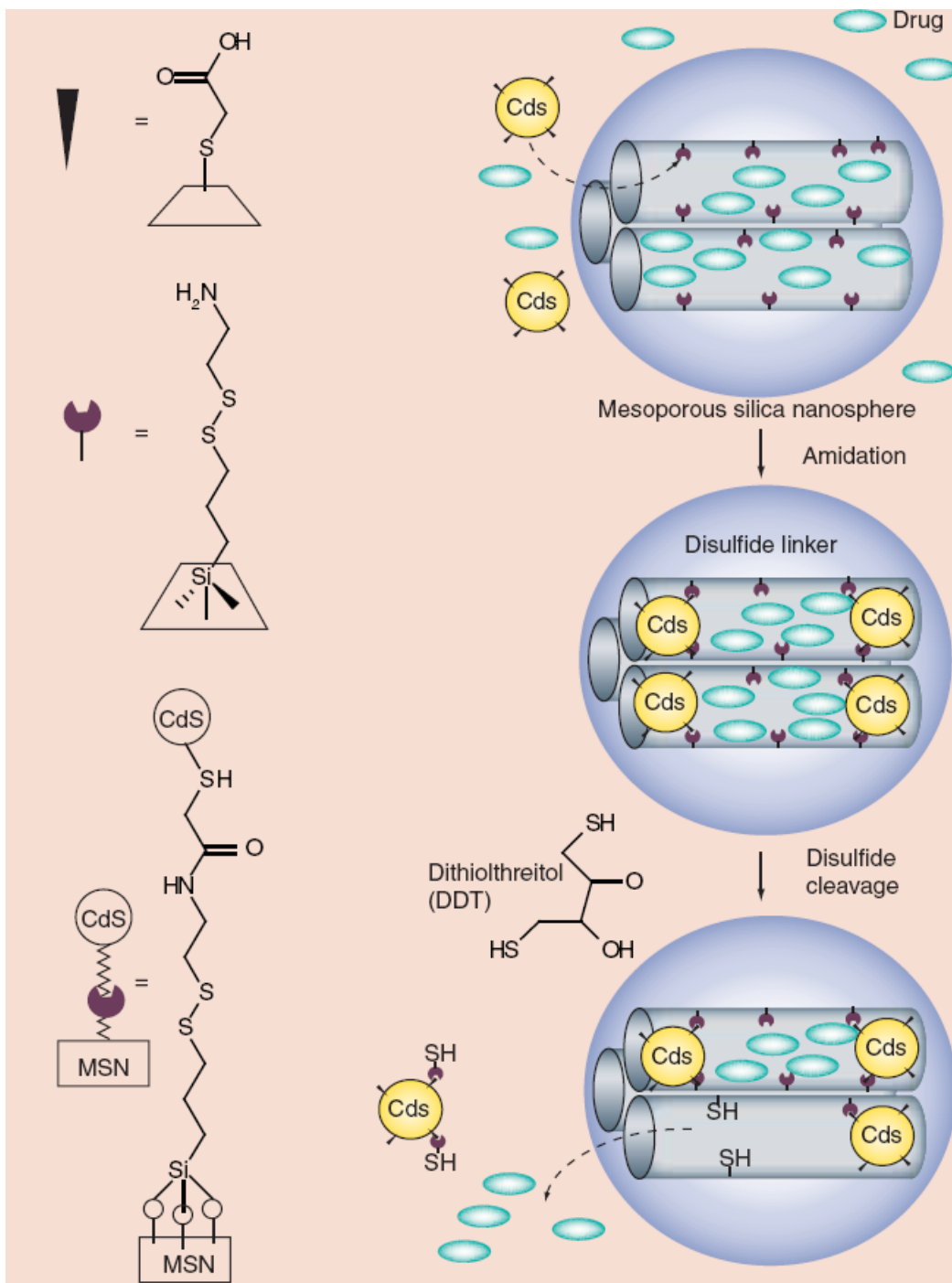
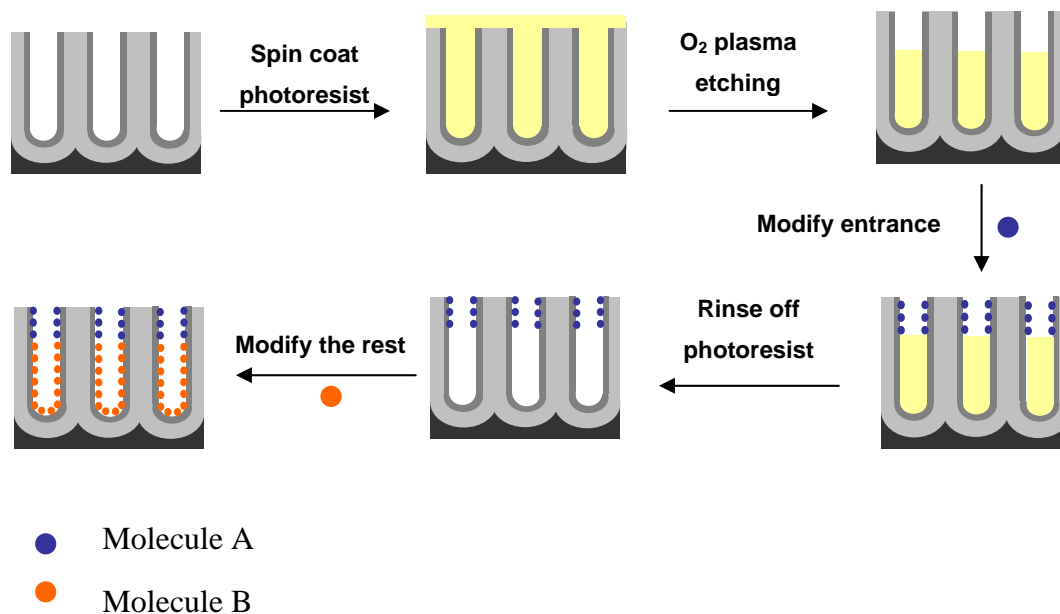


Figure 6.1 Schematic representation of the CdS nanoparticles-capped mesoporous silica nanoparticles-based drug delivery system [168]

6.1.2 Segmented functionalizations

In this chapter, the entrance of the silica nanotubes is modified differently from the remainder of the nanotubes. Photoresist is used as a mask for differential modification of the inner surface along the nanotubes, as shown in Scheme 6.1. Briefly, the pores of a silica-coated alumina template are filled with photoresist by spin-coating. With O_2 plasma etching, the photoresist at the entrance of the pore structure is etched off. The exposed surface of the pores can then be modified with molecule A. The remainder can be modified with molecule B after the photoresist is removed. In this way, the modification at the entrance of the pore can be different from the rest of the pore.

Scheme 6.1 Segmented modifications



6.1.3 Dry etching

The etching process involves transport of reactants to the surface of a substrate, surface reaction and transport of products from the surface. The advantage of dry etching over wet etching is its ability in defining small features since the reaction occurs in the gas phase. Dry etching technology can be classified into three types based on the etching mechanisms: physical sputtering, plasma etching and reactive ion etching. The etching mechanism changes with the ion energy which decreases with the pressure, as shown in Figure 6.2[169]. Physical sputtering requires the highest ion energy among these three. It relies on ion bombardment to remove the targeted materials. Plasma etching is achieved through plasma assisted chemical reactions. It requires the lowest ion energy among these three. The ions constantly bombard the surface and create damage in the form of unsatisfied bonds that are exposed to the reactive radicals. The radicals diffuse to the surface, quickly react to form volatile products, and are pumped away. Reactive ion etching combines these two mechanism[170].

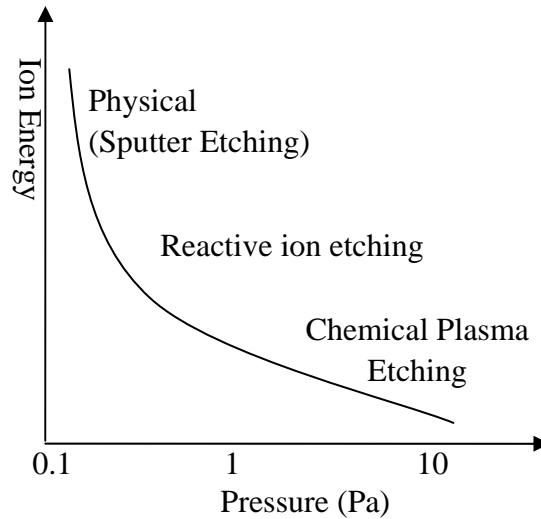


Figure 6.2 Ion striking energy decreases with pressure and the mechanism changes with the pressure [169]

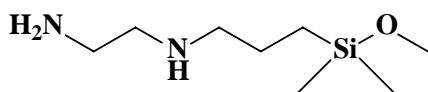
Plasma processing has gained wide use in materials processing because similar and more successful results cannot be attained using wet chemical etching. However, as the feature size decreases, the control of microscopic uniformity in high aspect ratio etching is becoming more and more challenging. It has been widely reported that smaller diameter holes and narrower trenches etch more slowly than larger diameter holes and wider trenches when the dimensions are below 1 μm . Many models have been built to qualitatively understand the dependence of etching rates on feature size. However, due to the complexity of the etching environment including the etch process parameters (pressure, rf power, etching gas chemistry, temperature) and the physical and chemical process parameters (energy and angular distribution of ions and neutrals, radical sticking, and surface charging), it is hard to make accurate profile predictions. Gottscho and Jurgensen have classified the effects contributing to the feature size dependent

etching rates into two categories: (1) aspect ratio dependent etching (ARDE), and (2) microloading [171]. ARDE is related with the transport of ions and neutrals in a microstructure. Typically, there is a substantial difference in mobility between electrons and ions. The electrons have a large angular distribution while the ion flux is quite directional[172]. This difference leading to localized surface charging becomes important with increased aspect ratio. Since the etching rate depends on the angular and energy distribution of the ions and neutrals flux, these factors will influence the etching profile. Microloading is due to inefficient supply of reactants under conditions where the etching reaction is reactant transport-rate-limited. This phenomenon is generally observed with a closely packed array.

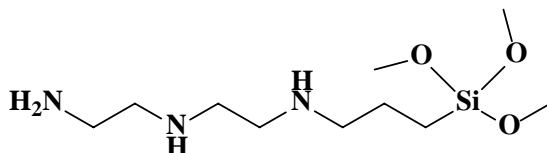
6.2 Experimental design

6.2.1 Materials

The silane agents were obtained from Gelest (Morrisville, PA), including (3-Trimethoxysilylpropyl)diethylenetriamine (95%, DETA-silane) and n-(2-aminoethyl)-3-aminoisobutyldimethylmethoxysilane (95%, ADMM-silane). Amine-reactive fluorescent probes Alexa Fluor 488 carboxylic acid 2,3,5,6-tetrafluorophenyl ester (Alexa Fluor 488), Alexa Fluor 555 carboxylic acid, succinimidyl ester (Alexa Fluor 555) and thiol-reactive probe Alexa Fluor 555 C2 maleimide (Alexa Fluor 555 C2) were obtained from Invitrogen (Eugene, Oregon). Traut's reagent (2-iminothiolane HCl, Thermo Scientific, IL, USA) was used to modify amine and introduce sulfhydryl functional groups.



n-(2-aminoethyl)-3-aminoisobutyldimethylmethoxysilane (ADMM-silane)



(3-Trimethoxysilylpropyl)diethylenetriamine (DETA-silane)

The preparation of anodic aluminum oxide (AAO) templates and the synthesis of silica nanotubes (SNTs) were introduced in Chapter 2. The SNT morphology was characterized by field emission scanning electron microscopy (SEM, Hitachi S-4700) and ZEISS EM10CA transmission electron microscopy (TEM) operating at 80 kV.

6.2.2 Modifications of the inner surfaces of silica nanotubes

The inner surfaces of silica nanotubes were modified when the nanotubes were still embedded in the AAO template. Specifically, the silica coated AAO was first immersed in silane in 95% ethanol-water at room temperature, rinsed with ethanol, and then cured at 120 °C for 20 min. For DETA, the silane concentration was 5% and the immersion time was 30 min. For ADMM, due to its lower reactivity than DETA, the concentration used was 10% and the immersion time was increased to 10 hrs. The amine functional groups were later used as linkers for fluorescent probes.

6.2.3 Photoresist coating

After silane modification, the silica coated AAO was rinsed with acetone, isopropanol, and baked at 120 °C for 10 min. A drop of photoresist, Shipley 1813, was spread on the top of the AAO for 2 min. Spin-coating was carried out at 6,000 RPM for 40 seconds. The sample was then soft-baked at 95 °C for 1 min and hard-baked at 120 °C for 5 min.

6.3.4 O₂ plasma etching

To study the etching rate, silica coated AAO template was used. After spin coating with photoresist, the sample was placed in a plasma chamber (Technics Model PE-IIA), as schematically shown in Figure 6.3. The chamber pressure was pumped down to 50 to 60 mTorr. Oxygen gas was then flushed in until the pressure reached 300 mTorr. The power was set to 100 W. The etching time ranged from 1 min to 4 min. Free standing silica nanotubes were obtained after the AAO template was selectively dissolved with 25% phosphoric acid.

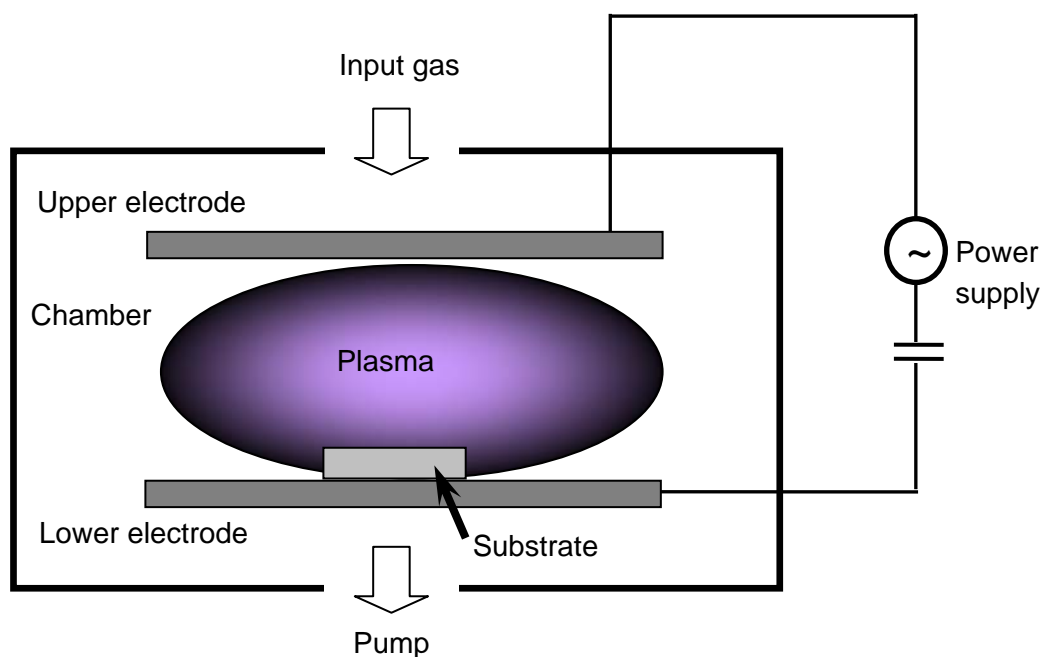


Figure 6.3 Schematic illustration of a plasma etching system

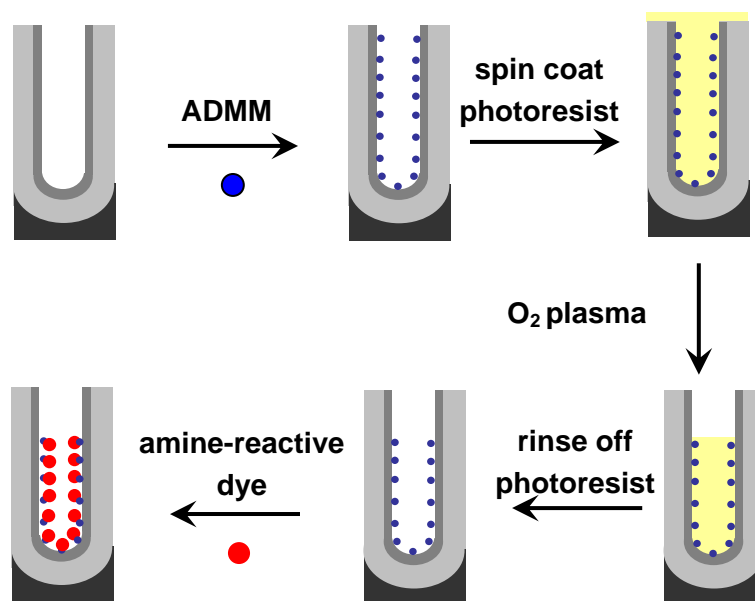
6.3.5 Segmented functionalization of nanotubes

The methodology is outlined in Scheme 6.2. Two sets of experiment were carried out. Method 1: The silica coated AAO was modified with ADMM, then spin-coated with photoresist. After dry etching by O_2 plasma, the photoresist was rinsed off with ethanol. The nanotubes were then freed from the template by selectively dissolving the template with 25% phosphoric acid and were labeled with amine-reactive fluorescence probes for optical imaging. Method 2: The silica-coated AAO was modified with DETA, then spin-coated with photoresist. After dry etching by O_2 plasma, the sample was dipped in Traut's reagent solution (2 mg/ml in 0.1 M sodium bicarbonate solution) for 2 hrs for thiolation. After the sample was rinsed with water and ethanol, the embedded nanotubes were released from the template and collected with filtration. The nanotubes first reacted with

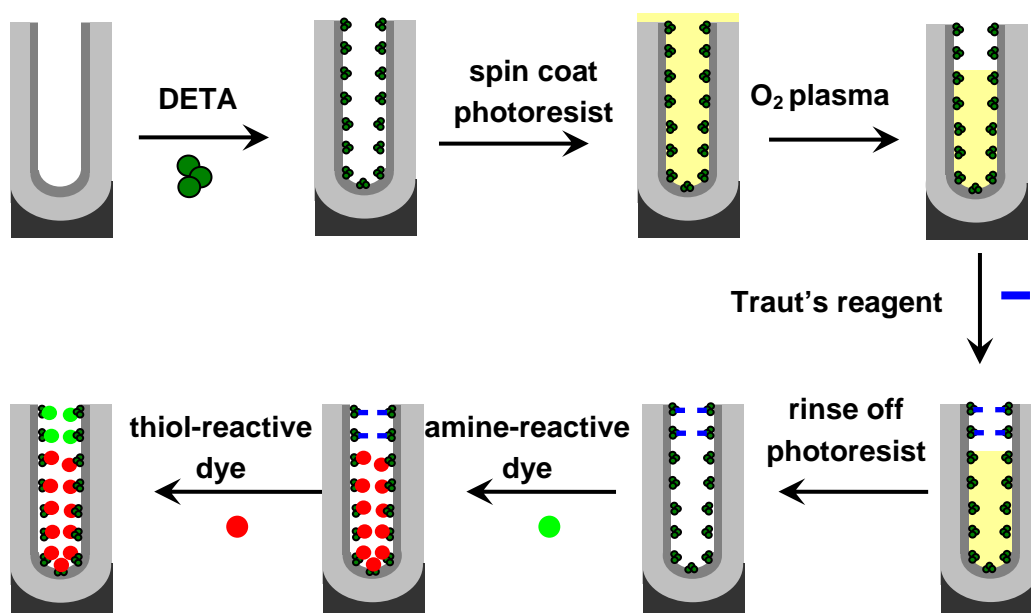
thiol-reactive fluorescence probes and then with amine-reactive probes. The fluorescence images of these nanotubes were taken with fluorescence microscopy (Zeiss, Axioskop 2 MAT).

Scheme 6.2 Two methods on segmented modification of nanotubes

Method 1.



Method 2



6.3 Results and discussions

Figure 6.4 shows the scanning microscopy images of silica coated AAO. The transmission microscopy images of the silica nanotubes with inner pore blocked with photoresist are illustrated in Figure 6.5.

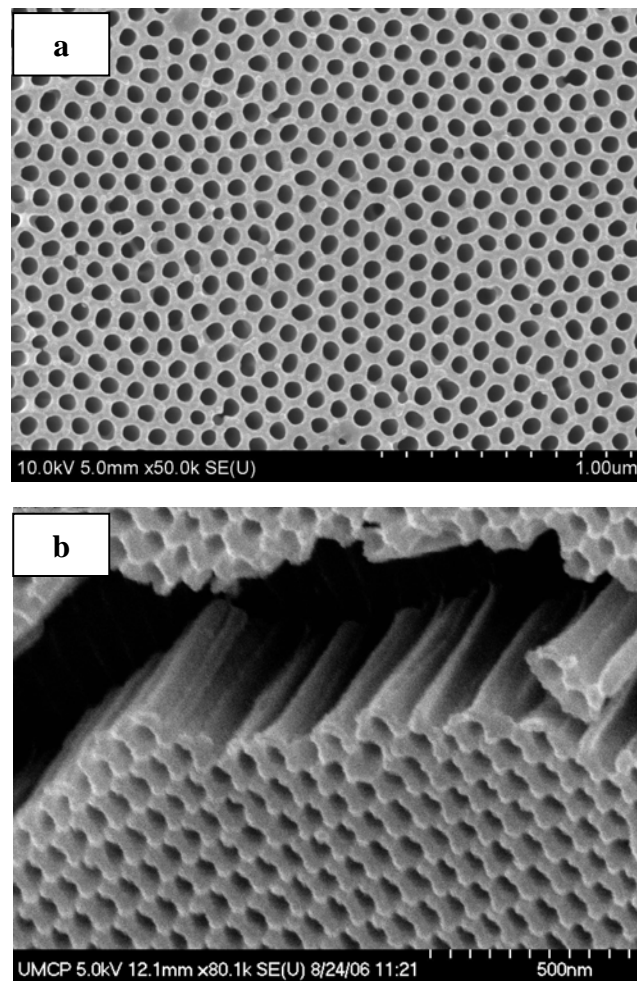


Figure 6.4 Scanning microscopy images of silica coated AAO, (a) top view and (b) side view

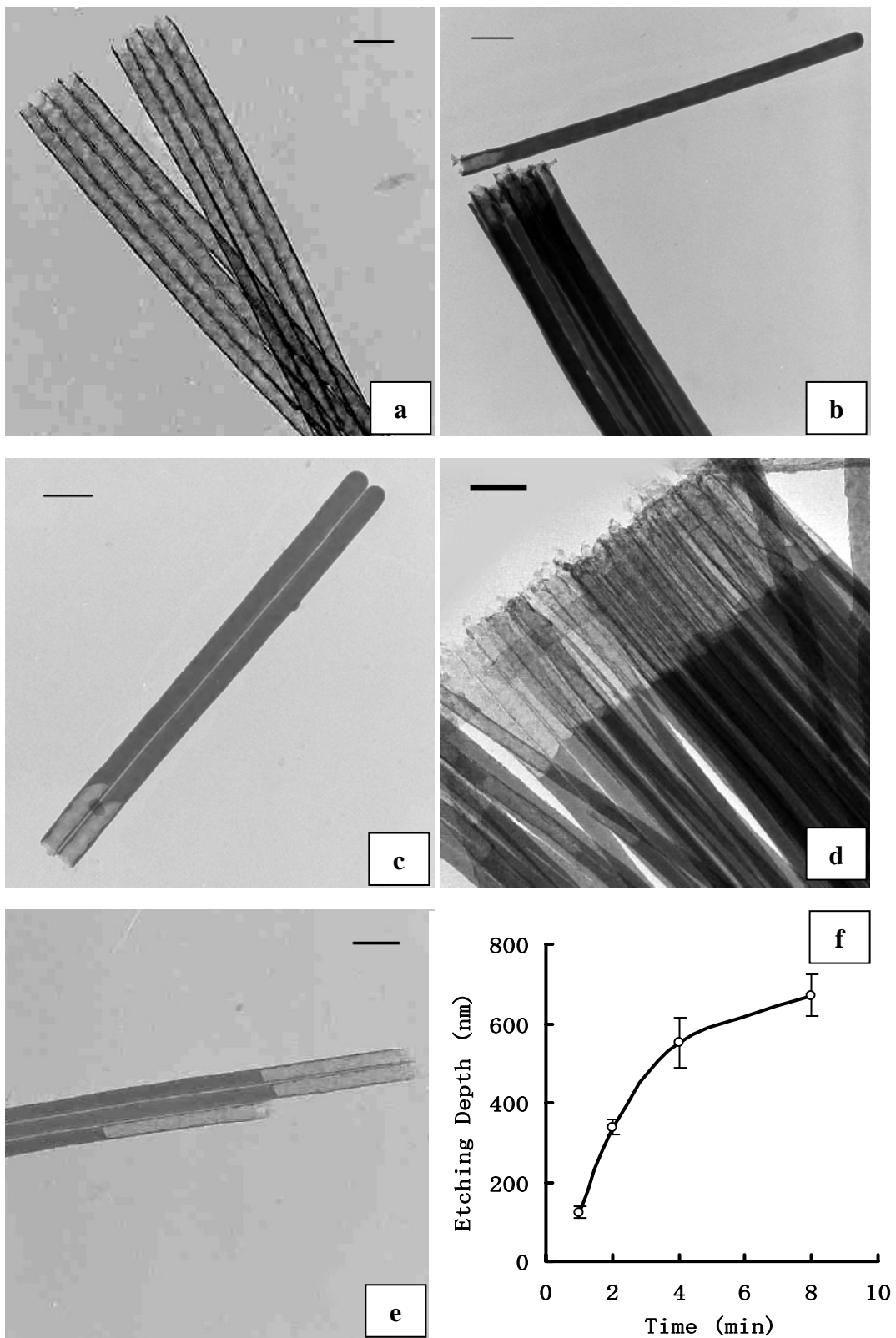


Figure 6.5 Transmission electron microscope (TEM) images of silica nanotubes before photoresist loading (a), and after photoresist loading with O_2 plasma etching time of 1 min (b), 2 min (c), 4 min (d), and 8 min (e). Scale bar: 200 nm

As shown in Figure 6.5, the etching depth increased with O₂ plasma etching time while the etching rate decreased with the etching time. The difference in etching rates can be attributed to the change in the aspect ratio. As the etching proceeds, the aspect ratio continually increases, and the etching rates decrease. This result can be explained by ARDE and/or microloading, as introduced in 6.1.3.

Figure 6.6 shows optical images of segmented-modified nanotubes based on method 1. The AMMD-silane modified nanotubes were partially labeled with fluorescent dye molecules, which indicate the success of the segmented modifications. However, the methods did not seem to work for the DETA-silane modified nanotubes. This difference may be explained by the different structure of the modification layer generated on the inner surfaces of the nanotubes. For the AMMD-silane modified surface, a mono-layer with amine functional groups was produced. When the top layers of photoresist were removed, the side chain of the AMMD-silane, which was linked to the nanotubes at the entrance, was exposed and then cleaved with the oxygen plasma during dry etching. The modification layer that was covered with photoresist was protected and could further react with amine-active probes. This can lead to the segmented modification of the probes in the step thereafter. For the DETA-silane modified nanotubes, the fluorescence images indicate that the amine functional groups were not completely removed by the O₂ plasma. This could be the result of the formation of protection layer leading to etching stop. The DETA-silane molecule has three ethoxy groups bound to Si compared to one for AMMD-silane molecule. The DETA-silane molecule may

form an oligomer before or during silane modification. This can lead to a formation of multi-layer deposition instead of a monolayer on the substrate. During the O₂ plasma etching process, the organic chains in the top layers were consumed and formed a crosslinked siloxane network. Since the transport of the oxygen radicals is quite directional under the low pressure, the siloxane network might act as an effective protection layer and hinder further cleavage of the organic side chains underneath the layer. The conversion of the top layer of SiOCH and SiCH film into a hydrophilic SiO₂-like porous material with O₂ plasma has been observed [173-175].

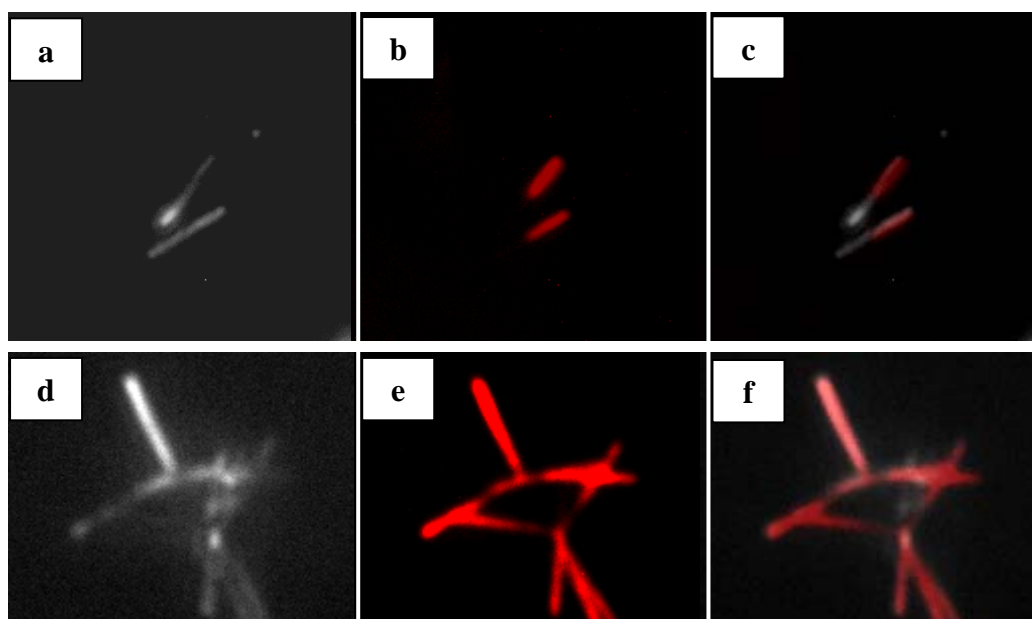


Figure 6.6 Optical images of differentially modified nanotubes based on method 1 with inner surfaces pre-modified with AMMD-silane (a and b), and nanotubes pre-modified with DETA-silane (c and d): (a, c) dark field images, (b, d) fluorescence images.

Figure 6.7 shows the fluorescence microscopic images of nanotubes modified with two probes. The results suggest that method 2 was effective for segmented modifications. However, the two color bands were not distinctive. The overlap of these two probes could be a result of nonspecific bonding. Additionally, it is possible that the reaction efficiency between the Traut's agent and the amine groups remained at the entrance after dry etching was not 100%. There were still some amine groups left and cause the existence of the amine-active probes at the entrance.

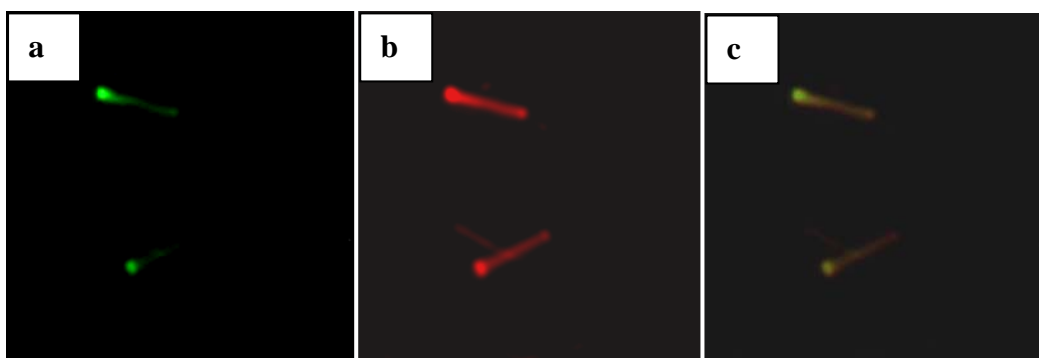


Figure 6.7 Fluorescence images of segmentedly modified nanotubes based on method 2 with inner surfaces pre-modified with DETA-silane. (a) with green dye filter, (b) with red dye filter, and (c) overlap of (a) and (b)

6.4 Conclusions

Nanotubes with their unique physical structure have potential advantages over spherical particles in terms of multifunctionality. The differential modifications between the inner and outer surfaces have been developed, as introduced in previous chapters. In this chapter, an novel method on segmented modifications

was developed. The results demonstrate that the method was effective even though more experiments need to be done to optimize the process parameters. With this segmented modification, nanotubes can work as a more efficient platform for biomedical applications.

Chapter 7 Conclusions and Future Work

As our circle of knowledge expands, so does the circumference of darkness surrounding it.

Albert Einstein

7.1 Conclusions

In this thesis, I developed a method of synthesis of magnetic nanotubes (MNTs). The structure of MNTs integrates the unique characteristics of SNTs, such as facile chemistry, robust mechanical properties, biocompatibility, and well-controlled dimensions, with the superparamagnetic properties of SPIONs. The saturation magnetization of MNT is as high as 95 emu/gFe, as described in Chapter 2.

In Chapter 3, I characterized MNTs as magnetic resonance contrast agents. The results demonstrated that MNTs enhanced proton magnetic resonance relaxation considerably, especially transverse relaxation. The transverse relaxivities r_2 (*) of MNTs are even higher than the values for Feridex, a FDA approved MR contrast agent, indicating that MNTs could potentially act as an efficacious T2-weighted MRI contrast agents.

I modified MNTs with pyridine-silane and C18-silane and used them as drug carriers to control the release profile of Dox (Chapter 5). The interaction between the inner surface modified layer of MNT and Dox varies with pH. The results showed that Dox molecules held in the MNTs were stable at pH 7.2, and released at pH 4.5. It indicates that the modification was effective in controlling the drug release profiles.

Additionally, the barrier effect of the magnetic nanoparticles in the nanotubes helped in holding the drug molecules.

I completed in-vitro cell labeling with MNTs, as introduced in Chapter 4. The preliminary studies on the in vitro cell labeling with MNTs reveal that the MNTs are not toxic, and the labeling is effective. To study the effect of structural and functional properties of nanotubes on cellular uptake and interactions, I did experiments on cytotoxicity and cellular uptake of SNTs with two different sizes and surface charges in primary (non-malignant) and cancer cell models were described. The nanotubes showed limited toxicity which was concentration-, surface charge-, and length-dependent and were internalized in cells at least in part by endocytosis.

In Chapter 6, I designed a scheme to modify the nanotubes segmentally between the entrance and the remainder of the nanotube. The idea is to design a universal delivery vehicle that can be filled with a payload and has a cap which can be released in the environment where the drug molecules are to be delivered. I did some proof-of-concept experiments. The results showed that the scheme was workable.

7.2 Future work

In this work, silica nanotubes/magnetic nanotubes are shown to be a promising candidate for biomedical applications. All the work done so far is just a start. More work need to be done to optimize the experimental conditions for materials synthesis and modifications. To continue the study on drug controlled release, we need data on long-term release and cumulative drug release before in vivo experiment. For the cellular work, more experiments need to be performed to find the optimum

parameters, such as the surface charging, dimensions, concentration of nanotubes for cell labeling and cellular uptake. For all the possible clinical applications, the *in vivo* capabilities and limitations of SNTs need to be explored. Data on biodistribution would be very interesting. The pharmacokinetic parameters of *in vivo* administered functionalized SNTs need to be characterized for various therapeutic and diagnostic applications.

With silica nanotubes as the constitute material, we can develop multimode imaging contrast agents combining MR with optical detection. Together with biomolecular targeting capabilities, we can obtain efficacious drug delivery modalities. Finally, we can achieve *in vivo* imaging-monitored drug delivery.

References:

1. www.azonano.com/news.asp?newsID=650, *Nanotechnology-Enabled Drug Delivery Systems Will Generate Over \$1.7 billion in 2009*. March 22nd, 2005.
2. Duncan, R: The dawning era of polymer therapeutics. *Nature Reviews Drug Discovery* 2, 347-360 (2003).
3. Ferrari, M: Cancer nanotechnology: Opportunities and challenges. *Nature Reviews Cancer* 5, 161-171 (2005).
4. King, FD, ed. *Medicinal chemistry: principles and practice*. 1994, The Royal Society of Chemistry: Cambridge.
5. Vaupel, P, F Kallinowski, P Okunieff: Blood-Flow, Oxygen and Nutrient Supply, and Metabolic Microenvironment of Human-Tumors - a Review. *Cancer Research* 49, 6449-6465 (1989).
6. Peer, D, JM Karp, S Hong, OC FaroKhazad, R Margalit, R Langer: Nanocarriers as an emerging platform for cancer therapy. *Nature Nanotechnology* 2, 751-760 (2007).
7. Torchilin, VP: Recent advances with liposomes as pharmaceutical carriers. *Nature Reviews Drug Discovery* 4, 145-160 (2005).
8. Hobbs, SK, WL Monsky, F Yuan *et al.*: Regulation of transport pathways in tumor vessels: Role of tumor type and microenvironment. *Proceedings of the National Academy of Sciences of the United States of America* 95, 4607-4612 (1998).
9. Brooks, PC, RAF Clark, DA Cheresh: Requirement of Vascular Integrin Alpha(V)Beta(3) for Angiogenesis. *Science* 264, 569-571 (1994).
10. Kim, KJ, B Li, J Winer *et al.*: Inhibition of Vascular Endothelial Growth Factor-Induced Angiogenesis Suppresses Tumor-Growth In Vivo. *Nature* 362, 841-844 (1993).
11. Moghimi, SM, AC Hunter, JC Murray: Long-circulating and target-specific nanoparticles: Theory to practice. *Pharmacological Reviews* 53, 283-318 (2001).
12. Ulbrich, K, V Subr: Polymeric anticancer drugs with pH-controlled activation. *Advanced Drug Delivery Reviews* 56, 1023-1050 (2004).
13. Alper, J, *Why nano*. September 2005, NCI alliance for nanotechnology in cancer, Monthly feature.
14. Ehrlich, P: The partial function of cells. *International Archives of Allergy and Applied Immunology* 5, 67-86 (1954).
15. El-Sayed, MEH, AS Hoffman, PS Stayton: Rational design of composition and activity correlations for pH-sensitive and glutathione-reactive polymer therapeutics. *Journal of Controlled Release* 101, 47-58 (2005).
16. Park John, W: Liposome-based drug delivery in breast cancer treatment. *Breast cancer research : BCR* 4, 95-9 (2002).
17. Singh, R, D Pantarotto, L Lacerda *et al.*: Tissue biodistribution and blood clearance rates of intravenously administered carbon nanotube radiotracers. *Proceedings of the National Academy of Sciences of the United States of America* 103, 3357-3362 (2006).

18. Sayes, CM, F Liang, JL Hudson *et al.*: Functionalization density dependence of single-walled carbon nanotubes cytotoxicity in vitro. *Toxicology Letters* 161, 135-142 (2006).
19. Hillebrenner, H, F Buyukserin, JD Stewart, CR Martin: Template synthesized nanotubes for biomedical delivery applications. *Nanomedicine (London, United Kingdom)* 1, 39-50 (2006).
20. Klumpp, C, K Kostarelos, M Prato, A Bianco: Functionalized carbon nanotubes as emerging nanovectors for the delivery of therapeutics. *Biochimica Et Biophysica Acta-Biomembranes* 1758, 404-412 (2006).
21. Bianco, A, M Prato: Can carbon nanotubes be considered useful tools for biological applications? *Advanced Materials (Weinheim, Germany)* 15, 1765-1768 (2003).
22. Pantarotto, D, R Singh, D McCarthy *et al.*: Functionalized carbon nanotubes for plasmid DNA gene delivery. *Angewandte Chemie-International Edition* 43, 5242-5246 (2004).
23. Zheng, M, A Jagota, MS Strano *et al.*: Structure-based carbon nanotube sorting by sequence-dependent DNA assembly. *Science* 302, 1545-1548 (2003).
24. Lam, CW, JT James, R McCluskey, RL Hunter: Pulmonary toxicity of single-wall carbon nanotubes in mice 7 and 90 days after intratracheal instillation. *Toxicological Sciences* 77, 126-134 (2004).
25. Worle-Knirsch, JM, K Pulskamp, HF Krug: Oops they did it again! Carbon nanotubes hoax scientists in viability assays. *Nano Letters* 6, 1261-1268 (2006).
26. Oberdorster, E: Manufactured nanomaterials (fullerenes, C60) induce oxidative stress in the brain of juvenile largemouth bass. *Environmental Health Perspectives* 112, 1058-1062 (2004).
27. Kam, NWS, ZA Liu, HJ Dai: Carbon nanotubes as intracellular transporters for proteins and DNA: An investigation of the uptake mechanism and pathway. *Angewandte Chemie-International Edition* 45, 577-581 (2006).
28. Cai, D, JM Mataraza, ZH Qin *et al.*: Highly efficient molecular delivery into mammalian cells using carbon nanotube spearing. *Nature Methods* 2, 449-454 (2005).
29. Botterhuis, NE, QY Sun, P Magusin, RA van Santen, N Sommerdijk: Hollow silica spheres with an ordered pore structure and their application in controlled release studies. *Chemistry-a European Journal* 12, 1448-1456 (2006).
30. Vallet-Regi, M, A Ramila, RP del Real, J Perez-Pariente: A new property of MCM-41: Drug delivery system. *Chemistry of Materials* 13, 308-311 (2001).
31. Radu, DR, CY Lai, K Jeftinija, EW Rowe, S Jeftinija, VSY Lin: A polyamidoamine dendrimer-capped mesoporous silica nanosphere-based gene transfection reagent. *Journal of the American Chemical Society* 126, 13216-13217 (2004).
32. Lai, CY, BG Trewyn, DM Jeftinija *et al.*: A mesoporous silica nanosphere-based carrier system with chemically removable CdS nanoparticle caps for stimuli-responsive controlled release of neurotransmitters and drug molecules. *Journal of the American Chemical Society* 125, 4451-4459 (2003).

33. Giri, S, BG Trewyn, MP Stellmaker, VSY Lin: Stimuli-responsive controlled-release delivery system based on mesoporous silica nanorods capped with magnetic nanoparticles. *Angewandte Chemie-International Edition* 44, 5038-5044 (2005).
34. Sun, XM, YD Li: Hollow carbonaceous capsules from glucose solution. *Journal of Colloid and Interface Science* 291, 7-12 (2005).
35. Sitharaman, B, KR Kissell, KB Hartman *et al.*: Superparamagnetic gadonanotubes are high-performance MRI contrast agents. *Chemical Communications* 3915-3917 (2005).
36. Roy, I, S Mitra, A Maitra, S Mozumdar: Calcium phosphate nanoparticles as novel non-viral vectors for targeted gene delivery. *International Journal of Pharmaceutics* 250, 25-33 (2003).
37. Schmidt, HT, AE Ostafin: Liposome directed growth of calcium phosphate nanoshells. *Advanced Materials* 14, 532-+ (2002).
38. Martin, CR: Nanomaterials - a Membrane-Based Synthetic Approach. *Science* 266, 1961-1966 (1994).
39. Martin, CR, P Kohli: The emerging field of nanotube biotechnology. *Nature Reviews Drug Discovery* 2, 29-37 (2003).
40. Masuda, H, K Fukuda: Ordered Metal Nanohole Arrays Made by a 2-Step Replication of Honeycomb Structures of Anodic Alumina. *Science* 268, 1466-1468 (1995).
41. Li, AP, F Muller, A Birner, K Nielsch, U Gosele: Hexagonal pore arrays with a 50-420 nm interpore distance formed by self-organization in anodic alumina. *Journal of Applied Physics* 84, 6023-6026 (1998).
42. Mitchell, DT, SB Lee, L Trofin *et al.*: Smart nanotubes for bioseparations and biocatalysis. *Journal of the American Chemical Society* 124, 11864-11865 (2002).
43. Chen, C-C, Y-C Liu, C-H Wu, C-C Yeh, M-T Su, Y-C Wu: Preparation of fluorescent silica nanotubes and their application in gene delivery. *Advanced Materials (Weinheim, Germany)* 17, 404-407 (2005).
44. Son, SJ, J Reichel, B He, M Schuchman, SB Lee: Magnetic nanotubes for magnetic-field-assisted bioseparation, biointeraction, and drug delivery. *Journal of the American Chemical Society* 127, 7316-7317 (2005).
45. Kovtyukhova, NI, TE Mallouk, TS Mayer: Templated surface sol-gel synthesis of SiO₂ nanotubes and SiO₂-insulated metal nanowires. *Advanced Materials (Weinheim, Germany)* 15, 780-785 (2003).
46. Berger, P, NB Adelman, KJ Beckman, DJ Campbell, AB Ellis, GC Lisensky: Preparation and properties of an aqueous ferrofluid. *Journal of Chemical Education* 76, 943-948 (1999).
47. Lee, D, RE Cohen, MF Rubner: Heterostructured magnetic nanotubes. *Langmuir* 23, 123-129 (2007).
48. Hillebrenner, H, F Buyukserin, M Kang, MO Mota, JD Stewart, CR Martin: Corking nano test tubes by chemical self-assembly. *Journal of the American Chemical Society* 128, 4236-4237 (2006).

49. Son, SJ,SB Lee: Controlled gold nanoparticle diffusion in nanotubes: Platform of partial functionalization and gold capping. *Journal of the American Chemical Society* 128, 15974-15975 (2006).
50. Jana, NR, L Gearheart,CJ Murphy: Seed-mediated growth approach for shape-controlled synthesis of spheroidal and rod-like gold nanoparticles using a surfactant template. *Advanced Materials (Weinheim, Germany)* 13, 1389-1393 (2001).
51. Jaffer, FA,R Weissleder: Molecular imaging in the clinical arena. *Jama- Journal of the American Medical Association* 293, 855-862 (2005).
52. McNeil, SE: Nanotechnology for the biologist. *Journal of Leukocyte Biology* 78, 585-594 (2005).
53. Medintz, IL, HT Uyeda, ER Goldman,H Mattoussi: Quantum dot bioconjugates for imaging, labelling and sensing. *Nature Materials* 4, 435-446 (2005).
54. Michalet, X, FF Pinaud, LA Bentolila *et al.*: Quantum dots for live cells, in vivo imaging, and diagnostics. *Science* 307, 538-544 (2005).
55. Ow, H, DR Larson, M Srivastava, BA Baird, WW Webb,U Wiesner: Bright and stable core-shell fluorescent silica nanoparticles. *Nano Letters* 5, 113-117 (2005).
56. Luo, D: Nanotechnology and DNA delivery. *Mrs Bulletin* 30, 654-658 (2005).
57. Shaffer, C: Nanomedicine transforms drug delivery. *Drug Discovery Today* 10, 1581-1582 (2005).
58. Wang, L, KM Wang, S Santra *et al.*: Watching silica nanoparticles glow in the biological world. *Analytical Chemistry* 78, 646-654 (2006).
59. Zhao, XJ, RP Bagwe,WH Tan: Development of organic-dye-doped silica nanoparticles in a reverse microemulsion. *Advanced Materials* 16, 173-+ (2004).
60. Loo, C, A Lowery, N Halas, J West,R Drezek: Immunotargeted nanoshells for integrated cancer imaging and therapy. *Nano Letters* 5, 709-711 (2005).
61. Taylor, KML, JS Kim, WJ Rieter, H An, WL Lin,WB Lin: Mesoporous silica nanospheres as highly efficient MRI contrast agents. *Journal of the American Chemical Society* 130, 2154-+ (2008).
62. Titirici, MM, M Antonietti,A Thomas: A generalized synthesis of metal oxide hollow spheres using a hydrothermal approach. *Chemistry of Materials* 18, 3808-3812 (2006).
63. Wang, LB, Jie; Wang, Lun; Zhang, Fang; Li, Yadong: One-pot synthesis and bioapplication of amine functionalized magnetite nanoparticles and hollow nanospheres. *Chemistry - A European Journal* 12, 6341-6347 (2006).
64. Bao, G,XR Bao: Shedding light on the dynamics of endocytosis and viral budding. *Proceedings of the National Academy of Sciences of the United States of America* 102, 9997-9998 (2005).
65. Decuzzi, P,M Ferrari: The receptor-mediated endocytosis of nonspherical particles. *Biophysical Journal* 94, 3790-3797 (2008).
66. Gao, HJ, WD Shi,LB Freund: Mechanics of receptor-mediated endocytosis. *Proceedings of the National Academy of Sciences of the United States of America* 102, 9469-9474 (2005).

67. Marsh, M, A Helenius: Virus entry: Open sesame. *Cell* 124, 729-740 (2006).
68. Chithrani, BD, AA Ghazani, WCW Chan: Determining the size and shape dependence of gold nanoparticle uptake into mammalian cells. *Nano Letters* 6, 662-668 (2006).
69. Chithrani, BD, WCW Chan: Elucidating the mechanism of cellular uptake and removal of protein-coated gold nanoparticles of different sizes and shapes. *Nano Letters* 7, 1542-1550 (2007).
70. Kam, NWS, Z Liu, HJ Dai: Functionalization of carbon nanotubes via cleavable disulfide bonds for efficient intracellular delivery of siRNA and potent gene silencing. *Journal of the American Chemical Society* 127, 12492-12493 (2005).
71. Kostarelos, K, L Lacerda, G Pastorin *et al.*: Cellular uptake of functionalized carbon nanotubes is independent of functional group and cell type. *Nature Nanotechnology* 2, 108-113 (2007).
72. Geng, Y, P Dalhaimer, SS Cai *et al.*: Shape effects of filaments versus spherical particles in flow and drug delivery. *Nature Nanotechnology* 2, 249-255 (2007).
73. Jun, YW, Jang, J. T., and Cheon, J, *Magnetic resonance nanoparticle probes for cancer imaging*, in *Nanomaterials for cancer diagnosis*, C.S.S.R. Kumar, Editor. 2007, Wiley-VCH Verlag GmbH & Co. KGaA: Weinheim. p. 147-173.
74. Hyeon, T, SS Lee, J Park, Y Chung, H Bin Na: Synthesis of highly crystalline and monodisperse maghemite nanocrystallites without a size-selection process. *Journal of the American Chemical Society* 123, 12798-12801 (2001).
75. Park, J, E Lee, NM Hwang *et al.*: One-nanometer-scale size-controlled synthesis of monodisperse magnetic iron oxide nanoparticles. *Angewandte Chemie-International Edition* 44, 2872-2877 (2005).
76. Tillmann, C, Caruthers, D. S., Wickline, S. A., and Lanza, M. G., *Nanoparticles for magnetic resonance imaging of tumors*, in *Nanomaterials for cancer diagnosis*, C.S.S.R. Kumar, Editor. 2007, Wiley-VCH Verlag GmbH & Co. KGaA: Weinheim. p. 121-146.
77. Baker, LA, P Jin, CR Martin: Biomaterials and biotechnologies based on nanotube membranes. *Critical Reviews in Solid State and Materials Sciences* 30, 183-205 (2005).
78. He, B, SJ Son, SB Lee: Shape-coded silica nanotubes for biosensing. *Langmuir* 22, 8263-8265 (2006).
79. Kohli, P, CR Martin: Template-synthesized nanotubes for biotechnology and biomedical applications. *Journal of Drug Delivery Science and Technology* 15, 49-57 (2005).
80. Kohli, P, CR Martin: Smart nanotubes for biotechnology. *Current Pharmaceutical Biotechnology* 6, 35-47 (2005).
81. Lee, SB, DT Mitchell, L Trofin, TK Nevanen, H Soderlund, CR Martin: Antibody-based bio-nanotube membranes for enantiomeric drug separations. *Science* 296, 2198-2200 (2002).
82. Mitchell, DT, SB Lee, L Trofin *et al.*: Smart nanotubes for bioseparations and biocatalysis. *Journal of the American Chemical Society* 124, 11864-11865 (2002).

83. Hillebrenner, H, F Buyukserin, JD Stewart, CR Martin: Template synthesized nanotubes for biomedical delivery applications. *Nanomedicine* 1, 39-50 (2006).
84. Son, SJ, X Bai, A Nan, H Ghandehari, SB Lee: Template synthesis of multifunctional nanotubes for controlled release. *Journal of Controlled Release* 114, 143-152 (2006).
85. Ammar, S, A Helfen, N Jouini *et al.*: Magnetic properties of ultrafine cobalt ferrite particles synthesized by hydrolysis in a polyol medium. *Journal of Materials Chemistry* 11, 186-192 (2001).
86. Caruntu, D, Y Remond, NH Chou *et al.*: Reactivity of 3d transition metal cations in diethylene glycol solutions. Synthesis of transition metal ferrites with the structure of discrete nanoparticles complexed with long-chain carboxylate anions. *Inorganic Chemistry* 41, 6137-6146 (2002).
87. Deng, H, XL Li, Q Peng, X Wang, JP Chen, YD Li: Monodisperse magnetic single-crystal ferrite microspheres. *Angewandte Chemie-International Edition* 44, 2782-2785 (2005).
88. Feldmann, C, HO Jungk: Polyol-mediated preparation of nanoscale oxide particles. *Angewandte Chemie-International Edition* 40, 359-362 (2001).
89. Thompson, GEW, G. C., *Anodic Films on ALuminum*, in *Treatise on Materials Science and TEchnology*, J.C. Scully, Editor. 1983, Academic Press: New York. p. 205.
90. Jessensky, O, F Muller, U Gosele: Self-organized formation of hexagonal pore arrays in anodic alumina. *Applied Physics Letters* 72, 1173-1175 (1998).
91. Nielsch, K, J Choi, K Schwirn, RB Wehrspohn, U Gosele: Self-ordering regimes of porous alumina: The 10% porosity rule. *Nano Letters* 2, 677-680 (2002).
92. Kovtyukhova, NI, TE Mallouk, TS Mayer: Templated surface sol-gel synthesis of SiO₂ nanotubes and SiO₂-insulated metal nanowires. *Advanced Materials* 15, 780-785 (2003).
93. Bulte, JWM, AS Arbab, T Douglas, JA Frank, *Preparation of magnetically labeled cells for cell tracking by magnetic resonance imaging*, in *Imaging in Biological Research, Pt B*. 2004. p. 275-299.
94. Kalish, H, AS Arbab, BR Miller *et al.*: Combination of transfection agents and magnetic resonance contrast agents for cellular imaging: Relationship between relaxivities, electrostatic forces, and chemical composition. *Magnetic Resonance in Medicine* 50, 275-282 (2003).
95. Mao, HK, Takahashi, T, WA Bassett, GL Kinsland, L Merrill: Isothermal Compression of Magnetite to 320 Kbar and Pressure-Induced Phase-Transformation. *Journal of Geophysical Research* 79, 1165-1170 (1974).
96. Tartaj, P, MP Morales, S Veintemillas-Verdaguer, T Gonzalez-Carreño, aCJ Serna: Synthesis, properties and biomedical applications of magnetic nanoparticles. *Handbook of Magnetic Materials*, ed. K.H.J. Buschow. Vol. 16. 2006: Elsevier Science. 405-453.
97. Gupta, AK, M Gupta: Synthesis and surface engineering of iron oxide nanoparticles for biomedical applications. *Biomaterials* 26, 3995-4021 (2005).

98. Bomati-Miguel, O, MP Morales, P Tartaj *et al.*: Fe-based nanoparticulate metallic alloys as contrast agents for magnetic resonance imaging. *Biomaterials* 26, 5695-5703 (2005).
99. Chkoundali, S, S Ammar, N Jouini *et al.*: Nickel ferrite nanoparticles: elaboration in polyol medium via hydrolysis, and magnetic properties. *Journal of Physics-Condensed Matter* 16, 4357-4372 (2004).
100. Morales, MP, S Veintemillas-Verdaguer, MI Montero *et al.*: Surface and internal spin canting in gamma-Fe₂O₃ nanoparticles. *Chemistry of Materials* 11, 3058-3064 (1999).
101. He, YP, SQ Wang, CR Li, YM Miao, ZY Wu, BS Zou: Synthesis and characterization of functionalized silica-coated Fe₃O₄ superparamagnetic nanocrystals for biological applications. *Journal of Physics D-Applied Physics* 38, 1342-1350 (2005).
102. Goya, GF, TS Berquo, FC Fonseca, MP Morales: Static and dynamic magnetic properties of spherical magnetite nanoparticles. *Journal of Applied Physics* 94, 3520-3528 (2003).
103. Caruntu, D, G Caruntu, Y Chen, CJ O'Connor, G Goloverda, VL Kolesnichenko: Synthesis of variable-sized nanocrystals of Fe₃O₄ with high surface reactivity. *Chemistry of Materials* 16, 5527-5534 (2004).
104. Tromp, RM, JB Hannon: Thermodynamics of nucleation and growth. *Surface Review and Letters* 9, 1565-1593 (2002).
105. Cushing, BL, VL Kolesnichenko, CJ O'Connor: Recent advances in the liquid-phase syntheses of inorganic nanoparticles. *Chemical Reviews* 104, 3893-3946 (2004).
106. Liu, SR, QS Pu, L Gao, C Korzeniewski, C Matzke: From nanochannel-induced proton conduction enhancement to a nanochannel-based fuel cell. *Nano Letters* 5, 1389-1393 (2005).
107. Tas, NR, P Mela, T Kramer, JW Berenschot, A van den Berg: Capillarity induced negative pressure of water plugs in nanochannels. *Nano Letters* 3, 1537-1540 (2003).
108. Tsukahara, T, A Hibara, Y Ikeda, T Kitamori: NMR study of water molecules confined in extended nanospaces. *Angewandte Chemie-International Edition* 46, 1180-1183 (2007).
109. Louie, AY, MM Huber, ET Ahrens *et al.*: In vivo visualization of gene expression using magnetic resonance imaging. *Nature Biotechnology* 18, 321-325 (2000).
110. Artemov, D: Molecular magnetic resonance imaging with targeted contrast agents. *Journal of Cellular Biochemistry* 90, 518-524 (2003).
111. Jun, YW, JH Lee, J Cheon: Chemical design of nanoparticle probes for high-performance magnetic resonance imaging. *Angewandte Chemie-International Edition* 47, 5122-5135 (2008).
112. Dobson, J: Magnetic micro- and nano-particle-based targeting for drug and gene delivery. *Nanomedicine* 1, 31-37 (2006).
113. Duguet, E, S Vasseur, S Mornet, JM Devoisselle: Magnetic nanoparticles and their applications in medicine. *Nanomedicine* 1, 157-168 (2006).

114. Huh, YM, YW Jun, HT Song *et al.*: In vivo magnetic resonance detection of cancer by using multifunctional magnetic nanocrystals. *Journal of the American Chemical Society* 127, 12387-12391 (2005).
115. Mulder, WJM, GJ Strijkers, GAF van Tilborg, AW Griffioen, K Nicolay: Lipid-based nanoparticles for contrast-enhanced MRI and molecular imaging. *Nmr in Biomedicine* 19, 142-164 (2006).
116. Song, HT, JS Choi, YM Huh *et al.*: Surface modulation of magnetic nanocrystals in the development of highly efficient magnetic resonance probes for intracellular labeling. *Journal of the American Chemical Society* 127, 9992-9993 (2005).
117. Arbab, AS, V Frenkel, SD Pandit *et al.*: Magnetic resonance imaging and confocal microscopy studies of magnetically labeled endothelial progenitor cells trafficking to sites of tumor angiogenesis. *Stem Cells* 24, 671-678 (2006).
118. Arbab, AS, EK Jordan, LB Wilson, GT Yocum, BK Lewis, JA Frank: In vivo trafficking and targeted delivery of magnetically labeled stem cells. *Human Gene Therapy* 15, 351-360 (2004).
119. Bulte, JWM, T Douglas, B Witwer *et al.*: Magnetodendrimers allow endosomal magnetic labeling and in vivo tracking of stem cells. *Nature Biotechnology* 19, 1141-1147 (2001).
120. Zhao, M, DA Beauregard, L Loizou, B Davletov, KM Brindle: Non-invasive detection of apoptosis using magnetic resonance imaging and a targeted contrast agent. *Nature Medicine* 7, 1241-1244 (2001).
121. Blasberg, RG: Molecular imaging and cancer. *Molecular Cancer Therapeutics* 2, 335-343 (2003).
122. Martina, MS, JP Fortin, C Menager *et al.*: Generation of superparamagnetic liposomes revealed as highly efficient MRI contrast agents for in vivo imaging. *Journal of the American Chemical Society* 127, 10676-10685 (2005).
123. Berret, JF, N Schonbeck, F Gazeau *et al.*: Controlled Clustering of Superparamagnetic Nanoparticles Using Block Copolymers: Design of New Contrast Agents for Magnetic Resonance Imaging. *J. Am. Chem. Soc.* 128, 1755-1761 (2006).
124. Zocchi, E, M Tonetti, C Polvani, L Guida, U Benatti, A Deflora: Encapsulation of Doxorubicin in Liver-Targeted Erythrocytes Increases the Therapeutic Index of the Drug in a Murine Metastatic Model. *Proceedings of the National Academy of Sciences of the United States of America* 86, 2040-2044 (1989).
125. Lackey, CA, OW Press, AS Hoffman, PS Stayton: A biomimetic pH-responsive polymer directs endosomal release and intracellular delivery of an endocytosed antibody complex. *Bioconjugate Chemistry* 13, 996-1001 (2002).
126. Etrych, T, M Jelinkova, B Rihova, K Ulbrich: New HPMA copolymers containing doxorubicin bound via pH-sensitive linkage: synthesis and preliminary in vitro and in vivo biological properties. *Journal of Controlled Release* 73, 89-102 (2001).
127. Gao, ZG, DH Lee, DI Kim, YH Bae: Doxorubicin loaded pH-sensitive micelle targeting acidic extracellular pH of human ovarian A2780 tumor in mice. *Journal of Drug Targeting* 13, 391-397 (2005).

128. Lee, ES, K Na, YH Bae: Doxorubicin loaded pH-sensitive polymeric micelles for reversal of resistant MCF-7 tumor. *Journal of Controlled Release* 103, 405-418 (2005).
129. Shuai, XT, H Ai, N Nasongkla, S Kim, JM Gao: Micellar carriers based on block copolymers of poly(ϵ -caprolactone) and poly(ethylene glycol) for doxorubicin delivery. *Journal of Controlled Release* 98, 415-426 (2004).
130. Wang, C-H, C-H Wang, G-H Hsiue: Polymeric micelles with a pH-responsive structure as intracellular drug carriers. *Journal of Controlled Release* 108, 140-149 (2005).
131. Kataoka, K, T Matsumoto, M Yokoyama *et al.*: Doxorubicin-loaded poly(ethylene glycol)-poly(β -benzyl-L-aspartate) copolymer micelles: their pharmaceutical characteristics and biological significance. *Journal of Controlled Release* 64, 143-153 (2000).
132. Pham, T, JB Jackson, NJ Halas, TR Lee: Preparation and characterization of gold nanoshells coated with self-assembled monolayers. *Langmuir* 18, 4915-4920 (2002).
133. Martin, TJ, K Prochazka, P Munk, SE Webber: pH-dependent micellization of poly(2-vinylpyridine)-block-poly(ethylene oxide). *Macromolecules* 29, 6071-6073 (1996).
134. Juliano, R: Challenges to macromolecular drug delivery. *Biochemical Society Transactions* 35, 41-43 (2007).
135. Bai, X, SJ Son, SX Zhang *et al.*: Synthesis MRI of superparamagnetic nanotubes as contrast agents and for cell labeling. *Nanomedicine* 3, 163-174 (2008).
136. Weetall, HH: Storage Stability of Water-Insoluble Enzymes Covalently Coupled to Organic and Inorganic Carriers. *Biochimica Et Biophysica Acta* 212, 1-& (1970).
137. Torchilin, VP, R Rammohan, V Weissig, TS Levchenko: TAT peptide on the surface of liposomes affords their efficient intracellular delivery even at low temperature and in the presence of metabolic inhibitors. *Proceedings of the National Academy of Sciences of the United States of America* 98, 8786-8791 (2001).
138. Nieland, TJJ, M Ehrlich, M Krieger, T Kirchhausen: Endocytosis is not required for the selective lipid uptake mediated by murine SR-BI. *Biochimica Et Biophysica Acta-Molecular and Cell Biology of Lipids* 1734, 44-51 (2005).
139. Arbab, AS, LA Bashaw, BR Miller, EK Jordan, JWM Bulte, JA Frank: Intracytoplasmic tagging of cells with ferumoxides and transfection agent for cellular magnetic resonance imaging after cell transplantation: Methods and techniques. *Transplantation* 76, 1123-1130 (2003).
140. Frank, JA, H Kalish, EK Jordan, SA Anderson, E Pawelczyk, AS Arbab: Color transformation and fluorescence of Prussian-Blue-positive cells: Implications for histologic verification of cells labeled with superparamagnetic iron oxide nanoparticles. *Molecular Imaging* 6, 212-218 (2007).
141. Kneuer, C, M Sameti, U Bakowsky *et al.*: A nonviral DNA delivery system based on surface modified silica-nanoparticles can efficiently transfect cells in vitro. *Bioconjugate Chemistry* 11, 926-932 (2000).

142. Li, Z, SG Zhu, K Gan *et al.*: Poly-L-lysine-modified silica nanoparticles: A potential oral gene delivery system. *Journal of Nanoscience and Nanotechnology* 5, 1199-1203 (2005).
143. Chang, JS, KLB Chang, DF Hwang,ZL Kong: In vitro cytotoxicity of silica nanoparticles at high concentrations strongly depends on the metabolic activity type of the cell line. *Environmental Science & Technology* 41, 2064-2068 (2007).
144. Hardman, R: A toxicologic review of quantum dots: Toxicity depends on physicochemical and environmental factors. *Environmental Health Perspectives* 114, 165-172 (2006).
145. Lim, Y, JH Kim, KA Kim *et al.*: Silica-induced apoptosis in vitro and in vivo. *Toxicology Letters* 108, 335-339 (1999).
146. Zhang, TT, JL Stilwell, D Gerion *et al.*: Cellular effect of high doses of silica-coated quantum dot profiled with high throughput gene expression analysis and high content cellomics measurements. *Nano Letters* 6, 800-808 (2006).
147. Lin, WS, YW Huang, XD Zhou,YF Ma: In vitro toxicity of silica nanoparticles in human lung cancer cells. *Toxicology and Applied Pharmacology* 217, 252-259 (2006).
148. Magrez, A, S Kasas, V Salicio *et al.*: Cellular toxicity of carbon-based nanomaterials. *Nano Letters* 6, 1121-1125 (2006).
149. Medina, C, MJ Santos-Martinez, A Radomski, OI Corrigan,MW Radomski: Nanoparticles: pharmacological and toxicological significance. *British Journal of Pharmacology* 150, 552-558 (2007).
150. Nel, A, T Xia, L Madler,N Li: Toxic potential of materials at the nanolevel. *Science* 311, 622-627 (2006).
151. Chavanpatil, MD, A Khair,J Panyam: Nanoparticles for cellular drug delivery: Mechanisms and factors influencing delivery. *Journal of Nanoscience and Nanotechnology* 6, 2651-2663 (2006).
152. Hobbs, KL, PR Larson, GD Lian, JC Keay,MB Johnson: Fabrication of nanoring arrays by sputter redeposition using porous alumina templates. *Nano Letters* 4, 167-171 (2004).
153. Kim, C, JB Park, HG Jee *et al.*: Formation of Au nanostructures through an alumina mask by laser-assisted deposition. *Journal of Nanoscience and Nanotechnology* 5, 306-312 (2005).
154. Lee, W, R Ji, U Gosele,K Nielsch: Fast fabrication of long-range ordered porous alumina membranes by hard anodization. *Nature Materials* 5, 741-747 (2006).
155. Lei, Y, WP Cai,G Wilde: Highly ordered nanostructures with tunable size, shape and properties: A new way to surface nano-patterning using ultra-thin alumina masks. *Progress in Materials Science* 52, 465-539 (2007).
156. Zhao, S, H Roberge, A Yelon,T Veres: New application of AAO template: A mold for nanoring and nanocone arrays. *Journal of the American Chemical Society* 128, 12352-12353 (2006).
157. Jessensky, O, F Muller,U Gosele: Self-organized formation of hexagonal pore structures in anodic alumina. *Journal of the Electrochemical Society* 145, 3735-3740 (1998).

158. Lee, W, R Scholz,U Gosele: A continuous process for structurally well-defined Al₂O₃ nanotubes based on pulse anodization of aluminum. *Nano Letters* 8, 2155-2160 (2008).
159. Lee, W, K Schwirn, M Steinhart, E Pippel, R Scholz,U Gosele: Structural engineering of nanoporous anodic aluminium oxide by pulse anodization of aluminium. *Nature Nanotechnology* 3, 234-239 (2008).
160. Zhao, LL, M Steinhart, U Gosele,S Schlecht: Reactive templates: Doing chemistry with pore walls. *Advanced Materials* 20, 1218-1221 (2008).
161. Gasparac, R, P Kohli, MO Mota, L Trofin,CR Martin: Template synthesis of nano test tubes. *Nano Letters* 4, 513-516 (2004).
162. Hillebrenner, H, F Buyukserin, JD Stewart,CR Martin: Biofunctionalization and capping of template synthesized nanotubes. *Journal of Nanoscience and Nanotechnology* 7, 2211-2221 (2007).
163. Slowing, II, BG Trewyn, S Giri, VSY Lin: Mesoporous silica nanoparticles for drug delivery and biosensing applications. *Advanced Functional Materials* 17, 1225-1236 (2007).
164. Slowing, II, JL Vivero-Escoto, CW Wu, VSY Lin: Mesoporous silica nanoparticles as controlled release drug delivery and gene transfection carriers. *Advanced Drug Delivery Reviews* 60, 1278-1288 (2008).
165. Slowing, I, BG Trewyn, VSY Lin: Effect of surface functionalization of MCM-41-type mesoporous silica nanoparticles on the endocytosis by human cancer cells. *Journal of the American Chemical Society* 128, 14792-14793 (2006).
166. Trewyn, BG, S Giri, Slowing, II, VSY Lin: Mesoporous silica nanoparticle based controlled release, drug delivery, and biosensor systems. *Chemical Communications* 3236-3245 (2007).
167. Trewyn, BG, Slowing, II, S Giri, HT Chen, VSY Lin: Synthesis and functionalization of a mesoporous silica nanoparticle based on the sol-gel process and applications in controlled release. *Accounts of Chemical Research* 40, 846-853 (2007).
168. Giri, S, BG Trewyn, VSY Lin: Mesoporous silica nanomaterial-based biotechnological and biomedical delivery systems. *Nanomedicine* 2, 99-111 (2007).
169. Sugawara, M: Plasma etching fundamentals and applications. 1998.
170. Campbell, SA: The science and engineering of microelectronic fabrication. 2001, New York: Oxford University Press.
171. Gottscho, RA, CW Jurgensen, DJ Vitkavage: Microscopic Uniformity in Plasma-Etching. *Journal of Vacuum Science & Technology B* 10, 2133-2147 (1992).
172. Lichtenberg, MALaAJ: Principles of plasma discharges and materials processing. 2nd ed. 2005, Hoboken, New Jersey: John Wiley & Sons, Inc.
173. Moore, D, R Carter, H Cui *et al.*: Process integration compatibility of low-k and ultra-low-k dielectrics. *Journal of Vacuum Science & Technology B* 23, 332-335 (2005).
174. Petkov, MP, MH Weber, KG Lynn, KP Rodbell, SA Cohen: Open volume defects (measured by positron annihilation spectroscopy) in thin film

hydrogen-silsesquioxane spin-on-glass; correlation with dielectric constant. *Journal of Applied Physics* 86, 3104-3109 (1999).

175. Shamiryan, D, MR Baklanov, S Vanhaelemeersch, K Maex: Comparative study of SiOCH low-k films with varied porosity interacting with etching and cleaning plasma. *Journal of Vacuum Science & Technology B* 20, 1923-1928 (2002).